METAMATERIAL DESIGN AND ITS APPLICATION FOR ANTENNAS

Sen YAN

Supervisor:
Prof. dr. ir. Guy A. E. vandenbosch

Members of the Examination Committee:
Prof. dr. ir. Paul Sas (Chair)
Prof. dr. ir. Georges Gielen
Prof. dr. ir. Dominique M. M.-P. Schreurs
Prof. dr. ir. A. B. (Bart) Smolders
(TU Eindhoven)
Ir. Walter L. De Raedt (IMEC)

Dissertation presented in partial fulfilment of the requirements for the degree of PhD in Engineering

May 2015

Uitgegeven in eigen beheer, Sen YAN, Sint-Lambertusstraat 33, Heverlee

Foreword

Time is like a fleeting show. Four years of PhD research may be the most important period in my life. The result of the PhD is not only several academic papers, but most importantly, the way how I am thinking and acting in the academic field, which will definitely change my career in the future.

This PhD work cannot be finished without the contribution of many people. I would like to express my best gratitude to my mentors, colleagues, friends, and my family.

Firstly, I owe an endless gratitude to my supervisor Prof. Guy Vandenbosch for the opportunity of joining the TELEMIC group. I learnt a lot of things from him, not only the academic knowledge, but also the way of research. This will be precious wealth in all my future academic life. Our communication is always flexible and efficient. That is the main reason why we can achieve so many productions. He also friendly supported me a lot in my daily life which I am truly appreciated.

Besides, I am eternally grateful to my PhD committee and jury, Prof. Dominique Schreurs, Prof. Georges Gielen, Prof. Bart Smolders, Prof. Paul Sas and Ir. Walter Raedt. They gave me a lot of suggestions and comments that help improve the thesis a lot. I also wish to express my sincere appreciation to all the professors in our group, Prof. Bart Nauwelaers, Prof. Emmanuel Van Lil, Prof. Sofie Pollin. They gave me a lot of guides in my study.

My deep thanks also go to Dr. Ping Jack Soh. We discussed our work together and struck some sparks of novel idea in 2013. With his help, I can introduce my technology in the field of wearable antennas, and our cooperation obtained a wide-ranging influence in this academic field. Many thanks to Dr. Vladimir Volski, Dr Xuezhi Zheng, Dr. Marco Mercuri, and Dr. Alexander Svezhentsev. They provide great help in my research, including basic theory, fabrication, and measurement. Thanks to our best assistant Ann Deforce. She always patiently and kindly gave us endless help. I also want to

express my thanks all our colleagues in TELEMIC group, Enas Gustavo, Ilja, Hadi, Saeed, Zhanna, Costanza, Rudy, Tomislav and etc.

I also would like to thank my Chinese friends, Ma Zhongkun, Peng Bo, Wang Lingyu, Xu Hantao, Liu Song, Xiao Dongping, Pan ning, Kong Linghui, Wang Jiachen, Bao Junchen, Wang Qingju, Huang Xiaolin, Yang bohan, Zhang Xueru, Wen Lianggong, Zhang Yang, Cheng Jiqiu, Zhu Peng, for their companies and help during the four years; and Chinese basketball team for those wonderful weekends.

I would like to address special thanks to China Scholarship Council (CSC) for the financial support of my study in Belgium.

Finally, I devote my deep love and gratitude to my family. My merciful parents gave their unconditional love to me and exerted their best to support my study. Thanks to my wife Yuanyuan. You gave up your job and came to accompany me. Your love and understanding encourages me to finish this work. I will hold you and cherish you forever.

Sen Yan
May 2015
Heverlee, Belgium

Abstract

Metamaterials have received increasing attention due to their unique electromagnetic properties. Various types of metamaterial have been proposed with different characteristics, e.g. negative refractive index, huge chirality, magnetic conductivity, etc. These unusual properties play an important role in modern antenna design, which can provide better performance, more functions, and more flexibility.

The main target of this PhD is to deeply study the characteristics of metamaterials, and to use that to improve the performance of microwave antennas. Three types of metamaterial are proposed, i.e. the coated dielectric sphere-based metamaterial with a wide negative refractive index band, the encapsulating metamolecule with high quality factor, and the planar coupled resonators with huge chirality. Different physical parameters are studied for these topologies with both numerical and measured results, and the working mechanisms behind these phenomena are explained by studying current and field distributions. Some potential applications of these structures are also discussed. Then, several antennas based on metamaterials are designed, including dual-band textile patch antennas based on the linear composite right/left-handed transmission line, radial patch antennas operating at zeroth-order mode and negative modes, and low profile antennas loaded with an artificial magnetic conductor plane. All the antennas are designed using simulations and verified through experiments. Their performances improve compared with conventional antennas.

Samenvatting

Metamaterialen krijgen recentelijk heel wat aandacht vanwege hun unieke elektromagnetische eigenschappen. Verschillende soorten metamaterialen met verschillende eigenschappen worden in de literatuur voorgesteld, bvb. negatieve brekingsindex, grote chiraliteit, magnetische geleidbaarheid, etc. Deze ongebruikelijke eigenschappen kunnen een belangrijke rol spelen in moderne antennes. Ze kunnen de prestaties verhogen, en zorgen voor meer functionaliteit en flexibiliteit.

De belangrijkste doelstelling van dit doctoraat is het fundamenteel bestuderen van de kenmerken van metamaterialen, en deze gebruiken om de prestaties van antennes te verbeteren. Drie soorten metamateriaal worden voorgesteld: een 3D versie op basis van gecoate diëlektrische bollen, hetgeen een brede band oplevert waar de brekingsindex negatief is, en 2D versies op basis van ingekapselde metamolecules met een hoge kwaliteitsfactor, en op basis van vlakke gecombineerde resonatoren, met een enorme chiraliteit als gevolg. Verschillende fysische parameters worden bestudeerd voor deze topologieën via zowel numerieke als gemeten resultaten, en de werkingsmechanismen achter deze verschijnselen worden verklaard via het bestuderen van de veldverdelingen. Potentiële toepassingen voor deze structuren worden ook besproken. In een tweede deel van de thesis worden meerdere antennes ontworpen op basis van metamaterialen: dual-band textiel-patch-antennes op basis van de lineaire samengestelde rechts / linkshandige transmissielijn, radiale patch-antennes werkend in een combinatie van nulde-orde mode en negatieve modes, en "low profile" antennes voorzien van een kunstmatige magnetische geleider. Alle antennes worden ontworpen met behulp van simulaties en geverifieerd door middel van experimenten. Het wordt duidelijk aangetoond dat de prestaties verbeteren in vergelijking met conventionele antennes.

Contents

List of Acronyms

AMC	Artificial Magnetic Conductor
BW	Bandwidth
CM	Chiral Media
CMM	Chiral Metamaterial
CP	Circular Polarization
CPW	Coplanar Waveguide
CRLH	Composite Right/Left-Handed
CST MWS	Computer Simulation Technology Microwave Studio
DNG	Double Negative
DPS	Double Positive
DSRR	Double Split-Ring Resonators
EBG	Electromagnetic Band Gap
EIT	Electromagnetically Induced Transparency
ENG	Epsilon Negative
ESA	Electrically Small Antenna
FBR	Front-to-Back Ratio
FEM	Finite Element Method
FOM	Figure of Merit
FS	Free Space
FSS	Frequency Selective Surface
GA	Global Alignment
GSTCs	Generalized Sheet Transition Conditions
HFSS	High Frequency Structural Simulator
IFFT	Inverse Fast Fourier Transformer
LCP	Left Circular Polarization
LHM	Left-Handed Media
LS-SVM	Least Squares Support Vector Machines
MEMS	Micro Electronic Mechanical System
MIMO	Multiple-Input and Multiple-Output
ML	Microstrip Line

MM	Metamaterial
NRI	Negative Refractive Index
PCB	Printed Circuit Board
PEC	Perfect Electrical Conductor
PIFA	Planar Inverted-F Antenna
PMC	Perfect Magnetic Conductor
RCP	Right Circular Polarization
rms	root mean square
SAR	Specific Absorption Rate
SFCW	Stepped-Frequency Continuous Wave
SIW	Substrate Integrated Waveguide
SMT	Surface Mount Technology
SNG	Single Negative
SRR	Split Ring Resonator
TL	Transmission Line
TM	Transverse magnetic
UWB	Ultra-Wideband
VSWR	Voltage Standing Wave Ratio
WBAN	Wireless Body Area Network
WLAN	Wireless Local Area Network
ZOR	Zeroth Order Resonance
ZRI	Zero Refractive Index

Chapter 1

INTRODUCTION

"Material: The matter from which a thing is or can be made."

——Oxford Dictionaries.

In this chapter, the research background and motivation will be introduced. Then the state of the art is reviewed in the fields of metamaterials and their application in antenna design. Next the main objective of the PhD project is discussed together with an overview of this thesis.

1.1 BACKGROUND AND MOTIVATION

The study and research on materials can be traced back to the first humans, several thousand years ago. Hundreds of handbooks have been published, listing diverse properties of materials under different physical circumstances. Engineers can select the proper category of materials for their specific applications. However, it is in the nature of people to never be satisfied with the present situation. They are constantly looking for new materials with novel properties, even properties "not created by God".

A metamaterial is a kind of artificial synthetic composite material with a specific structure, which exhibits properties not found in natural materials. [1] In the narrow sense, a metamaterial is mostly designed based on a periodic structure aiming at novel electromagnetic properties, e.g. negative permittivity or permeability, zero refractive index, and huge chirality [2, 3]. As in natural materials, the properties of metamaterials are decided by their components and their arrangements. In order to obtain specific properties, the components should be designed with specific patterns, yielding resonant structures. The components, sometimes called meta-atoms or metamolecules, are periodically arranged in one, two, or three dimensions. They can be coupled with each other which considerably modifies the properties of the metamaterial.

The first concepts of negative refraction and double negative materials were proposed by Mandelstam and Veselage in 1945 [4] and 1967 [5], respectively. The first experiment that verified the feasibility of negative refraction was realized by Smith and Pendry in 2000 [6, 7]. Although great progress has been made in this field in the new century [2, 3, 8-12], a unique, clear and accurate definition of the general concept "metamaterial" is still a matter of debate. However, there are several generally accepted features for a metamaterial. The most important of all is that it is required that the dimensions of the unit cells, and thus the periodicity of the metamaterial, are much smaller than the operating wavelength. This ensures that one obtains a quasi-homogeneous material [2, 3]. This is a clear difference with some other periodic structures, e.g. photo crystals, scattering arrays, electromagnetic bandgap topologies, etc.

Metamaterials have been widely used in the design of microwave devices and antennas. A huge number of new devices and antennas have been fabricated with novel performances. These will be reviewed in the next two sections. However, due to the fast development of flexible portable devices

such as mobile phones, laptops, wearable devices, etc., antennas with different tunable functions, based on variable structures, are still in urgent demand. This is the motivation of this PhD project. We aim at designing several novel metamaterials, and use them to further improve the performance of antennas. This will give more design freedom and a better performance for wireless communication systems.

1.2 REVIEW OF METAMATERIALS

As a hot research topic in the recent 15 years, metamaterials have achieved great successes in the fields of both science and engineering. Variable metamaterials have been designed from radio frequencies up to optical frequencies, and different functions have been realized, e.g. negative refractive index (NRI), huge chirality, anisotropy and bianisotropy [2, 3]. As an interdisciplinary topic, metamaterials can be classified into different categories based on different criteria. From an operating frequency point of view, they can be classified as microwave metamaterials, terahertz metamaterials, and photonic metamaterials. From a spatial arrangement point of view, there are 1D metamaterials, 2D metamaterials, and 3D metamaterials. From a material point of view, there are metallic and dielectric metamaterials. In this work we will concentrate on the electromagnetic properties, and introduce several important types of metamaterials in the microwave frequency range.

1. Veselago media

Veselago media were the first type of metamaterial proposed [4, 5]. Depending on the real part of the permittivity and permeability metamaterials can be classified as given in Fig. 1-1 [3, 13]. The upper right corner contains the normal materials, which have both a positive permittivity and a positive permeability. DPS stands for “double positive”. In contrast, the lower left corner contains the DNG media, which have both a negative permittivity and a negative permeability. This type of metamaterials is sometimes called left-handed media (LHM) or negative refractive index (NRI) media [8]. A lot of interesting phenomena can be observed in them: anomalous refraction [6, 14], reversed Doppler shift [15, 16], inverse Cherenkov radiation [17, 18], opposite group velocity and phase velocity [19, 20], etc..

In the upper left and lower right corners, there are two kinds of metamaterial with only the permittivity or the permeability negative. They

are called single negative (SNG) media. The materials with near zero permittivity and permeability are located around the x-axis and y-axis, respectively. In the centre, the zero refraction index (ZRI) materials can be found.

2. High impedance plane

A high impedance plane is a kind of 2D metamaterial, sometimes called metasurface. The plane consists of a periodic structure of resonant unit cells. When an electromagnetic wave impinges on the surface, the phase of the reflected wave will be tuned by these resonators. Based on this phase several types can be distinguished, see Fig. 1-2 [21-23].

When the reflection phase approaches 180°, the plane starts to behave like a perfect electric conductor (PEC). When the reflection phase approaches 0°, the plane starts to behave as a perfect magnetic conductor (PMC), or an artificial magnetic conductor (AMC) [22-24]. In other situations, the phase of the reflection wave is advanced or delayed with respect to the incident wave. In this case, we distinguish capacitance planes and inductance planes, respectively [25, 26]. It is important to point out that by choosing the resonators and tuning their dimensions, the reflection wave can be fully controlled at specific frequencies.

Another important type of metasurface is the absorber plane [27, 28]. In this case the materials of the unit cells are lossy. In the limit, the incident wave is absorbed totally, and no wave at all is reflected.

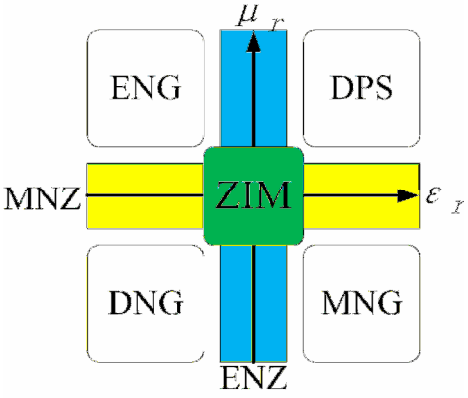

Fig. 1-1 The nomenclature of metamaterials, based on the values of the real parts of their permittivity and permeability. [3, 13] DPS: double positive media, ENG: ε negative media, MNG: μ negative media, DNG: double negative media, ENZ: ε near zero media, MNZ: μ near zero media, ZIM: zero index media.

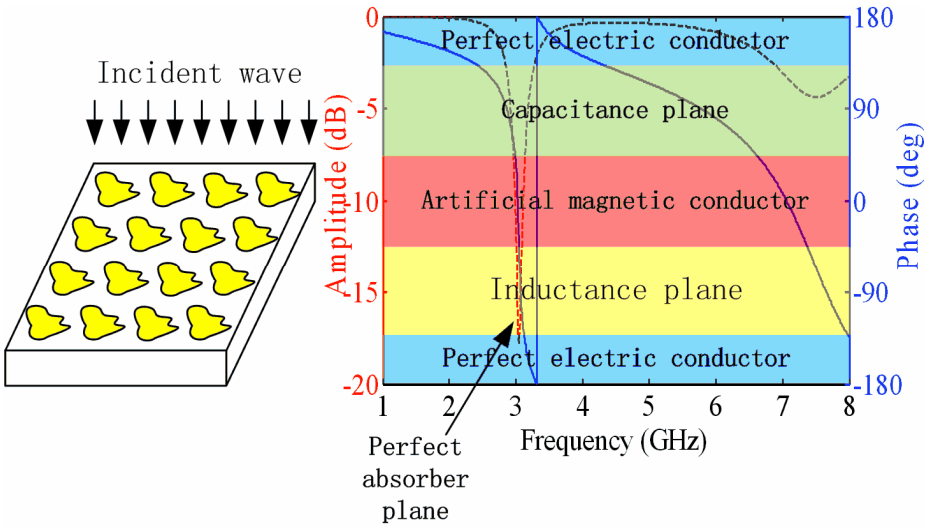

Fig. 1-2 The nomenclature of a high impedance plane.

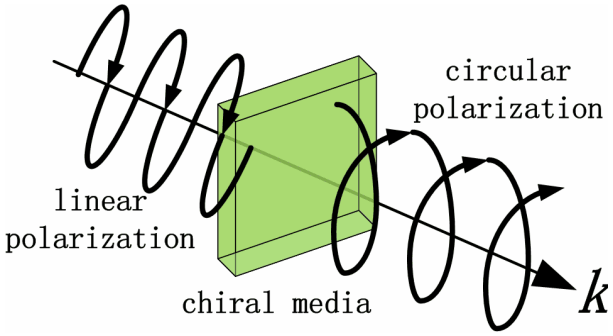

Fig. 1-3 The function of chiral media.

3. Chiral media

The term chiral describes an object, especially a molecule, which has or produces a non-superimposable mirror image of itself [29]. This property changes the polarization of an incident electromagnetic wave. In natural materials chirality is usually weak and only at some special frequencies. However, huge chirality can be designed with metamaterials at arbitrary frequencies. Indeed, by choosing a metamolecule with an asymmetric pattern in 3D space, a chiral metamaterial is easily realized. This metamaterial can be a 3D bulk medium as well as a 2D plane with only one layer of metamolecules. Media like that have been realized in a frequency range from

radio frequencies up to optical frequencies. This property can be used in polarizers (Fig. 1-3), polarized filters, and polarized splitters. [30-34]

4. Other metamaterials

There are a lot of metamaterial types with novel characteristics other than the ones mentioned above, e.g. high anisotropy [35, 36], large nonlinearity [37, 38], huge dispersion [10], etc.. All of these features have their special applications in different fields. In the next section, several important applications in antenna design will be introduced.

1.3 METAMATERIALS IN ANTENNA DESIGN

One of the most important applications of metamaterials is antenna design. Due to the unusual properties of metamaterials, we can achieve antennas with novel characteristics which cannot be realized with traditional materials. In this section, several types of metamaterial loaded antennas will be reviewed.

1. Electrically small antennas based on zeroth resonant mode

In mobile communication systems, electrically small antennas (ESA) are desired. Modern integrated circuit technology has the ability to miniature circuits to a very small size. However, in a traditional design, the performance of the antenna is related with its size. The antenna usually has dimensions in the order of the operating wavelength. This sets boundaries for the size of the whole system. [39-42]

A ZIM medium, whose refractive index is near zero, shows an operating wavelength that is infinite at an arbitrary designed frequency. This phenomenon is named zeroth resonant mode. Since the wave number in this antenna is zero, in theory, the physical size of the antenna can be made independent of its working frequency. Because the operating wavelength is infinite, the field distribution and the radiation pattern are different from the normal ones. [43-46]

2. Dual-band and multi-band antennas

Normal dual-band antennas are realized with different resonant structures, or different resonant modes in one structure. The main disadvantage of this technique is that the field distributions in these structures can hardly be the same in both bands. This means that the radiation patterns in the operating bands are different. [47-51] Since metamaterials can support a negative

refractive index, the resonant modes can be selected as a symmetric pair, i.e. so-called negative and positive modes. The field distributions of these two modes can be very similar, and thus also the radiation patterns. [52-54]

Negative and positive modes can be designed together with a zeroth-order mode. This yields a multi-band antenna with a specific pattern for each mode. An extra advantage of a metamaterial-loaded multi-band antenna is the fact that its size is usually smaller than in a traditional design, where the size is decided by the lowest operating frequency. [52, 55]

3. Low Profile planar reflectors

In an electric dipole antenna positioned parallel on top of a PEC plane, the distance between the dipole antenna and the reflector should be approximately a quarter wavelength. Indeed, since the reflective phase at the PEC plane is 180°, the radiation of the image of the electric dipole will start to cancel the radiation of the dipole itself if it is located closer to the reflector. [39]

However, if the reflector is a PMC plane, the reflective phase is zero, and the image of the electric dipole will enhance the radiation when the dipole is located near the PMC plane. This technique allows designing low profile reflectors for electric dipole antennas. [21-23, 56-63]

Conversely, magnetic dipoles, in practice realized by slots or apertures in a ground plate, are also not suitable for placement near any PEC plane because of the generation of parallel plate modes between the two metal planes, which considerably distorts the characteristics. [64] An AMC plane can help to suppress any parallel plate modes. Also in this case, low profile structures become feasible. [64-66]

4. Antenna lenses and polarizers

Dielectric lenses can be used to improve the directivity and gain of an antenna. However, the cost to fabricate a 3D lens is large. Further, the location of the lens should be carefully chosen in relation with the phase centre of the antenna. A metamaterial lens can be formed by a flat 2D structure. Their manufacturing cost is much lower. They can even be integrated with the planar antenna structure to reduce the profile and size of the antenna system. [67, 68]

A polarizer can be based on a chiral medium which has the capability to transform a linearly polarized wave into a circularly polarized wave. This opens a way to design circularly polarized antennas based on existing linearly polarized antennas. [69-71]

5. Other antennas and structures involving metamaterials

There are a lot of other types of antennas and structures involving metamaterials, e.g. leaky wave antennas [72-75], magnetodielectric microstrip antennas [76, 77], ultra-wideband (UWB) antennas with notched bands [78, 79], metamaterial based isolators [80, 81], series power divider [82], dual-band splitters [83] and delay lines [84], etc.. All of these designs have a relatively better performance than the corresponding conventional designs.

1.4 OBJECTIVES AND CONTENTS OF THIS THESIS

The main objective of this PhD project was twofold: 1. to design dedicated new types of metamaterials, and 2. to use metamaterials to further improve the performance of antennas.

In the first part, from Chapter 2 to Chapter 4, the concept of metamaterials is studied in order to acquire a deep physical understanding of their behaviour, and several novel metamaterial structures are proposed. First, a volumetric meta-metamaterial is studied in Chapter 2. It involves a technology to increase the NRI bandwidth by using coated dielectric spheres. The parameters of this structure, i.e. the thickness and the permittivity of the core and the coating, are studied in detail. The optimum negative permeability band can be increased 60 % compared to nude spheres without coating. A combination of the new topology with wires is used to reach an NRI bandwidth of about 23 %. To the knowledge of the authors, to date this is one of the highest bandwidths reported in literature.

Next, in Chapter 3, a planar chiral metasurface is studied. This metamaterial has potential applications in the design of circularly polarized antennas. We use two methods to break the symmetric pattern of the structures to obtain the chirality. One is based on a twisted pair of resonators and the other is based on a displaced pair of resonators. The chirality of each structure is analyzed in both simulations and experiments. An application of this chiral metamaterial is the circular polarizer, which is realized and evaluated. Besides, we investigate the possibility to build a tunable chiral metasurface.

The concept of a metamolecule is discussed in Chapter 4. A metamolucule consists of two different meta-atoms. Both the behaviour of the single meta-atoms and the coupling between them are analyzed. This helps to design a metamaterial with complex properties. The structure studied here can be used as a sensitive sensor.

In the second part of this thesis, we discuss three types of metamaterial-based antennas. Chapter 5 proposes a dual-band textile antenna based on a 1-dimensional type of metamaterial, i.e. a linear array of composite right/left-handed transmission line cells (CRLH TL). Although the antenna topology itself has been studied a lot, we are the first group to design and fabricate a textile version of this antenna type. Two antennas are realized for dual-band WLAN wearable applications. The dual-band antennas are operated in the symmetric modes and maintain a similar broadside radiation pattern in the two bands. The main features of these designs are the flexibility, easy fabrication, low rear radiation, and low specific absorption ratio (SAR).

The radial CRLH TL is studied in Chapter 6. An innovative circuit model of the radial CRLH TL is proposed to analyze this type of metamaterial. Several types of antennas loaded with this kind of metamaterial are presented. It is shown that when a circular patch antenna works at ZOR mode, the resonant frequency of the antenna is independent of its physical size, which can be used to design an electrically small antenna, or a large aperture antenna. It is demonstrated that a sector patch antenna can also support the same ZOR mode as the full circular patch. This topology is much easier to integrate with a matching network to achieve a larger bandwidth. Moreover, the sector patch can operate in multi-frequency bands, and all the bands have a quasi omni-directional radiation pattern.

The third type of antennas studied concerns low profile antennas based on metasurfaces. By locating a slot dipole etched patch on top of an AMC plane, two operating bands are achieved with wide band, low profile, low rear radiation pattern, and high radiation efficiency. The antenna works as a patch antenna in the lower band, and as a slot dipole with PMC reflector in the upper band. The functionality of the metasurfaces is analyzed and two designs are realized based on this topology, one can be used for wearable systems, and the other one can be used for indoor radar systems.

Finally, the thesis is concluded and a view of possible future research is outlined.

Chapter 2

DIELECTRIC COATED SPHERE BASED METAMATERIALS WITH WIDE NEGATIVE REFRACTIVE INDEX BAND

A new metamaterial topology is proposed, based on dielectric coated spheres. The effect of the coating is an increased negative permittivity and permeability bandwidth compared with the non-coated spheres. The influence of the dimensional parameters is analyzed, and the relation of each of them with the bandwidth is studied. The theoretical results are confirmed by full wave simulations using CST MWS. A combination of the new topology with wires is used to reach an NRI bandwidth of about 23 %. To the knowledge of the authors, to date this is one of the highest bandwidths reported in literature.

This chapter is based on the following publication:

[1] S. Yan, and G. A. E. Vandenbosch. "Increasing the NRI bandwidth of dielectric sphere-based metamaterials by coating." Progress In Electromagnetics Research 132 (2012): 1-23.

2.1 INTRODUCTION

A large class of MMs displays a negative refractive index (NRI), i.e. their permittivity and permeability are negative simultaneously. As early as 1968 [5], Veselago theoretically investigated NRI MMs, and predicated some strange electromagnetic effects in these media. After that, MMs disappeared from literature for about 30 years, until Pendry used an array of split ring resonators (SRR) and metallic wires to build a real medium that exhibits the NRI properties in the microwave band [6]. After that, the interest in this field resurged. Huge numbers of scientists studied similar structures, like the double SRR [7], single SRR [85], omega-shaped structures [86], S-shaped [87] and U-shaped structures [88], and spiral resonators [5, 89]. Though all of these have different metallic structures and performances, the basic principle is nearly the same. The unit cell resonates at a certain frequency, whose wavelength is much larger than the size of the cell. Both theory and experiments have shown that the result is significant. However, a series of inherent defects are exhibited, like anisotropy, conductor loss, narrow bandwidth, and also a difficult fabrication in the optical band.

Another route based on Mie resonances of dielectric particles was proposed to solve the above problems. R. Gans and H. Happel were the first ones to investigate a dielectric sphere array more than 100 years ago [90]. Within the context of metamaterials, in 2003, C.L. Holloway and E.F. Kuester pointed out that small spheres with large permittivity and permeability could give an effective negative permittivity and negative permeability [91]. They used Lewin's formula [92]to calculate the effective properties of the mixture. After that in 2004, O. G. Vendik and M.S. Gashinova [93] used spheres with only large permittivity but different sizes to realize the NRI. The authors claimed that this is much easier to fabricate in practice. In 2006, L. Jylhä and I. Kolmakov [94] established a theoretical model using the Clausius-Mossotti relation [95], which is more accurate than Lewin's model. M. S. Wheeler (2006) [14] and L.I. Basilio (2012) [96] simplified things and used spheres of the same size only to realize NRI. E.F. Kuester [97] obtained an NRI bandwidth of ca. 10 % by using layered dielectric spheres while considering realistic losses. Experiments on single sphere structures were performed only by L. Peng (2007) [98], Q. Zhao (2008) [99], X. Cai (2008) [100], and T. Lepetit (2009) [101]. Several kinds of all-dielectric MMs were fabricated and tested to verify the NRI characteristics. L. Y. Liu derived an effective circuit model for this structure in 2011 [102]. This model is more intuitive and gives an analytical

dependency on the electromagnetic and geometrical parameters of the composite. V. Yannopapas (2005) [103] and A. Garcia-Etxarri (2011) [104] used the dielectric sphere structure to obtain the NRI phenomenon at terahertz and infrared frequencies, respectively.

All-dielectric MMs certainly have no conductor losses, and are quasi-isotropic due to inherent symmetries. However, their bandwidth is still a difficult problem. A higher packing density can give a stronger coupling, which means more bandwidth (A. Ahmadi 2007 [105] and I. B. Vendik 2009 [106]). The highest packing density is limited by the size of the particles and the space between them.

In order to extend the NRI bandwidth considerably, in this chapter, an alternative method is proposed and theoretically investigated. The technique involves changing the particles themselves by coating them. Coating the spheres generates more degrees of freedom to control the resonance. After this introduction, in the second section, the existing model for all-dielectric single spheres is used, to the knowledge of the authors for the first time, to study the negative permittivity and permeability bandwidth in terms of the topological parameters of the structure. After that, in a third section, the topology with coated spheres is introduced. The theoretical model for this topology is constructed, and verified with CST simulations. Results for coated spheres are compared with results for nude spheres. It is proven that coating allows to considerably increase either the negative permeability or negative permittivity bandwidth. Note that in sections 2.2 and 2.3, the main goal is to study separately the negative permittivity and negative permeability bands of the coated sphere structure, i.e. center frequency and bandwidth of these (possibly different) bands. The actual realization of a wide band NRI metamaterial is reported in the fourth and last section, where an array of wires is added, yielding a structure of both coated spheres and wires. The NRI bandwidth reached there is ca. 23 %.

2.2 ARRAY OF NUDE SPHERES

Consider a structure consisting of a lattice of dielectric particles. If the radius of the particles is much smaller than the wavelength in the mixture, the mixture can be seen as a homogeneous material. Its effective properties can be obtained from the generalized Clausius-Mossotti relations [94] near the first two Mie resonance modes

$$\frac{\varepsilon_{eff}-\varepsilon_b}{\varepsilon_{eff}+2\varepsilon_b}=\frac{N\alpha}{3} \tag{2.1}$$

$$\frac{\mu_{eff}-\mu_b}{\mu_{eff}+2\mu_b}=\frac{N\beta}{3} \tag{2.2}$$

where, ε_{eff} and μ_{eff} are the effective permittivity and permeability of the matrix. ε_b and μ_b are the permittivity and permeability of the background host material. α and β are the electric and magnetic polarizability of the particles, N is the number of spheres per unit volume. α and β are related to the scattering coefficients a_1 and b_1 of the first lowest electric and magnetic dipole modes [95].

$$\alpha=\frac{6\pi j b_1}{k_0^3} \tag{2.3}$$

$$\beta=\frac{6\pi j a_1}{k_0^3} \tag{2.4}$$

So we get

$$\varepsilon_{eff}=\varepsilon_b\frac{2(k_0r)^3+6jf_va_1}{2(k_0r)^3-3jf_va_1} \tag{2.5}$$

$$\mu_{eff}=\mu_b\frac{2(k_0r)^3+6jf_vb_1}{2(k_0r)^3-3jf_vb_1} \tag{2.6}$$

where $f_v=\frac{4}{3}\pi Nr^3=\frac{4\pi}{3}\left(\frac{r}{s}\right)^3$ is the volume fraction. r is the radius of the spheres and s is the distance between the sphere centers. For a certain array, once the scattering coefficients are calculated, the effective parameters are obtained from (2.5) and (2.6).

An array of "nude" spheres is shown in Fig. 2-1. The permittivity of the spheres is ε_1 and their radius is r_1. From Mie-scattering theory, the scattering coefficients are expressed as [107]

$$a_m=\frac{n_1\psi_m(n_1x_1)\psi_m'(x_1)-\psi_m(x_1)\psi_m'(n_1x_1)}{n_1\psi_m(n_1x_1)\xi_m'(x_1)-\xi_m(x_1)\psi_m'(n_1x_1)} \tag{2.7}$$

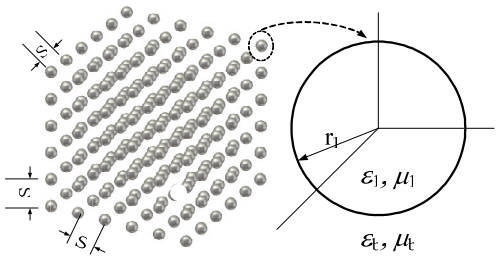

Fig. 2-1. Array of spheres

$$b_m = \frac{\psi_m(n_1 x_1)\psi_m'(x_1) - n_1\psi_m(x_1)\psi_m'(n_1 x_1)}{\psi_m(n_1 x_1)\xi_m'(x_1) - n_1\xi_m(x_1)\psi_m'(n_2 x_1)} \tag{2.8}$$

where $n_1 = \sqrt{\varepsilon_1\mu_1}$, $x_1 = k_0 r_1$, $k_0 = \omega/c$ is the wave vector in vacuum. $\psi_m(z) = z j_m(z)$ and $\xi_m(z) = z h_m^{(1)}(z)$ are the m-th order Riccati-Bessel functions. The prime indicates a differentiation. Inserting(2.7) and(2.8) into (2.5) And (2.6), the Clausius-Mosotti model is obtained [94].

In this section, we will firstly prove that the Lewin model, established in 1947 [92], is identical to a simplified version of the Clausius-Mosotti model for the nude sphere. If $r_1 \ll \lambda/\sqrt{\varepsilon_b\mu_b}$, where λ is the wavelength in vacuum, the first two scattering coefficients can be simplified [107]

$$a_1 = i\frac{2}{3}\left(k_0^2\varepsilon_b\mu_b\right)^{3/2} r_1^3 \frac{\mu_b - \mu_p}{2\mu_b + \mu_p} \tag{2.9}$$

$$b_1 = i\frac{2}{3}\left(k_0^2\varepsilon_b\mu_b\right)^{3/2} r_1^3 \frac{\varepsilon_b - \varepsilon_p}{2\varepsilon_b + \varepsilon_p} \tag{2.10}$$

$$\frac{\varepsilon_p}{\varepsilon_1} = \frac{\mu_p}{\mu_1} = \frac{2(\sin\theta - \theta\cos\theta)}{(\theta^2 - 1)\sin\theta + \theta\cos\theta} = F(\theta) \tag{2.11}$$

where $\theta = kr_1/\sqrt{\varepsilon_1\mu_1}$, so the effective permittivity and permeability are easy to express as

$$\varepsilon_{eff} = \varepsilon_b\left(1 + 3f\Big/\left(\frac{\varepsilon_p + 2\varepsilon_1}{\varepsilon_p - \varepsilon_1} - f_v\right)\right) \tag{2.12}$$

$$\mu_{eff} = \mu_b\left(1 + 3f\Big/\left(\frac{\mu_p + \mu\varepsilon_1}{\mu_p - \mu_1} - f_v\right)\right) \tag{2.13}$$

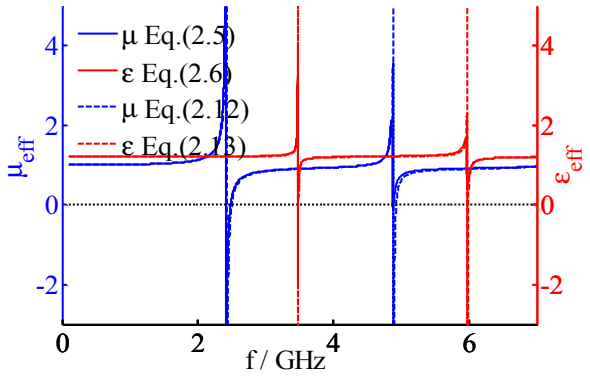

Fig. 2-2. Effective parameters of an array of nude spheres (s = 20 mm, r_1 = 5 mm, ε_1 = 150)

These formulas are identical to the Maxwell-Garnett formulas obtained in a totally different way with the Lewin's model.

An example is calculated to compare the Lewin's model and the Clausius-Mossotti model. It is assumed that the background material and the spheres have the properties ε_b=1, μ_b=1, ε_1=150 and μ_1=1, respectively. The radius of the spheres is r_1 = 5 mm and the distance between them is s = 20 mm. Fig. 2-2 shows the results. It can be seen that Lewin's model is very accurate. The two curves nearly coincide. The bands of negative permittivity and permeability appear alternately at the resonant frequencies. The lowest resonant frequency corresponds to a negative permeability, showing a much wider band than the negative permittivity band displayed by the second resonant frequency.

Further in the paper the center frequencies and relative bandwidths for the resonances are defined as: $\omega_{center} = (\omega_{up}+\omega_{low})/2$ and $\omega_{RBW} = (\omega_{up}-\omega_{low})/2\omega_{center}$. ω_{up} and ω_{down} stand for the boundaries of the negative band as shown in Fig. 2-2. The following section discusses the relationships of ω_{center} and ω_{RBW} with ε_1, r_1 and s.

2.2.1 Change of ε_1 of the spheres

Fig. 2-3 exhibits the characteristics of the negative band with ε_1. When ε_1 is very small, there is no negative band. Above a certain value, the negative band appears. The center frequency of the resonance falls down as ε_1 increases, since the electric size of the spheres becomes larger.

Considering the bandwidth, the negative permeability and permittivity bands show different phenomena. For the negative permeability, the resonance becomes strong when ε_1 rises, so the band extends until it reaches a steady value. For the negative permittivity, the band increases sharply at first, also because the resonance becomes strong, but goes down immediately after it reaches its maximum. The reason is that the resonance, generating the negative component in the permittivity, cannot keep up with the average permittivity of the mixture, which is also increasing.

2.2.2 Change of r_1 of the spheres

In Fig. 2-4, ω_{center} goes down as r_1 increases, while ω_{RBW} grows caused by the coupling between the spheres. When r_1 is too small compared to s, the negative band will not appear. For different ε_1, the negative μ_{eff} band is almost identical, while the negative ε_{eff} band is very different. Note that the topologies with r_1 approaching 10 mm are not suitable in practice, since they

correspond to cases where the spheres almost touch each other. In this case, also note that the strong coupling between the particles may induce a strange resonance, as described in [106]. A very narrow extra NRI band is obtained.

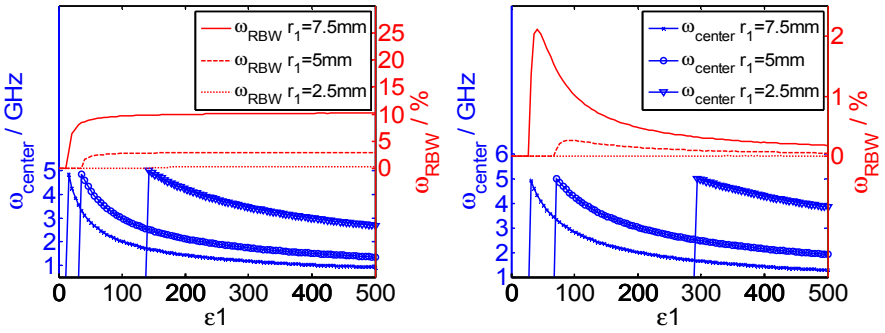

(a) Effective permeability (b) Effective permittivity

Fig. 2-3. The change of the negative band with ε_1 (s = 20 mm)

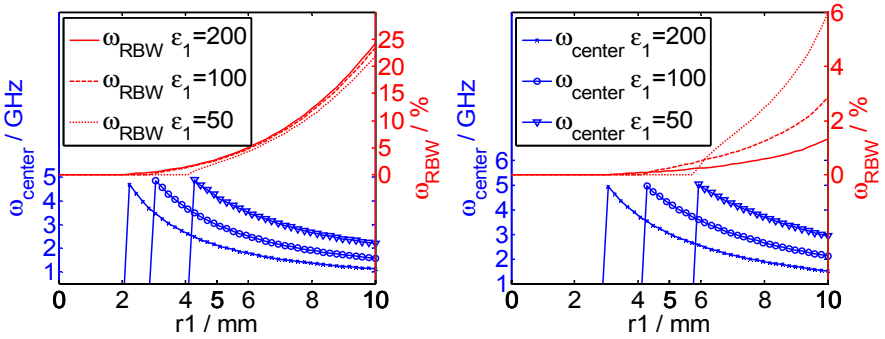

(a) Effective permeability (b) Effective permittivity

Fig. 2-4. The change of the negative band with r_1 (s = 20 mm)

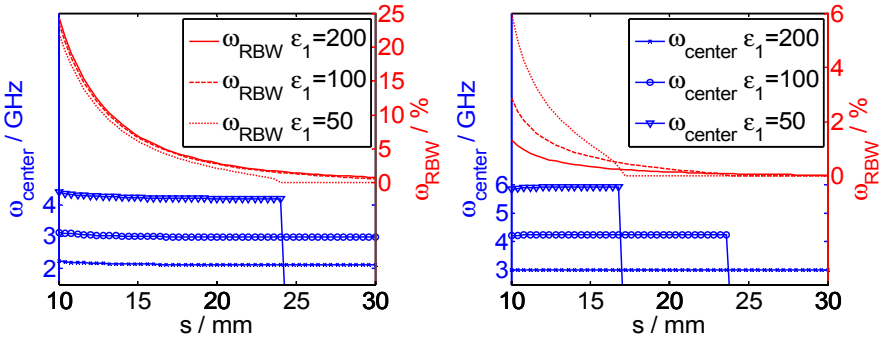

(a) Effective permeability (b) Effective permittivity

Fig. 2-5. The change of the negative band with s (r_1 = 5 mm)

2.2.3 **Change of *s* between the spheres**

With changing the distance s, ω_{center} seems to keep its value. The center frequency is mainly caused by the structure of the particle itself, while the bandwidth is influenced by the embedding of the particle in an array configuration. Indeed, it can be seen that when s is too large, the resonance of this single particle cannot generate the negative aspect any more over the whole unit cell and the negative band disappears.

Generally speaking, the center frequency ω_{center} is mainly related to the size and permittivity of the spheres, while the bandwidth ω_{RBW} is related to the spacing in the array. Usually, foam with $\varepsilon_b = 1$ is chosen as the host medium, so only three parameters, s, r_1, and ε_1, can be adjusted in order to design the MMs for the nude spheres.

2.3 ARRAY OF COATED SPHERES

In this section an array of coated spheres, as shown in Fig. 2-6, is studied. There are five parameters in this topology: the two permittivities, the radii of the core and the coating, and the spacing in the array. We will show that if the five parameters are chosen properly, the bandwidth of the negative band is increased remarkably.

The core of the particle has the radius r1 and permittivity ε1 and the coating has an outer radius r_2 and permittivity ε_2. The scattering coefficients of the coated spheres are [107]

$$a_m = \frac{\psi_m(x_2)\left[\psi_m'(n_2x_2) - A_m\chi_m'(n_2x_2)\right] - n_2\psi_m'(x_2)\left[\psi_m(n_2x_2) - A_m\chi_m(n_2x_2)\right]}{\xi_m(x_2)\left[\psi_m'(n_2x_2) - A_m\chi_m'(n_2x_2)\right] - n_2\xi_m'(x_2)\left[\psi_m(n_2x_2) - A_m\chi_m(n_2x_2)\right]} \tag{2.14}$$

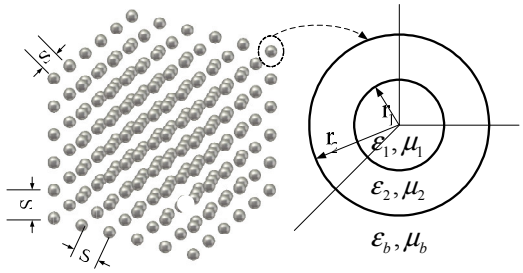

Fig. 2-6. Array of coated spheres

$$b_m = \frac{n_2\psi_m(x_2)\left[\psi_m'(n_2x_2) - B_m\chi_m'(n_2x_2)\right] - \psi_m'(x_2)\left[\psi_m(n_2x_2) - B_m\chi_m(n_2x_2)\right]}{n_2\xi_m(x_2)\left[\psi_m'(n_2x_2) - B_m\chi_m'(n_2x_2)\right] - \xi_m'(x_2)\left[\psi_m(n_2x_2) - B_m\chi_m(n_2x_2)\right]} \tag{2.15}$$

$$A_m = \frac{n_2\psi_m(n_2x_1)\psi_m'(n_1x_1) - n_1\psi_m'(n_2x_1)\psi_m(n_1x_1)}{n_2\chi_m(n_2x_1)\psi_m'(n_1x_1) - n_1\chi_m'(n_2x_1)\psi_m(n_1x_1)} \tag{2.16}$$

$$B_m = \frac{n_2\psi_m(n_1x_1)\psi_m'(n_2x_1) - n_1\psi_m(n_2x_1)\psi_m'(n_1x_1)}{n_2\chi_m'(n_2x_1)\psi_m(n_1x_1) - n_1\psi_m'(n_1x_1)\chi_m(n_2x_1)} \tag{2.17}$$

where $n_1 = \sqrt{\varepsilon_1\mu_1}$, $n_2 = \sqrt{\varepsilon_2\mu_2}$, $x_1 = k_0r_1$, $x_2 = k_0r_2$. $\psi_m(z) = zj_m(z)$, $\xi_m(z) = zh_m^{(1)}(z)$ and $\chi_m(z) = -zy_m(z)$ are the m-th order Riccati-Bessel functions. The a_m and b_m are clearly different compared to the nude spheres. As for the nude spheres, the effective parameters of the coated spheres are obtained by inserting (2.14) and (2.15) into (2.5) and (2.6).

Note that in case that $r_1 \ll \lambda/\sqrt{\varepsilon_b\mu_b}$ and $r_2 \ll \lambda/\sqrt{\varepsilon_b\mu_b}$, a line of reasoning can be followed similar as in the case of a nude sphere to derive simplified formulas for the scattering coefficients. These can be used in (2.5) and (2.6) to yield a model similar as the Maxwell-Garnett model for the nude sphere. Full details can be found in [97]. See also [108] and [109], from which it can be seen that indeed the same results are obtained.

2.3.1 **Change of r_1 of the spheres**

The outer radius of the coated spheres is kept at 5 mm, but the ratio of inter and outer radius (r_1/r_2) is changed. The distance s is kept at 20 mm The core permittivity ε_1 is assumed 200, and the coated permittivity ε_2 is larger than ε_1 in Fig. 2-7 and smaller than ε_1 in Fig. 2-8. For $\varepsilon_2 > \varepsilon_1$, ω_{center} starts lower for both permeability and permittivity, compared with nude spheres. As the coating become thinner, ω_{center} grows gradually until we get the nude situation. But the bandwidth of permeability and permittivity varies differently. ω_{RBW} of μ_{eff} firstly goes up smoothly. After a maximum corresponding with a thin coating of about 1mm, it goes down again. It is remarkable that the coated situation can give a larger ω_{RBW} than a single layer sphere with ε_2 or ε_1. This shows that coated spheres indeed have the capability to enlarge the bandwidth of negative μ_{eff}.

When the permittivity of the coating is lower than the core permittivity ($\varepsilon_2 < \varepsilon_1$), the situation is opposite. The ω_{center} becomes higher and the ω_{RBW} of μ_{eff} has a minimum value. Considering the ω_{RBW} of ε_{eff}, the negative band is larger than for the nude sphere with the purely core permittivity ε_1. But it

does not show a notable improvement compared to the nude sphere with the coating permittivity ε_2 (for example, ε_2 =*100,* ε_1 = *200*).

2.3.2 **Change ε_2 of the spheres**

In this section a different ε_2 is considered, while the core permittivity ε_1 remains 200. In Fig. 2-7, ε_2 is greater than ε_1. The higher ε_2 is responsible for the lower resonant frequency of both μ_{eff} and ε_{eff}. The bandwidth of μ_{eff} becomes larger as ε_2 grows. For a coating layer with suitable thickness (ε_2 = 1600, r_1/r_2 = 0.92), the bandwidth reaches a maximum of 4.3%, nearly 50% above the original one of 2.9 %. Unfortunately, the bandwidth of ε_{eff} is lower than the original.

In Fig. 2-8, ε_2 is less than ε_1. It can be seen in the figure that there is no negative band when ε_2 is too small and r_1 is too thin. With this kind of coating, ω_{center} of both μ_{eff} and ε_{eff} is higher. The variation of the bandwidth show opposite trends compared to Fig. 2-7.

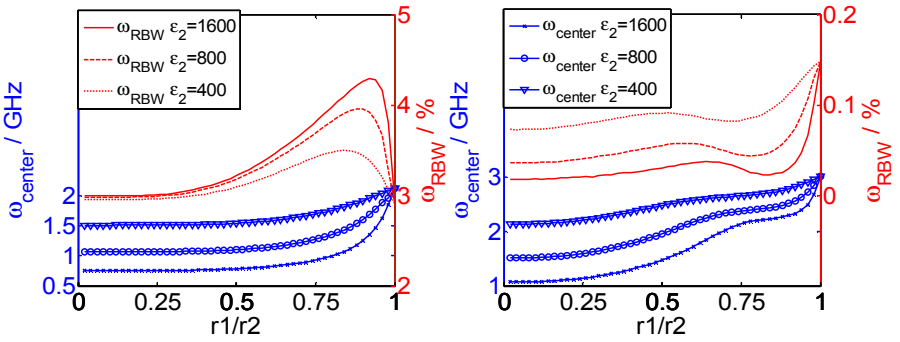

(a) Effective permeability (b) Effective permittivity

Fig. 2-7 The change of negative band with r_1 (s = 20mm, r_2 = 5mm, ε_1 = 200, $\varepsilon_2 > \varepsilon_1$)

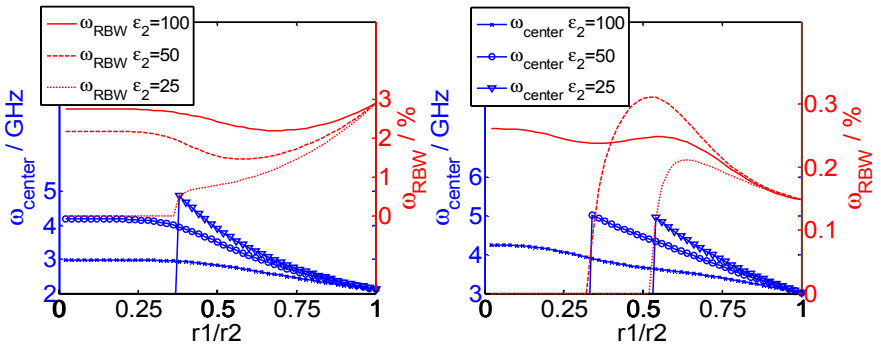

(a) Effective permeability (b) Effective permittivity

Fig. 2-8. The change of negative band with r_1 (s = 20 mm, r_2 = 5 mm, ε_1 = 200, $\varepsilon_2 < \varepsilon_1$)

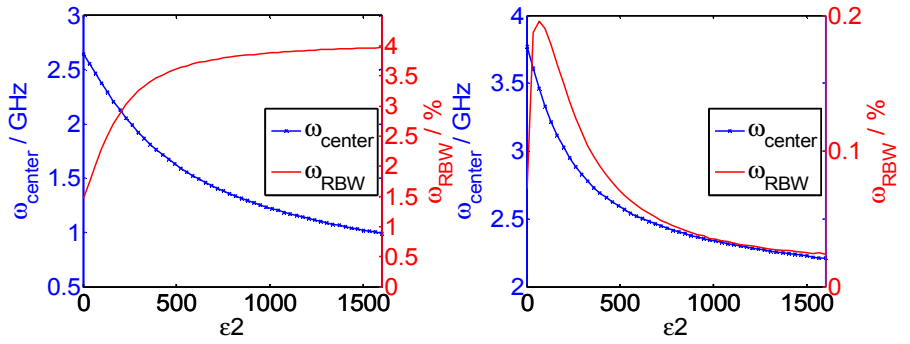

(a) Effective permeability (b) Effective permittivity

Fig. 2-9. The change of the negative band with ε_2 (s = 20 mm, r_1 = 4 mm, r_2 = 5 mm, ε_1 = 200)

In Fig. 2-9, r_1 is kept at 4 mm. Analyzed as a function of ε_2, ω_{RBW} of μ_{eff} first increases rapidly and then "saturates". ω_{RBW} of ε_{eff} first sharply grows and then gradually decreases to a very low value.

2.3.3 **Change *s* between the spheres**

In this section the distance s is changed, aiming at realizing a much wider negative parameter band, see Fig. 2-10. and Fig. 2-11. The distance between the coated spheres is chosen 12 mm, 15 mm, and 20 mm, respectively. It has to be emphasized that Fig. 2-10. and Fig. 2-11. are the key figures of the paper. They present the negative bands for a constant size (radius 5 mm) of the embedded particle. A higher coating permittivity ε_2 (= 1600) is chosen to increase the negative permeability band and a lower permittivity ε_2 (= 25) is chosen to increase the negative permittivity band. Like in the case of the nude sphere ω_{center} does not change with s, because ω_{center} is in practice only depending on the particle itself. However, ω_{RBW} grows continuously when the particles are put closer together since in that case the coupling between them is enhanced. It is clearly seen that a proper thickness of the coating can generate a much larger NRI bandwidth compared to cases where only a single permittivity is used. When only 25 is used as permittivity, there is no negative permittivity band for s = 15 mm and 20 mm. (the utmost left point in the Fig. 2-11 (b)). When only 200 is used, the maximum negative permittivity BW is 0.7 % for s = 12 mm. For a coating of about 3.5 mm, the negative permittivity BW can be boosted up to 3.2 %. Similarly, when we use a proper coating with permittivity 1600 (which is the highest practical value appearing in references), the negative permeability band can reach 22 %, see Fig. 2-10. (a). This is a really wide band for most applications.

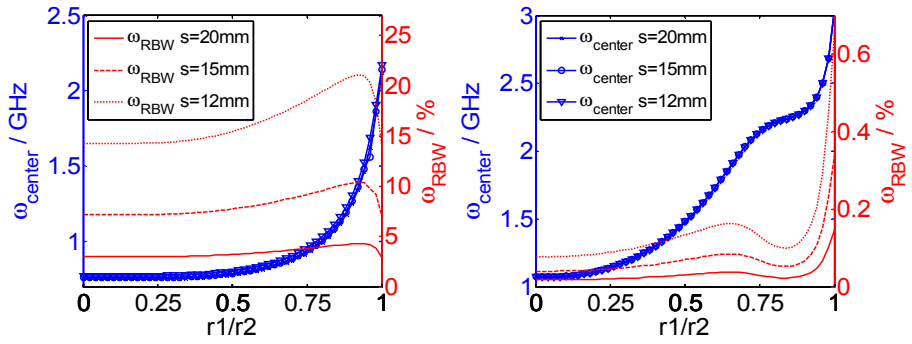

(a) Effective permeability (b) Effective permittivity

Fig. 2-10. The change of the negative band with $r1$ and s (r_2=*5mm*, ε_1=*200*, ε_2=*1600*)

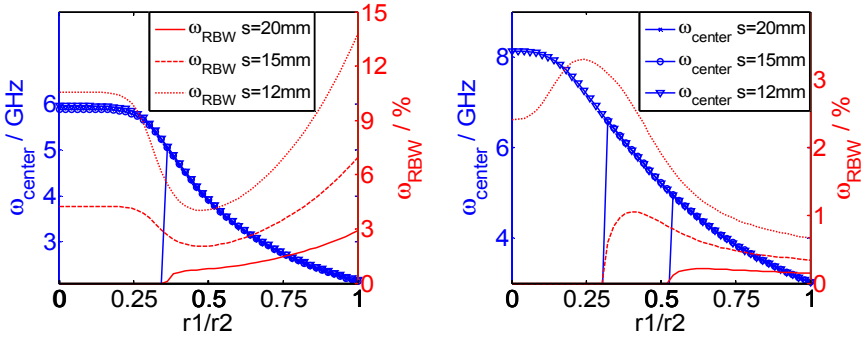

(a) Effective permeability (b) Effective permittivity

Fig. 2-11. The change of the negative band with r_1 and s (r_2=*5mm*, ε_1=*200*, ε_2=*25*)

2.4 VALIDATION AND APPLICATION

2.4.1 **Effective parameter retrieval from S parameters**

In order to verify the results of our model, several structures have been simulated with the frequency solver available in the commercial software CST Microwave Studio.

We mentioned before that the band of the negative permittivity is much narrower than the band of the negative permeability, see for example Fig. 2-3 and Fig. 2-5. Even the coated spheres can only provide a very narrow band with negative permittivity (Fig. 2-11 (b)). That has a strong direct effect on the total bandwidth where a negative index n is obtained. But in microwave frequency bands, a negative permittivity can be easily obtained by an array of metallic wires ([110, 111]). If the radius of the wire is a and the spacing between them is s, the effective permittivity can be expressed as

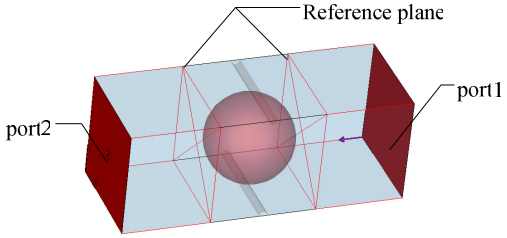

Fig. 2-12 The topology of the CST model.

$$\varepsilon_{eff} = 1 - \frac{1}{\frac{1}{2}\left(\frac{s}{2}\right)^2 \frac{\omega^2}{c^2} \ln\left(\frac{s}{2a}\right) + \frac{j\omega\varepsilon_0}{\sigma}\left(\frac{s}{2a}\right)^2} \tag{2.18}$$

where ω is the circular frequency and c is the wave velocity in vacuum. In the topologies considered below, the dielectric spheres only provide the negative permeability at their first resonant frequency, and the array of metallic wires produces the negative permittivity.

Impedance z and refractive index n are widely used when characterizing electromagnetic materials. They can be related to ε and μ through $\varepsilon = n/z$ and $\mu = n*z$. Usually, z and n are first retrieved from the simulation (in this work we use the technique of [112]), and then ε and μ are calculated.

This procedure is worked out as follows. In CST Microwave Studio, a waveguide with periodic boundaries is built to simulate infinite space, as shown in Fig. 2-12. A short section of vacuum waveguide is added at each end of the sample to ensure extinction of the higher order modes. We set one port at each side of this waveguide and obtain the S-matrix by simulation. This S-matrix is calculated back to the reference planes, also depicted in Fig. 12. This means that the results are actually obtained with respect to the reference planes, which are set at a unit cell boundary.

The number of unit cells actually simulated is based on the following line of reasoning. Since the periodic boundaries ensure periodicity in the transversal directions, transversally we can take one unit cell only. We have simulated different lengths of the 1D metamaterial sample. The result is that the retrieved values for permittivity and permeability are almost independent of the number of unit cells along the length, except for the artificial resonances due to the extraction procedure itself, as discussed in [113]. This is illustrated in Fig. 2-13. This means that using a single unit cell already provides accurate results.

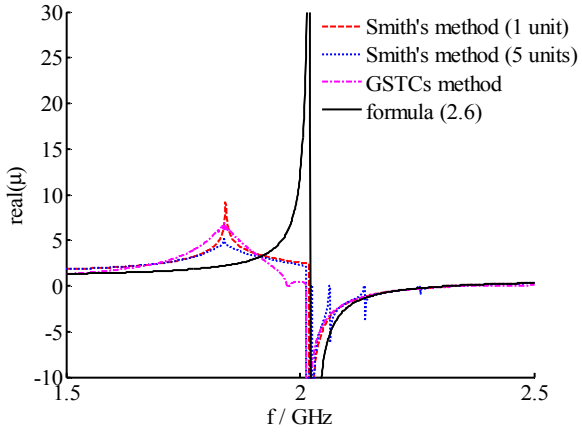

Fig. 2-13 Comparison of different methods. (s = 12 mm, r_1 = 5 mm, ε_1 = 200, a = 0.5 mm)

In [114] it is stated that the problem of the boundary effects can be solved by using the original extraction technique in combination with a proper choice of the reference planes. However, in the same paper it is mentioned: "… to eventually conclude empirically that the first effective boundary of a symmetric one-dimensional metamaterial coincides with the first unit-cell boundary and the second effective boundary coincides with the last unit-cell boundary". This confirms that our choice of the reference planes is correct. If necessary, the technique of [113, 115] can be used to remove the remaining small surface effects. However, this will not change the main conclusions of this paper. This is illustrated in Fig. 2-13, where the method used in this paper (Smith's method, 1 unit) is compared to a case where multiple unit cells are considered (Smith's method, 5 units), and with the generalized sheet transition conditions method (GSTCs method) of [113]. As can be seen, the three methods almost completely coincide in the negative permeability region.

The S parameters are related to n and z by (see)

$$S_{11} = \frac{\Gamma\left(1-e^{j2nk_0d}\right)}{1-\Gamma^2 e^{j2nk_0d}} \tag{2.19}$$

$$S_{21} = \frac{\left(1-\Gamma^2\right)e^{jnk_0d}}{1-\Gamma^2 e^{j2nk_0d}} \tag{2.20}$$

with $k_0 = \frac{2\pi}{\lambda_0} = \frac{2\pi f}{c}$ and $\Gamma = \frac{z-1}{z+1}$. d is the length of the waveguide. This can be easily transformed into

$$z = \pm\sqrt{\frac{(1+S_{11})^2 - S_{21}^2}{(1-S_{11})^2 - S_{21}^2}} \tag{2.21}$$

$$n = \pm\frac{1}{k_0 d}\cos\left[\frac{1}{2S_{21}}\left(1 - S_{11}^2 + S_{21}^2\right)\right] + \frac{2\pi m}{k_0 d} \tag{2.22}$$

Pay attention, for passive materials, Real (z) and Imag (n) must be greater than zero. m is an integer related to the branch of index Real(n). For a thin thickness sample, m can be equalled to zero, while under other conditions, m has to be obtained from the continuity of n. More details on this retrieval method can be found in [114, 116].

2.4.2 **Nude spheres**

In the topological model, the waveguide contains one unit element. Fig. 2-14 shows all corresponding results. Fig. 2-14 (a) and (b) displays the S parameters obtained by CST in three situations, only metallic wires, only nude spheres, and using them together. Fig. 2-14 (c) and (d) reveal the parameters retrieved by using (2.21) and (2.22), compared with our model (using (2.6) and (2.18)). The metallic wires show a wide stop band for the whole simulation frequency range caused by the negative permittivity, while the configuration with nude spheres has an obvious stop band around its first resonant frequency 2.171 GHz, corresponding to the negative permeability. A combination of metallic wires and dielectric spheres can provide double negative parameters, so a pass band appears as expected. This pass band corresponds to a NRI bandwidth of 14.1 %. This cannot be improved significantly by increasing the permittivity of the spheres, as shown by the permeability results in Fig. 2-3 (a). On top, we simulated the NRI bandwidth for a structure with wires and for $\varepsilon_1 = 1600$). The result is only 13.8 %.

The agreement between the permeabilitiy obtained from the CST simulation and from our model is excellent for the array of nude spheres. However, the resonant frequency shifts 0.01 GHz towards higher frequencies for the combination of metallic wires and nude spheres. This means that the metallic wires can influence the permeability a little bit.

The permittivity retrieved for the combination of metallic wires and nude spheres shows little difference with the results obtained from our model. For the CST simulation the permittivity is a little bit perturbed at the first magnetic resonance. This is not obtained from our model. However, this difference is little compared with the much larger influence of the metallic wires.

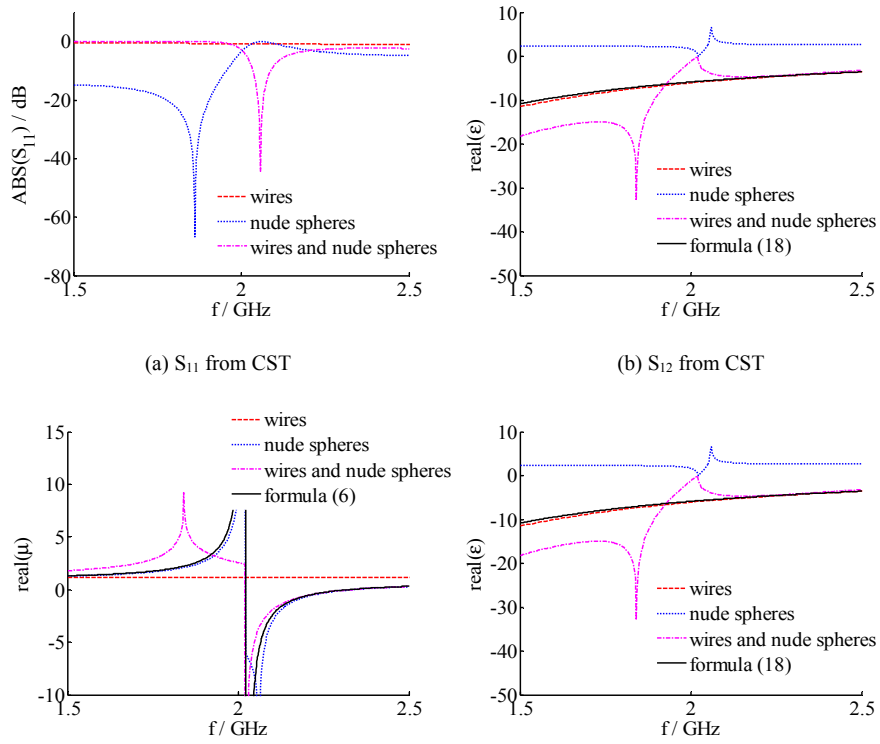

(a) S_{11} from CST

(b) S_{12} from CST

(c) Permeability

(d) Permittivity

Fig. 2-14. Topology of nude spheres.(s = 12 mm, r_1 = 5 mm, ε_1 = 200, a = 0.5 mm)

2.4.3 **Coated spheres**

Also for the coated spheres, our formulas and the CST results agree well, as shown in Fig. 2-15. This proves the correctness of our model for the topology of coated spheres. Little difference still appears for the structure mixing the metallic wires and spheres together, as mentioned for the nude spheres. It is clearly shown that the new technique allows to increase the NRI bandwidth. It is now 23 % around a frequency of 1.34 GHz, which is an obvious improvement of 64 % compared to the nude spheres of the last section (ω_{RBW} = 14 %). Moreover, if we put the spheres more densely together, the relative band could even be further increased by using the mutual coupling, as shown in Fig. 2-5.

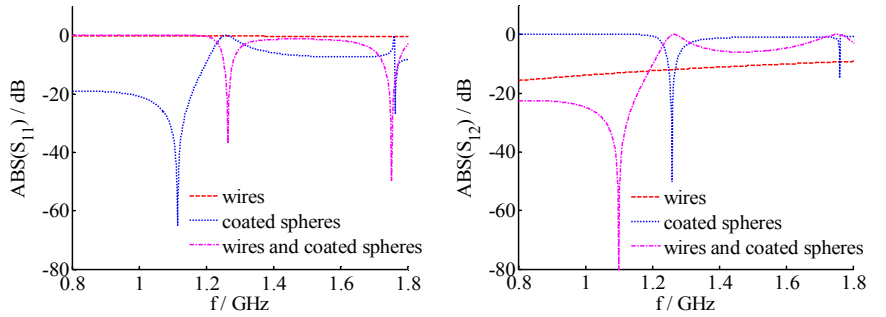

(a) S_{11} from CST

(b) S_{12} from CST

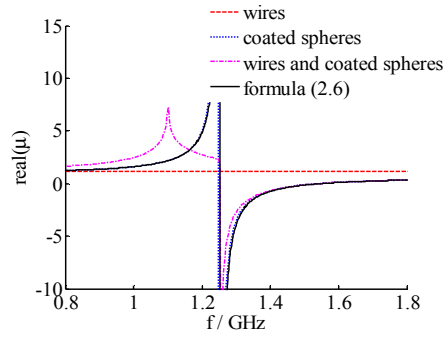

(c) Permeability

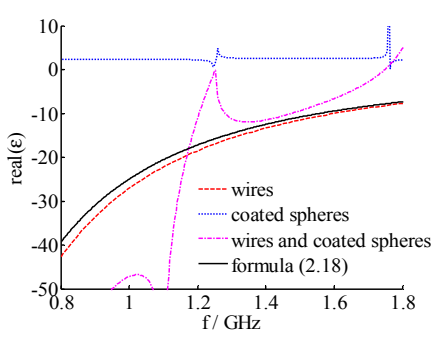

(d) Permittivity

Fig. 2-15 Topology of coated spheres. (*s = 12 mm, r_1 = 5 mm, r_2 = 4.6 mm, ε_1 = 200, ε_2 = 1600, a = 0.5 mm)*

In Fig. 2-16, the amplitude of the electric displacement vector $\varepsilon\mathbf{E}$ on the center line of the waveguide at resonance is shown for three different cases: nudes spheres for $\varepsilon = 200$ and for $\varepsilon = 1600$, and coated spheres. No wires are present. The physical parameters of the spheres are the same as in Fig. 2-14 and Fig. 2-15. It is clearly seen that in the case of the coated spheres, inside the coating this vector (and thus the polarization current) is much larger than within the core spheres. This explains the possible strong effect on the scattering of the incident field, which in its turn explains the effect on the bandwidth, see (2.6).

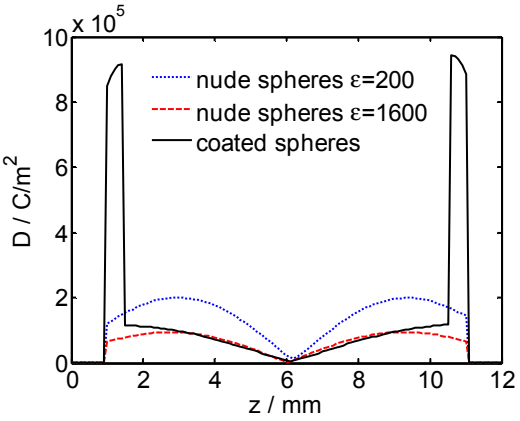

Fig. 2-16. Comparison of the electric displacement vector within the spheres. Wires are not present and the physical parameters of these spheres are the same as in Fig. 2-14 and Fig. 2-15.

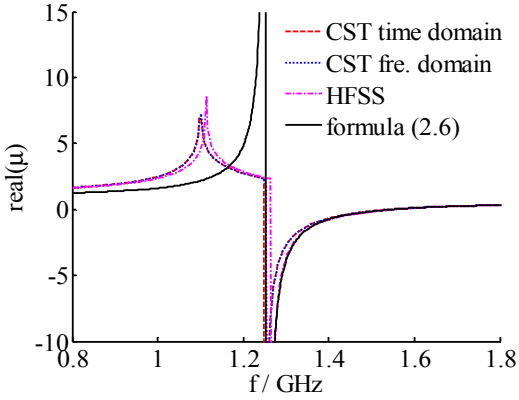

Fig. 2-17. Comparison of different solvers for the topology of wires and coated spheres. (s = 12 mm, r_1 = 5 mm, r_2 = 4.6 mm, ε_1 = 200, ε_2 = 1600, a = 0.5 mm).

In order to verify the results above-mentioned, based on the recommendation given in [117], the results of the frequency solver within CST are compared with the time-domain solver within CST and with HFSS. The results are given in Fig. 2-17. They indicate that the three different solvers agree extremely well. The CST time domain solver practically coincides with the CST frequency domain solver. The HFSS result shows a frequency shift of only 10 MHz (0.8 %).

In order to assess the effect of realistic losses, the topology was also analyzed for $\varepsilon_1 = 200\,(1 - j0.001)$, $\varepsilon_2 = 1600\,(1 - j0.003)$, and $\sigma = 5.8 \times 10^7$ S for the metallic wires, respectively. The CST results yield an attenuation

constant (defined as in [97]) of α = 1.12 dB/λ at 1.35 GHz. This is a really low value very competitive with the values found in the overview table I in [97].

Finally, in TABLE 2-I we compare several kinds of NRI metamaterials described in literature. It can be clearly seen that the topology with coated spheres and wires has the second highest bandwidth of all the structures. The metallic crosses structure of [118] yields the widest band. It can be expected however that this structure is extremely sensitive to small deviations in the gap distances between the crosses, an issue not considered in [118]. The bandwidth in the last column is defined as the bandwidth where the real part of both permittivity and permeability are negative simultaneously.

Nude sphere metamaterials have been fabricated and verified in a few experiments [98-100]. The practical realization of coated spheres however is a huge challenge for researchers active in this field. One of the main reasons is that in the microwave frequency band, the high permittivity dielectrics involved are usually very fragile and extremely difficult to process mechanically. In the terahertz and optical frequency bands, it may be feasible to realize coated structures by using thin film technology.

TABLE 2-I
COMPARISON OF SEVERAL KINDS OF NRI METAMATERIALS

Ref.	*TECHNOLOGY*	*CENTER FREQ. [GHZ]*	*NRI BW [%]*
[6]	SRRs and wires	10.5	9
[86]	Ω-like metallic patterns	12.6	9.5
[88]	U-like metallic patterns	85×10^3	5.9
[118]	Metallic Crosses	11.5	56.7
[93]	Dielectric spheres	67.1	0.3
[94]	Dielectric spheres	10.1	1
[99]	Dielectric cubes and wires	8.6	3.7
[100]	Dielectric spheres and wires	6	11.7
[101]	Dielectric rods	10.8	3.7
[96]	Degenerate dielectric spheres	16.5	6
[14]	Micron-scale coated spheres	3.6×10^3	9.8
This paper	Coated dielectric spheres and wires	1.34	**23**

2.5 CONCLUSION

In this chapter, a specific case of a dielectric metamaterial is discussed. It involves spheres that are coated in order to extend the NRI bandwidth. By using suitable coating materials with optimal permittivity and thickness, the NRI bandwidth can be increased 60 % compared with nude spheres with no coating. In order to obtain these results, an upgraded theoretical model is used and compared with general purpose commercial software. The agreement is excellent. The theoretical model provides an intuitive link between the physical size and the electromagnetic parameters, which can be used to design this kind of all-dielectric MMs.

Chapter 3

PLANAR CHIRAL METAMATERIALS

BASED ON BILAYERED RESONATORS

In this chapter bilayered chiral metamaterials are studied. To obtain the asymmetric pattern in the structures, two types of bilayered structures are proposed. One is based on a twisted pair of resonators, and the other is based on a displaced pair of resonators. Prototypes are fabricated in the microwave frequency band. Simulated and measured results agree well and show significant chirality. The electric fields and currents on the structures are analyzed to illustrate the phenomenon. Because of the simple topologies, these structures can be easily used in polarizers and polarized filters.

This chapter is based on the following three publications:

[1] S. Yan, and G. A. E. Vandenbosch. "Chiral structure based on bilayered displaced U pair." EPL (Europhysics Letters) 103.1 (2013): 18002.

[2] S. Yan, and G. A. E. Vandenbosch. "Compact circular polarizer based on chiral twisted double split-ring resonator." Applied Physics Letters 102.10 (2013): 103503.

[3] S. Yan, and G. A. E. Vandenbosch. "Circular polarizer Based on chiral twisted structure." EMC Europe 2013 Symposium, Brugge, Belgium, Sep. 2013.

3.1 INTRODUCTION

Chirality is a basic phenomenon in electromagnetism and it has been observed and analyzed for over a hundred years [119]. A lot of structures show chirality, from chiral molecules to spiral coils. Chiral media (CM) have the ability to rotate the plane of polarization of the incident wave to the right or left depending on the handedness of the objects. This brings different resonances for different circularly polarized (CP) incident waves. As for their unique characteristics, e.g., asymmetric transmission, optical activity, and circular dichroism, CMs have a lot of applications in optical and microwave devices. Unfortunately, CMs in nature can only provide weak chirality at some special frequencies. However, several kinds of artificial CM structures, or named chiral metamaterials (CMMs), have been proposed. Their unit cells are designed carefully to form different resonances for incident circularly polarized waves, and thus can generate strong chirality.

Since chirality requires an asymmetric pattern, a straightforward idea is to compose CMMs with helices or spiral coils in 3-D space [30]. As this 3-D structure is not easy to fabricate, quasi-planar structures are proposed to realize a similar function [120, 121]. Recently, many researchers focus on bilayered planar structures without vertical metallic connections. Examples are structures based on the conjugated gammadion, the rotating rosette, the twisted cross, the U-shaped SRR, etc.[122-127]. In these structures, the strong chirality is caused by the coupling between the twisted structures on the different layers, without direct metallic connection. These CMMs have been proven to exhibit huge optical activity and circular dichroism from the microwave frequency band to the optical spectrum. Moreover, a single-layer metallic structure can also support chirality when the electromagnetic wave incidents obliquely [128, 129]. Several tunable CMMs have been designed containing active devices in the chiral structure.[130, 131]

Devices based on CMs have also received attention. Several kinds of polarization filters and polarizers for linear and circular polarization have been designed. [30-33, 132] Another application is chiral metamaterials (CMMs), that can show a negative refractive index (NRI) band, without the need to have both permittivity and permeability negative simultaneously, as in the case of traditional NRI metamaterials (MMs). [6, 133] This idea has been realized by several groups already. [134-137]

In the next section of this chapter, a type of compact chiral structure, based on twisted double split-ring resonators (DSRR), is used as a circular

polarizer in the microwave frequency band. The circularly polarized wave can be obtained from a linearly polarized incident wave after it travels through the structure. The difference in level between the transmitted waves with left-circular polarization (LCP) and right-circular polarization (RCP) can reach more than 30 dB near the resonant frequency of the material. Compared with other kinds of CMs, the unit cell of the structure is extremely small in all three dimensions. This is very advantageous when this structure has to be integrated with other small devices like electrical small antennas or small sensors.

Then another type of bilayered chiral structure is introduced. The displacement is used to break the symmetry of the pattern and generates the chirality, instead of rotation. Both optical activity and circular dichroism are observed for circularly polarized waves. The amplitude and phase differences for the transmission coefficients of the circularly polarized waves can reach more than 12 dB and 40° at about 13.4 GHz, respectively. Since the chirality of the bilayered structure can be easily controlled by moving the position of one of the two layers, such a topology is very helpful in the design of tunable CMMs.

3.2 CIRCULAR POLARIZER BASED ON CHIRAL TWISTED DOUBLE SPLIT-RING RESONATOR

A compact circular polarizer is presented, which is based on a twisted double split-ring resonator (DSRR). The bottom DSRR is rotated 90° with respect to the top one. When the structure is illuminated by a normally incident linearly polarized wave, the two linear components of the transmitted wave have nearly equal amplitudes and 90° (-90°) phase difference around the resonant frequency. This means that the transmitted wave with left-handed circular polarization is much larger (smaller) than the one with right-handed circular polarization. The electric fields and currents on the structure are analyzed to illustrate this phenomenon. The size of each unit cell in this structure is extremely small compared with the wavelength in all three dimensions. Both simulations and measurements verify our design at microwave frequencies.

3.2.1 Topology and theoretical description

The unit cell topology of the proposed circular polarizer is shown in Fig. 3-1. Each cell is composed of a pair of stacked DSRRs. The DSRRs in the two layers are coaxial but mutually twisted by 90°. All geometric parameters are

defined in Fig. 3-1 (b). This unit cell can be repeated to create a layer that can function as a polarizer.

Assuming that the incident and transmitted wave are $\overrightarrow{E^i} = E_x^i \hat{x} + E_y^i \hat{y}$ and $\overrightarrow{E^t} = E_x^t \hat{x} + E_y^t \hat{y}$, the linear transmission matrix T_{ll} is

$$\begin{pmatrix} E_x^t \\ E_y^t \end{pmatrix} = \mathbf{T}_{ll} \begin{pmatrix} E_x^i \\ E_y^i \end{pmatrix} = \begin{pmatrix} T_{xx} & T_{xy} \\ T_{yx} & T_{yy} \end{pmatrix} \begin{pmatrix} E_x^i \\ E_y^i \end{pmatrix} \tag{3.1}$$

The circularly polarized transmitted waves can be expressed as

$$\begin{pmatrix} E_+^t \\ E_-^t \end{pmatrix} = \begin{pmatrix} E_x^t + jE_y^t \\ E_x^t - jE_y^t \end{pmatrix} = \mathbf{T}_{cl} \begin{pmatrix} E_x^i \\ E_y^i \end{pmatrix} \tag{3.2}$$

$$\mathbf{T}_{cl} = \begin{pmatrix} T_{+x} & T_{+y} \\ T_{-x} & T_{-y} \end{pmatrix} = \frac{1}{\sqrt{2}} \begin{pmatrix} T_{xx} + iT_{yx} & T_{xy} + iT_{yy} \\ T_{xx} - iT_{yx} & T_{xy} - iT_{yy} \end{pmatrix} \tag{3.3}$$

where the subscripts $_+$ and $_-$ represent the left-handed and right-handed polarized waves, respectively. The constant $1/\sqrt{2}$ is a result of power normalization. The elements in this linear-circular transmission matrix involve the ability of a structure to transform a linearly polarized incident wave into a circular transmitted wave. For a circular polarizer, the goal is that one CP wave is much larger (smaller) than the other one, e.g. $T_{+x} \gg T_{-x}$ or $T_{+x} \ll T_{-x}$.

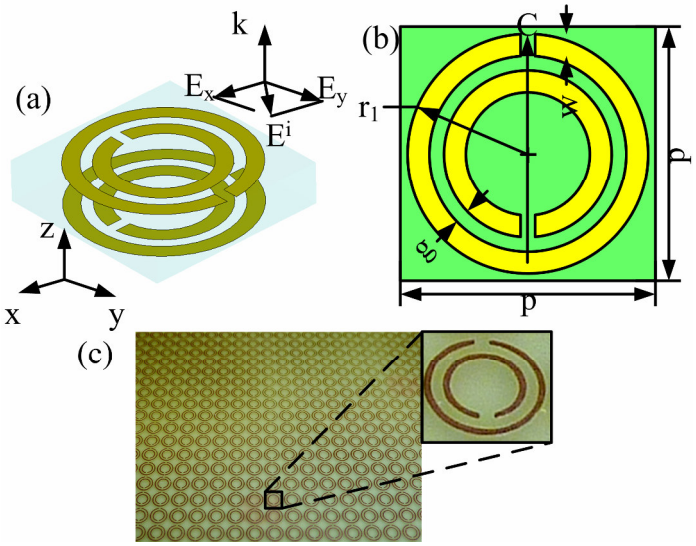

Fig. 3-1. (a) The unit cell topology of the circular polarizer. (b) Parameters of the unit cell: (c) Photo of the prototype fabricated (a zoomed in unit cell is shown): p = 3.5 mm, r_1 = 1.65 mm, g = 0.2 mm, w = 0.3 mm.

A prototype was fully designed, fabricated, and measured. The DSRRs are etched on the two sides of an FR4 board (ε_r = 3.5, *tan* δ = 0.025) with thickness 0.8 mm. The sample is composed of 50 × 50 unit cells, making the total size of the PCB equal to 17.5 cm × 17.5 cm. A photo of the sample is given in Fig. 3-1 (c).

The radii of the DSRRs in combination with the size of the gaps control the operating frequencies of the polarizer. The thickness of the substrate is the key parameter in the coupling between the pair of DSRRs. If the thickness is zero, no chirality will occur, since the structure is symmetric in the transmitted direction. However, if the thickness is too large, the coupling between the two DSRRs is too small, each of the layers (and consequently also the whole structure) shows achirality. Here, the thickness 0.8 mm is carefully selected from the set of available standard substrate thicknesses.

The structure is modeled and simulated with the frequency domain solver within CST Microwave Studio, which is based on the finite element method (FEM). The unit cell boundaries and Floquet ports are used in the model.

The measured results are obtained by a vector network analyzer (Agilent 8510C) in a transmission measurement set-up using two standard gain horn antennas (Narda microwave-east standard gain horn 640). Since multiple reflections occur between the two horns, “raw” measurement data show an oscillating behavior. A data processing procedure similar as in[138] is used to remove these oscillations. It implements a kind of low-pass filter.

3.2.2 **Simulated and measured results**

The transmission coefficients for linear polarization are given in Fig. 3-2. After data processing, the simulated and measured results agree very well in the operating frequency band. Due to the lack of fourfold symmetry, the cross transmission coefficients are different for an incident wave with x-polarization and one with y-polarization ($T_{xy} \neq T_{yx}$). For a normally incident wave with x-polarization, the transmitted waves for the two linear polarizations nearly have the same amplitudes and a +90° (-90°) phase difference at about 8.8 GHz (10.3 GHz), which means that a nearly pure circular polarization wave is formed. On the other hand, for an incident wave with y-polarization, also a resonance is obtained at the same frequency, but its cross-polarization transmission is much lower than the co-polarization ($T_{xy} < T_{yy}$), see Fig. 3-2 (b). So the transmitted wave will display an elliptic polarization.

Fig. 3-3 (a) and (b) shows the linear-circular transmission coefficients of the basic single layer DSRR (top layer) and the final bilayered structure. It

can be clearly seen that the single layer structure yields the same transmission for the two CP waves. However, the bilayered twisted DSRR shows large differences in the CP transmitted waves. This is put in full evidence in Fig. 3-3 (c) and (d), where the ratio between the two CP transmitted wave amplitudes is shown. For an x-polarized incident wave, the difference between the transmitted waves with different CP can reach a level of more than 30 dB. The curve includes two peaks in the operating band. At 8.8 GHz, the LCP wave dominates the transmitted wave and at 10.3 GHz, the RCP wave is the main component. In the center of the band, the amplitudes of LCP and RCP are nearly the same, which indicates linear-polarization, see also Fig. 3-4 (c). For an y-polarized incident wave, the difference only reaches 15 dB, since the transmitted wave with y-polarization is always much larger than the one with x-polarization, see Fig. 3-2 (b).

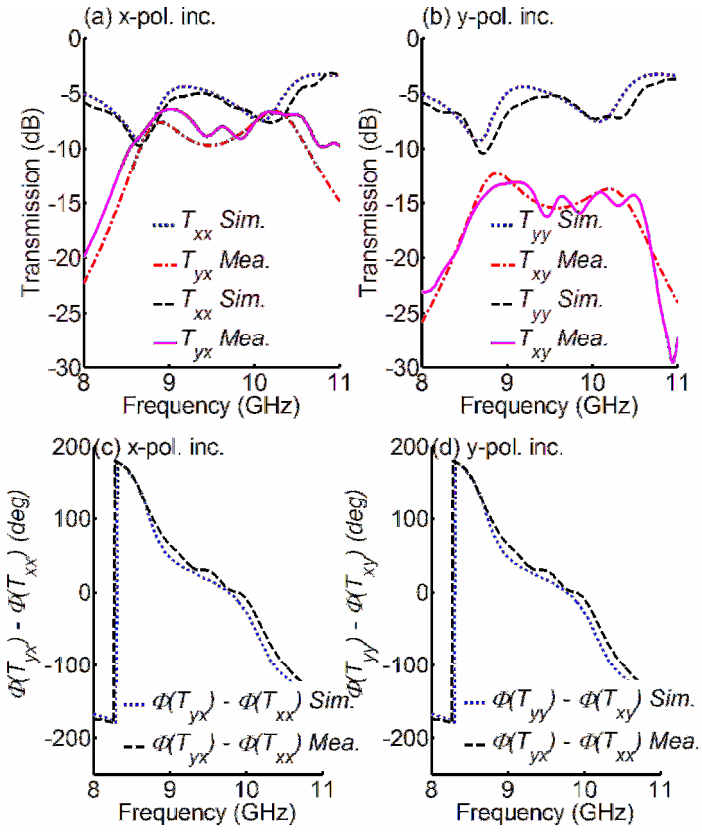

Fig. 3-2. Linear transmission coefficients: (a) and (c) x-polarized incident wave, (b) and (d) y-polarized incident wave.

In general, the transmitted wave can be described as an elliptically polarized wave. For an elliptically polarized wave the polarization azimuth and ellipticity are defined as [139].

$$\theta = \left[\arg\left(E_+\right) - \arg\left(E_-\right)\right]/2 \tag{3.4}$$

$$\eta = \arctan\frac{|E_+| - |E_-|}{|E_+| + |E_-|} = \frac{1}{2}\arcsin\frac{|E_+|^2 - |E_-|^2}{|E_+|^2 + |E_-|^2} \tag{3.5}$$

respectively. θ represents the angle between the major axis of the ellips and the x-axis. η describes the polarization of the wave. For a pure circularly polarized wave η equals 45°, and for a pure linearly polarized wave η = 0°. When η is larger than zero, the wave is left-handed, otherwise it is right-handed.

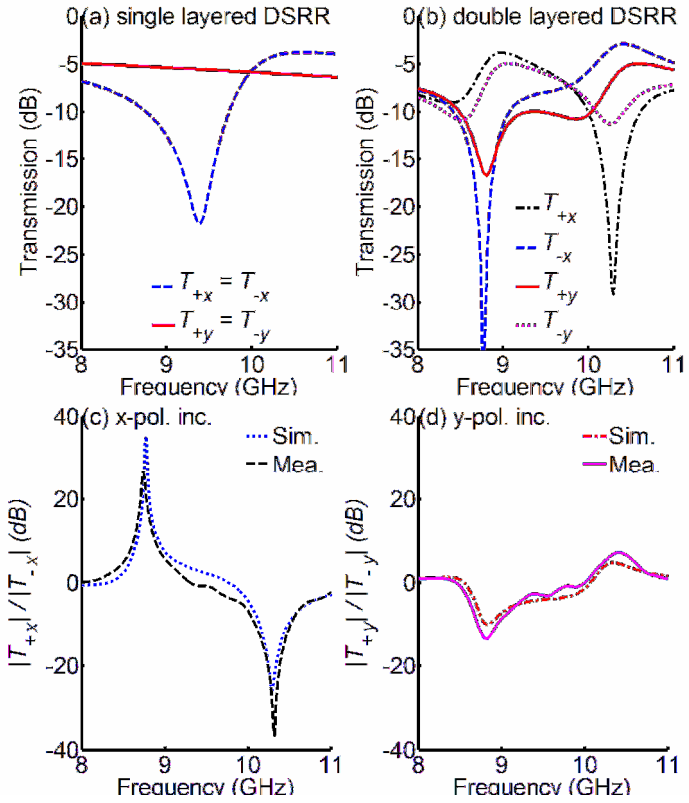

Fig. 3-3. Top: simulated linear-circular transmission coefficients: (a) single layer DSRR, (b) double layered DSRR with 90° twisted angle. Bottom: simulated and measured difference between the transmitted LCP and RCP waves: (c) x-polarized incident wave, (d) y-polarized incident wave.

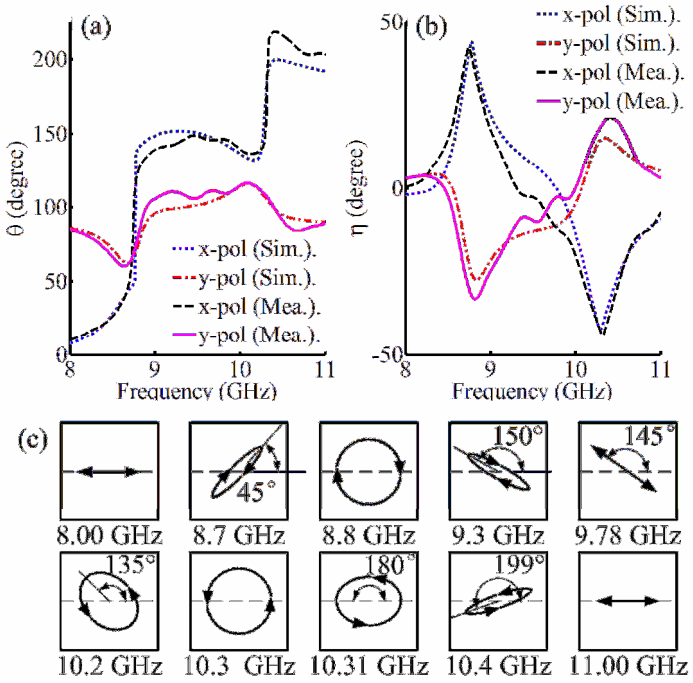

Fig. 3-4. (a) Polarization azimuth, (b) Ellipticity of transmitted wave for x-polarized and y-polarized incidence, respectively, (c) Several polarization states of transmitted wave for x-polarized incidence (waves are coming out of the paper).

These two parameters are shown in Fig. 3-4 (a) and (b) for x-polarization and y-polarization incidence, respectively. Several polarization states for x-polarized incidence are plotted in Fig. 3-4 (c). Incident and transmitted wave have the same linear polarization at low frequencies (8 GHz). Near the resonant frequency, the transmitted wave becomes left-handed elliptical, and its major axis rotates with respect to x-axis. At 8.8 GHz the wave becomes left-handed circular. After that, the wave continues rotating and stays left-handed elliptical up to 9.78 GHz, where a linear polarization is formed with an angle of 145° with respect to the x-axis. After that, the transmitted wave becomes right-handed elliptical. At 10.3 GHz, it is right-handed circular, and then, it becomes gradually linearly polarized.

We also fabricated a sample with no twisted angle between the two layers (the gaps have the same relative position in the top and bottom DSRR). The simulated and measured results both show that the LCP and RCP transmitted waves have the same amplitudes and phases, since the structure does not have any chirality.

An extra noticeable advantage of this structure is its compact size. At 8.8 GHz the size of the unit cell is only $\lambda_0/9.74 \times \lambda_0/9.74 \times \lambda_0/42.6$. That is not only extremely thin in the z direction, but also very small in the transverse directions. The small size of the unit cell is very advantageous in a lot of applications where the polarizer needs to be integrated with other compact devices, like electrically small antennas and small sensors.

3.2.3 **Physical explanation**

In each DSRR, two modes are possible. One is the dipole (current) mode, see Fig. 3-5 (a). This occurs when the excitation (electric field) is along the direction C connecting the two gaps. The presence of the gaps has no direct effect on this mode, since it does not interrupt the current flow. Also, this mode does not show a resonance, as can be seen from the straight line response in Fig. 3-3 (a). The other mode is the "gapped" loop current mode, further called the gapped mode. This occurs when the excitation is along the direction normal to C. "Gapped" means that this mode can actually be seen as a fixed superposition of a dipole mode normal to C, and a "full" loop mode (or a magnetic dipole, involving a current flowing along the full loop), see Fig. 3-5 (b). The currents of these two exactly cancel at the position of the gaps. The gapped mode is thus only possible thanks to the presence of the gaps. This mode does show a resonance around 9.4 GHz, see Fig. 3-3. Due to the 90° spatial rotation of the two DSRRs, the dipole current mode of one couples to the gapped mode of the other.

An x-polarized normally incident wave excites the gapped mode in the top DSSR and the dipole mode in the bottom DSSR. The top gapped mode can be decomposed into its dipole and full loop constituents. The dipole part couples to the dipole mode at the bottom, but more importantly, the full loop part couples to the full loop mode (and thus automatically to the gapped mode) at the bottom. The latter is actually the inductive coupling between two overlapping full loops. Gapped modes are thus excited in both DSSRs. The transmission behavior can be explained based on the resonance around 9.4 GHz for the single DSSR in Fig. 3-3 (b). The stacking results in a splitting of the basic resonance in two, one with a parallel and the other with an anti-parallel character. [140, 141]When the frequency changes the relative amplitudes and phases of these two modes also change. The phases are such that at 8.78 GHz LHCP and at 10.3 GHz RHCP is obtained. The resulting charge and current distributions at these two frequencies are given in Fig. 3-6. For both resonant frequencies, clearly only gapped modes are observed. In the top layer, the phases of the current and charge are quasi the same at

the two frequencies. In the bottom layer however, there is a clear 180° phase difference between the two frequencies. The current flow is indeed parallel at the lower frequency and anti-parallel at the higher frequency. This explains different transmitted circular polarizations.

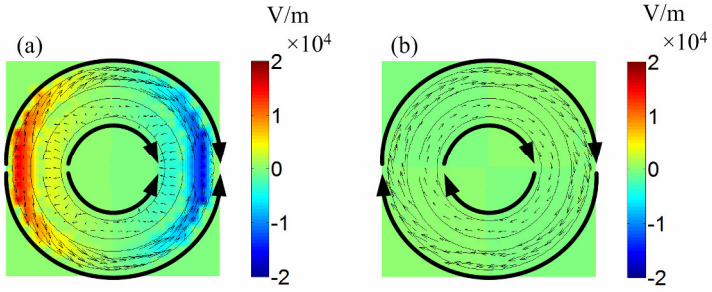

Fig. 3-5. z-component of the electric field distribution (directly related to surface charge), depicted in color, and surface current flow, depicted with arrows, (a) dipole mode,(b) "full" loop mode.

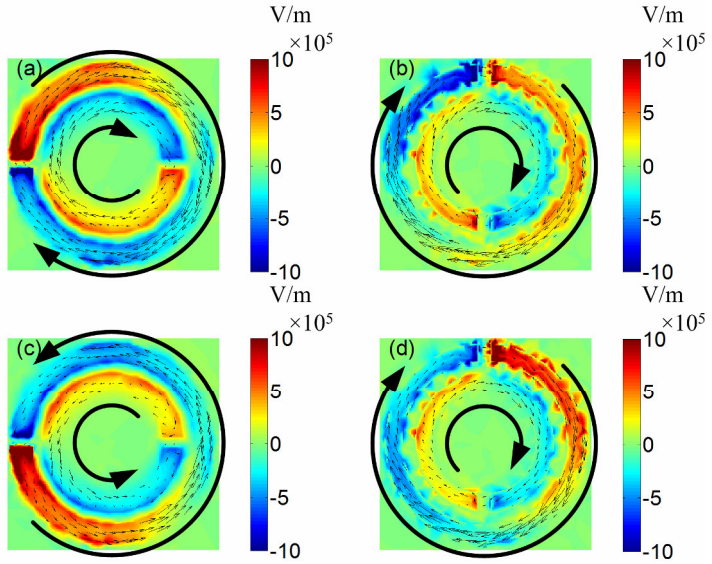

Fig. 3-6. z-component of the electric field distribution (which is directly related to surface charges) near the resonant frequencies. The arrows indicate the directions of the surface current flow. (a) on bottom layer at 8.8 GHz, (b) on top layer at 8.8 GHz, (c) on bottom layer at 10.3 GHz, (d) on top layer at 10.3 GHz.

3.3 CHIRAL STRUCTURE BASED ON BILAYERED DISPLACED U PAIR

A type of bilayered chiral structure is introduced. Whereas common bilayered chiral structures are based on rotation, our design is based on the displacement between two U topologies on different layers. This displacement breaks the symmetry of the pattern and generates the chirality. Prototypes are fabricated in the microwave frequency band. Simulated and measured results agree well. Both optical activity and circular dichroism are observed for circularly polarized waves. The amplitude and phase differences for the transmission coefficients of the circularly polarized waves can reach more than 12 dB and 40° at about 13.4 GHz, respectively. Since the chirality of the bilayered structure can be easily controlled by moving the position of one of the two layers, this topology can be used in the designing of tunable chiral metamaterials.

3.3.1 Topology and theoretical description

The unit cell of the proposed structure is shown in Fig. 3-7 (a). Each cell is composed of a pair of stacked U-shapes. The U structures in the two layers have displacements in both x and y direction (Δx and Δy). The unit cell parameters are defined in Fig. 3-7 (b).

The structure is modeled and simulated with the frequency domain solver in CST Microwave Studio, which is based on the finite element method (FEM). Unit cell boundaries and Floquet ports are used in the model. The measured results are obtained by a vector network analyzer (Agilent 8510C) in a transmission measurement set-up using two standard gain horn antennas (Narda microwave-east standard gain horn 639).

Assuming that the incident and transmitted wave are

$$\overrightarrow{E^i} = \begin{pmatrix} E^i_x \hat{x} \\ E^i_y \hat{y} \end{pmatrix} e^{jkz} \tag{3.6}$$

and

$$\overrightarrow{E^t} = \begin{pmatrix} E^t_x \hat{x} \\ E^t_y \hat{y} \end{pmatrix} e^{jkz} \tag{3.7}$$

they are related by the linear transmission matrix T_l as

$$\begin{pmatrix} E^t_x \\ E^t_y \end{pmatrix} = \mathbf{T}_l \begin{pmatrix} E^i_x \\ E^i_y \end{pmatrix} = \begin{pmatrix} T_{xx} & T_{xy} \\ T_{yx} & T_{yy} \end{pmatrix} \begin{pmatrix} E^i_x \\ E^i_y \end{pmatrix} \tag{3.8}$$

The transmission matrix for circularly polarized waves can be expressed as

$$\begin{aligned}\mathbf{T}_c &= \begin{pmatrix} T_{++} & T_{+-} \\ T_{-+} & T_{--} \end{pmatrix} \\ &= \frac{1}{2}\begin{pmatrix} (T_{xx}+T_{yy})+i(T_{xy}-T_{yx}) & (T_{xx}-T_{yy})-i(T_{xy}+T_{yx}) \\ (T_{xx}-T_{yy})+i(T_{xy}+T_{yx}) & (T_{xx}+T_{yy})-i(T_{xy}-T_{yx}) \end{pmatrix}\end{aligned} \tag{3.9}$$

where the subscripts + and - represent the right-handed polarized (RCP) and left-handed polarized (LCP) waves, respectively.

3.3.2 **Simulated and measured results**

In the prototype, the U structures are etched on the two sides of an FR4 board (ε_r = 3.8, tan δ = 0.025) with thickness 0.8 mm. The sample is composed of 30 × 35 unit cells, making the total size of the PCB equal to 15 cm × 17.5 cm. A photo of the sample is given in Fig. 3-7 (c).

Since the U-shape shows symmetry along the x-axis, only position shifting in y-direction cannot break the symmetry, and thus does not introduce chirality. So a shift in the x-direction is firstly analyzed. Δx is chosen 1.55 mm. The resulting transmission coefficients of the LCP and RCP waves are given in Fig. 3-8 (a). Around 13.8 GHz the difference between them can clearly be seen. The amplitude and phase differences are characterized by Δ and δ, respectively.

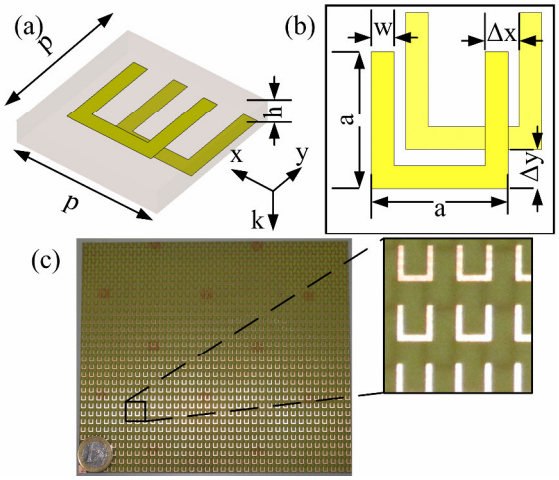

Fig. 3-7 (a) The unit cell topology of the bilayered chiral structure. (b) Parameters of the unit cell. (c) Photo of the prototype fabricated (a zoomed in unit cell is shown): h = 0.8 mm, p = 5 mm, a = 3 mm, w = 0.5 mm.

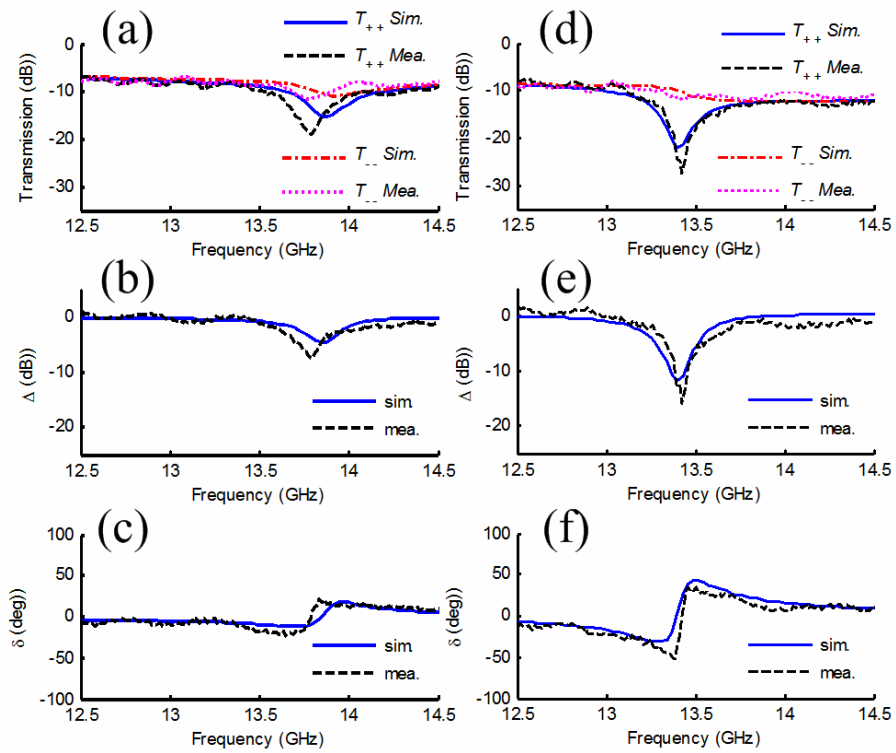

Fig. 3-8. Transmission coefficients of the structure (a), (b) and (c), Δx = 1.55 mm, Δy = 0 mm; (d), (e) and (f), Δx = 2 mm, Δy = 2.5 mm.

$$\Delta = |T_{++}| / |T_{--}| \tag{3.10}$$

$$\delta = \arg(T_{++}) - \arg(T_{--}) \tag{3.11}$$

Fig. 3-8 (b) and (c) show these two parameters in the operating frequency band. The difference between the two CP waves can reach 4.8 dB and 17° in amplitude and phase, respectively.

A sample with only position shifting in y direction (Δx = 0) was also analyzed. The simulated results show that the LCP and RCP transmitted waves have the same amplitudes and phases, since the structure does not have the necessary asymmetry.

If the two U resonators on the different layers have a displacement in both x and y direction, a much more significant effect can be observed. In Fig. 3-8 (b), Δx = 2 mm and Δy = 2.5 mm. It is seen that the amplitude and phase differences reach values of 12 dB and 43° near 13.4 GHz, respectively, which is much larger than for the structure with displacement in x direction

only. This is caused by the more significant asymmetric pattern in the structure. Considering that the thickness of the sample is only 0.8 mm, such chirality is remarkable.

The effective parameters of the structure in Fig. 3-8 (d) are calculated based on the retrieval method. [134] The results show that the effective refractive index can reach about 0.15 at 13.5 GHz for the RCP wave, which is much lower than for the LCP wave. So the presented bilayered structure can be used as a zero-index metamaterial. Its chirality is not enough to support negative index. This can be reached for example with the twisted bilayered structure. [134, 142]

In principle, the same method can be used in other frequency bands to generate chirality, the Tera-Hertz band, even the IR and the optical band, because the break of the symmetry by displacement is the essential reason of the chirality. However, at these high frequencies, the larger losses in the metals may have a reducing effect on the results. An example is given in Fig. 3-9. The permittivity of the gold is described by a Drude model with plasma frequency ω_{pl} = 1.37×1016 s-1, and damping constant ω_c = 4.08×1013 s-1. The refractive index of the substrate PC 403 n_{PC403} = 1.55. [141] A significant difference is obtained between the LCP and RCP wave in this simulated result, of the same order of magnitude as at microwave frequencies (Fig. 3-8 (d)).

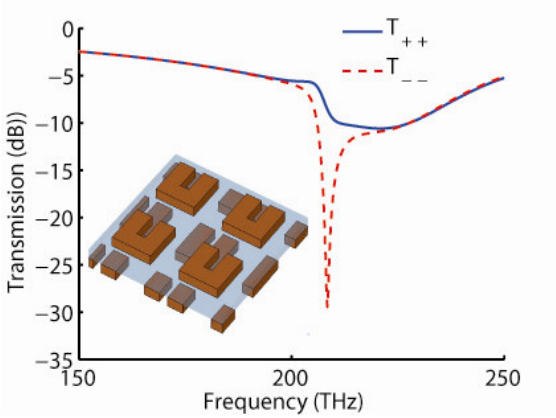

Fig. 3-9. Performance of the displaced U pair topology at THz frequencies. The physical parameters are p = 400 nm, a = 230 nm, w = 90 nm, h = 50 nm, the thickness of the gold is t = 50 nm.), Δx = 150 nm, Δy = 200 nm.

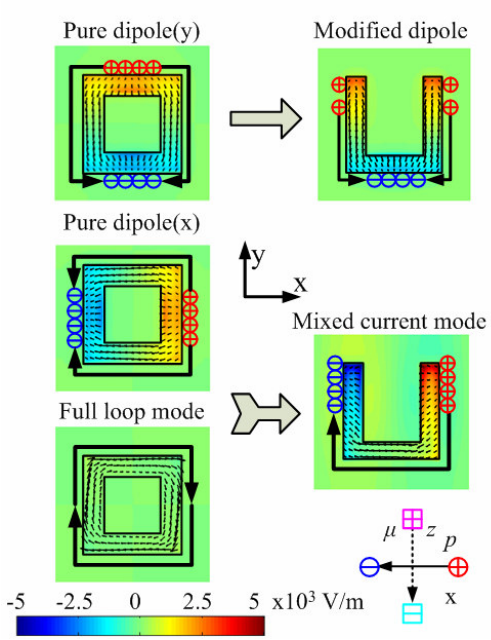

Fig. 3-10. Electric current modes on the square and U structures, the color represents the z-component of the electric field distribution (directly related to surface charge), the arrow indicates surface current flow.

3.3.3 **Physical explanation**

In general the constitutive relations can be expressed as

$$\begin{bmatrix}\mathbf{D}\\ \mathbf{B}\end{bmatrix}=\mathbf{X}\begin{bmatrix}\mathbf{E}\\ \mathbf{H}\end{bmatrix}=\begin{bmatrix}\chi_{EE} & \chi_{EH}\\ \chi_{HE} & \chi_{HH}\end{bmatrix}\begin{bmatrix}\mathbf{E}\\ \mathbf{H}\end{bmatrix} \tag{3.12}$$

For materials without chirality, only the diagonal entries in the matrix **X** are not zero ($\chi_{EE} \neq 0$, $\chi_{HH} \neq 0$, $\chi_{EH} = \chi_{HE} = 0$). This means that the electric field (**E**) cannot cause a magnetic flux (**B**), and vice versa, the magnetic field (**H**) cannot induce an electric displacement field (**D**). However, for a CM, the χ_{EH} and χ_{HE} are no longer zero. Electric field and magnetic field can induce each other. This coupling is one way of explaining chirality.

In a complete and isolated square, there are three main electric current modes, the pure dipole modes in x- and y-direction, and the full loop mode (see Fig. 3-10 left). In the U shape, the pure dipole mode in y-direction is slightly distorted due to the fact that the upper edge of the square is missing. The result is the "modified" dipole current mode (see Fig. 3-10, right top). This mode essentially still generates y-directed electric fields, just as the pure dipole mode in y-direction. The pure dipole mode in x-direction is

considerably altered. The fact that the upper edge of the square is missing gives rise to a "mixed" current mode, which is a combination of the original pure dipole mode and a full loop mode, in such a way that the current in the missing edge is annihilated (see Fig. 3-10, right bottom). In other words, it is a superposition of an electrical dipole moment p in x-direction, and a magnetic dipole moment μ perpendicular to the loop in z-direction.[141] The electric dipole moment p generates x-directed electric fields. The magnetic dipole moment μ generates z-directed magnetic fields and a rotational electric field in the xy-plane.

The "modified" dipole mode is excited when the incident electric field is along the y-direction, which is the direction along the legs of the U shape. In the operating frequency band, this mode does not show a resonance. The "mixed" current mode occurs when the exciting electric field is along the base of the U shape (in x-direction). This mode does resonate at about 13.4 GHz. From symmetry considerations, it is clear that none of the two current modes described for the U structure can generate chirality.

In general, the stacking introduces capacitive coupling between the U's of the top and bottom layer. Capacitive coupling means the formation of dipole charge distributions. The nature of the capacitive coupling is, and thus the dipoles are, totally depending on the relative positioning of the stacked U's, and thus on the displacement between the layers. This capacitive coupling introduces a deformation of the charge distributions, and thus current modes, in this way breaking the symmetry. The formation of these dipolar charge distributions in the U's in the two layers is the main cause of chirality. This is clearly illustrated in Fig. 3-11, where the charges on the U's are depicted for the case $\Delta x = 2$ mm, $\Delta y = 2.5$ mm and for an incident field in x-direction. For the bottom layer (Fig. 3-11 (b) and (d) at the right), only the "mixed" current mode can be seen, generating the corresponding dipole charge distribution (with phase 90°). Note that a current distribution has a phase shift of 90° with respect to its charge distribution. However, for the top layer (Fig. 3-11 (a) and (c) at the left) not only a smaller "mixed" current mode with phase 90° is seen. Where the tips of a U of the bottom layer approach the bottom of a U of the top layer, an extra asymmetric dipolar charge distribution is formed, due to capacitive coupling. The corresponding current thus shows a net y-directed dipole moment with phase 0°, see p_a in Fig. 3-11 (c). This means that an incident x-directed electric field is generating an outgoing y-directed field component. According to (7), together with proper phase relations between the transmission coefficients, this is a prerequisite to generate chirality.

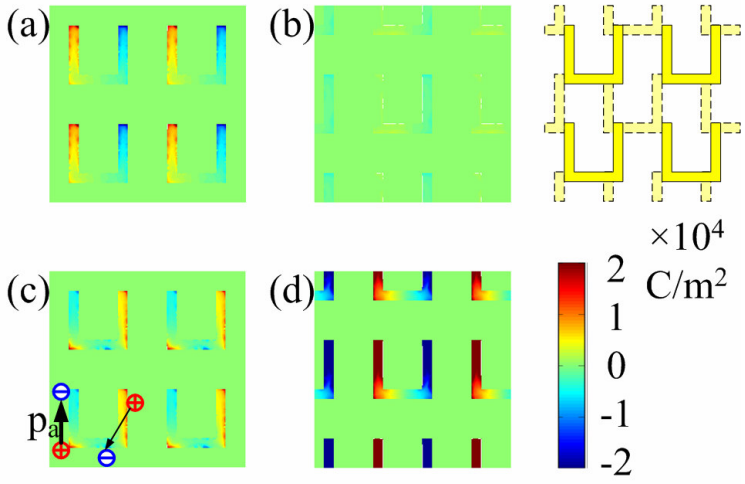

Fig. 3-11. Charge distribution in the bilayered U structures for the case Δx = 2 mm, Δy = 2.5 mm: a) top layer at phase 0°, b) bottom layer at phase 0°, c) top layer at phase 90°, d) bottom layer at phase 90°.

3.3.4 **Tunable chirality**

Another advantage of this kind of chiral structure is its tunability. Several kinds of tunable CMMs have been designed already. They may even contain active devices.[130, 131] The most common one is based on silicon. The conductivity of a silicon substrate can be controlled by a laser, which modifies the transmission characteristics of the structure. Since this method requires a controllable substrate and a laser source, it is only available in the THz frequency band. In the microwave or optical band, it is less straightforward to change the properties of the substrate. Another tunable CMM based on rotation of the two layers is presented in.[143] The control can be performed by a Micro Electronic Mechanical System (MEMS). However, the huge disadvantage of this technique is that the rotation of the two layers with respect to each other inherently breaks the periodicity of the structure. This makes it extremely difficult to analyze and adds thus considerable challenges in the design of such structures. The chiral structure proposed in this paper is based on the displacement of total layers which respect to each other. This keeps the periodicity of the whole structure and makes the design much easier.

In Fig. 3-12 the displacement of the two layers is changing. The physical parameters of the structure are the same as in Fig. 3-7. In Fig. 3-12 (a), the displacement in y direction is kept Δy = 2.5 mm, and Δx is changing from 0 mm to 2.5 mm. When Δx is zero, Δ is also zero due to the symmetry of the structure itself. Then Δ grows with Δx up to Δx = 2.0 mm where a peak value is observed in the curve. This phenomenon is caused by the ascending asymmetry induced by the displacement in the bi-layered structure. After this maximum, Δ drops down sharply to zero at Δx = 2.5 mm (half the period) where the structure shows an asymmetric pattern. If Δx is negative (a shift in the other direction), the amplitude of Δ remains but its sign changes.

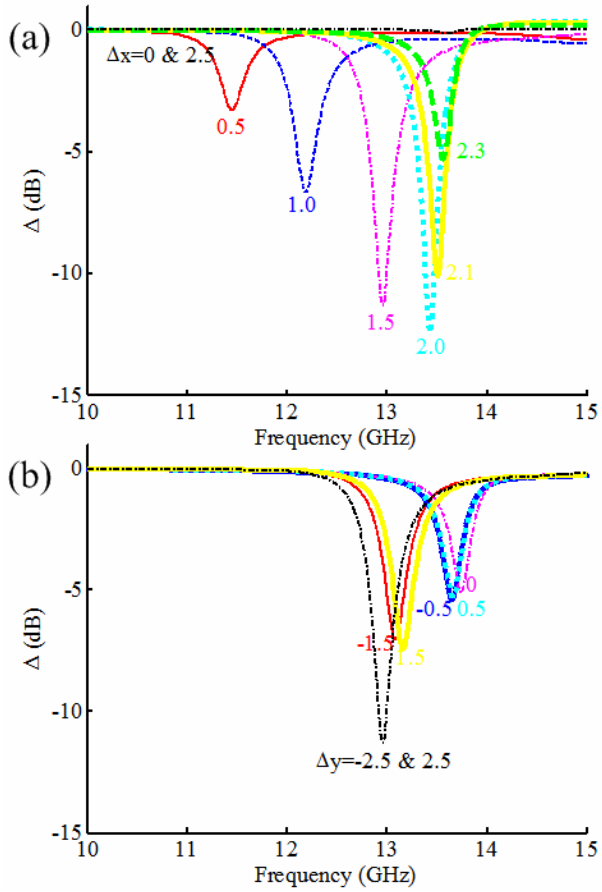

Fig. 3-12. The amplitude difference for different displacements. (a) Δy = 2.5 mm, (b) Δx = 1.5 mm.

In Fig. 3-12 (b), Δx is kept 1.5 mm. Since the U shape resonator is asymmetric in y direction, Δ shows small differences for positive and negative Δy. The peak of Δ shifts much less compared to the previous case, but the amplitude of the shift Δ is of the same order of magnitude.

By changing the displacement in the bilayered structure both in x and y direction, the peak frequency and max (Δ) are tunable over a large range. It has to be emphasized that this is a simple method to design chirality in CMMs.

The four-U structure of [142] can be treated as four displaced U pairs with different orientations. This structure needs a twist between the different layers, with as a result a very strong chirality, larger than for the presented structure. However, in our topology chirality is reached only by the displacement. The displacement, and thus the chirality, is then very easy to tune. This is much more difficult in case of the four-U structure, since in practice its rotations cannot be changed in a straightforward way.

3.4 CONCLUSION

Two kinds of chiral structures are studied in this chapter. One is based on the bi-layered twisted DSRRs and the other one is based on a pair of displaced U-shape resonators. Both of them break the pattern symmetry and show huge chirality. The unit cell of these structures is not only extremely thin in the longitudinal direction, but also very small in the transverse directions. Prototypes are fabricated and measured. The numerical and measured results agree well. The physical working mechanisms behind these phenomena observed are also explained, based on the current and charge distributions in the structures. In real applications, the first design can be used as a polarizer which can convert a linearly polarized wave into a pure circularly polarized wave. The second one can be used in tunable CMMs whose chirality can be easily controlled by a mechanical displacement between the two layers. A circular patch antenna with this technology designed for GPS applications is presented in a master thesis supervised by the author [144].

Chapter 4

AN ENCAPSULATING META-MOLECULE: U RESONATOR CONTAINING SPIRAL LINE

A new kind of planar metamaterial is investigated. It consists of meta-molecules where a first resonator encapsulates a second resonator. The near-field coupling between these resonators is the dominating effect determining the characteristics of the material and is discussed in detail at a physical level. The technique of encapsulating allows both to miniaturize the unit cell, which is advantageous with respect to making the material homogeneous, and to invoke strong coupling, which is advantageous for tuning the material.

This chapter is based on the following publication:

[1] S. Yan, and G. A. E. Vandenbosch. "An encapsulating meta-molecule: U resonator containing spiral line", Japanese Journal of Applied Physics (JJAP), 53. 11 (2014) 110306.

4.1 INTRODUCTION

A MM usually consists of periodic deep subwavelength resonators, called meta-atoms, that are carefully designed in order to get unique functionalities at specific frequencies. Some basic meta-atoms are the split ring resonator (SRR) [7, 145], the U shape resonator [88, 146], the spiral roll [7, 147], the dielectric sphere [98, 133], etc.. They provide properties like negative refractive index (NRI) [6, 121], huge chirality [34, 120, 121, 148], asymmetric transmission [149, 150], and even large nonlinear properties [37, 38]. Similar to natural materials, several meta-atoms can be combined into a meta-molecule. The properties of a meta-molecule are not the mere sum of the properties of each meta-atom, since there may exist a strong interaction between them. Exploiting this coupling forms a new route in MM design that may provide very interesting new properties. [141, 151]

The interaction between two elementary meta-resonators is studied by several groups. In general, due to the electromagnetic coupling between meta-atoms, the resonances of a meta-molecule will differ from to the ones of the constituting atoms. [141, 152, 153] A common phenomena is that the resonance splits into two resonances, one with a “parallel current” nature and one with an “anti-parallel current” nature. [153] In general, when a planar wave is incident on a planar screen consisting of such meta-molecules, a narrow transmission band can be found in the center between these two hybrid resonances [141]. This transmission window usually has a high quality factor and a sharp dispersion. Both these phenomena have a lot of applications in engineering. In the microwave frequency band, sharp resonances are used in filters [32, 33, 154], artificial delay lines [154], or polarizers. [30, 34]In the optical spectrum, they can be used in sensitive sensors. [155, 156]

In this chapter, we investigate a new type of meta-molecule introduced recently: the encapsulating meta-molecule [157]. This structure consists of a first resonator encapsulating a second resonator, in this way forming a compact unit cell. The typical dimension of the meta-molecule is smaller than one sixth wavelength. Due to the near-field interaction between the two resonators, a hybridization of the resonances is obtained, splitting the spectrum, with a narrow transmission window in the wide stop band. A U shape element acts as the first resonator and a spiral line acts as the second one. In contrast to [157], the meta-molecule shows strong polarization dependence. Different distances between the two resonators, including the

important case of overlapping topologies, and the corresponding coupling are studied. It is proven that the concept of overlapping yields very promising results. Not only the distance between the atoms, but also the period of the unit cell is shown to seriously influence the coupling. The working mechanism is explained at a physical coupling level, based on the current modes that occur in the structure, and not just at a circuit equivalent level. The near-field distribution is inspected for each situation in order to verify the physical mechanisms behind this phenomenon. To the knowledge of the authors, the concept of encapsulation within a single unit cell is quite new and has not been studied in detail. This endows this design with potentials in highly integrated devices, like electrically small antennas or small sensors.

The proposed structure is etched on an FR4 printed circuit board (PCB) (relative permittivity ε_r = 3.8, thickness 0.8 mm). The meta-molecule is composed of a U shape resonator and a spiral line. The physical parameters of the unit cell are shown in Fig. 4-1. The structure is simulated with the frequency domain solver in the commercial software CST MWS. Periodic boundaries and Floquet ports are used in the model.

The reflection and transmission coefficients for x- and y-polarized incident plane waves in case of the single U resonator, the single spiral line, and the meta-molecule, respectively, are plotted in Fig. 4-2, top. The component of the electric field normal to the structure Ez, which is related to the charge distribution in the structure, is depicted at several frequencies in Fig. 4-2, bottom.

4.2 SIMULATED AND MEASURED RESULTS

When the incident wave is parallel to the legs of the isolated U (x-direction), no resonance can be found in the operating frequency band (below 15 GHz). However, when the incident wave is perpendicular to the legs of the U (y-direction) a wide resonance can be observed around 9.155 GHz. The Ez distribution (Fig. 4-2 (d)) shows a looped current mode at this resonant frequency. Since the current on the U clearly realizes a superposition of an electric dipole moment in y-direction and a magnetic dipole moment in z-direction [11,20], the structure is strongly coupled with the y-directed incident wave. The efficient radiation of this U resonator makes the Q factor low, resulting in a wide stop band.

In the isolated spiral line, a resonance can be seen at 9.035 GHz for the x-directed incident wave. The Ez distribution in Fig. 4-2 (e) reveals that this

mode is the current loop mode of the spiral line. Also for the y-directed incident wave, a very small dip can be observed. The Ez distribution (not shown) shows a similar pattern as the former one, but its intensity is much weaker. This difference is caused by the orientation of the gap in the spiral line, which is in x direction. The current loop mode is the dark mode under a y-direction incident wave for this spiral line.

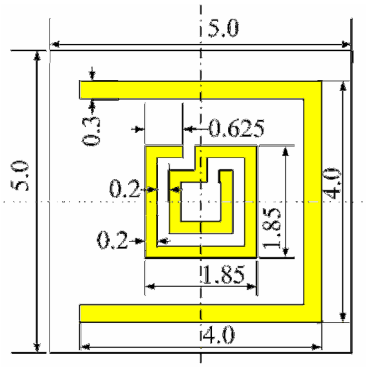

Fig. 4-1. The unit cell topology of the meta-molecule (dimensions in mm). The U shape resonator and spiral line are concentric.

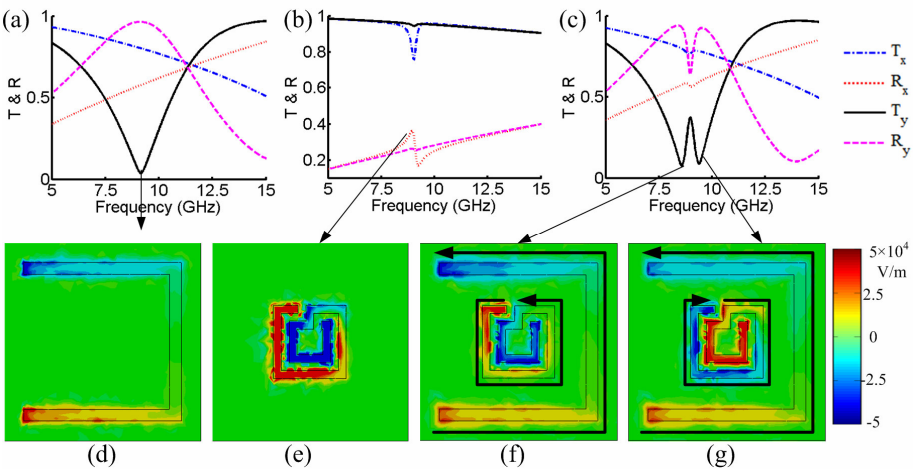

Fig. 4-2. Top: the transmission and reflection coefficients of the U resonator, the single spiral line, and the meta-molecule are shown in (a), (b) and (c), respectively. Bottom: the Ez distribution in the U resonator for y-polarization at 9.155 GHz. (d), in the single spiral line for x-polarization at 9.035 GHz (e), in the meta-molecule for y-polarization at 8.57 GHz (f) and 9.38 GHz (g). The arrow indicates the direction of the surface current flow.

Next, the U shape and the spiral line are brought together to form a meta-molecule. The two resonators are placed concentrically. Their orientation is shown in Fig. 1. The transmission and reflection coefficients of the structure are shown in Fig. 4-2 (c). For the x-directed incident wave, the results are similar to the U resonator, except for a little perturbation at about 8.93 GHz caused by the spiral line. For the y-directed incident wave, from the results for the isolated structures we know that the U shape resonator is excited directly, and that the spiral line is hardly directly excited. In the meta-molecule, the physical working mechanism is as follows. The U shape resonator is excited firstly, yielding a loop current on the U shape, and thus a magnetic dipole moment in z-direction. This magnetic dipole moment excites the spiral line. Due to this near-field interaction between the two resonators, the spectrum splits into two peaks, representing a symmetric mode, and an antisymmetric mode. [141, 152] Fig. 4-2 (f) and (g) illustrates these modes. The parallel current at the lower frequency and the antiparallel current at the higher frequency can be clearly seen in these two figures. The narrow transmission window appearing in the center between these two frequencies is an electromagnetically induced transparency (EIT) [151, 155]. This phenomenon will be discussed in detail in the next section.

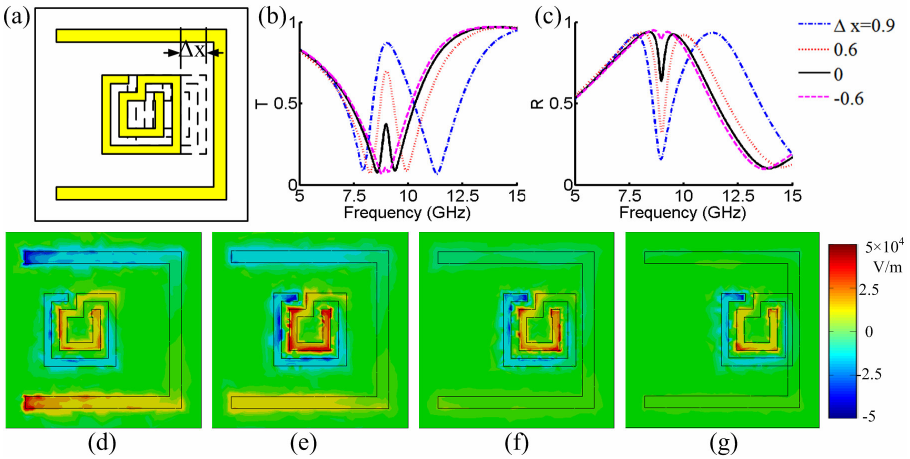

Fig. 4-3. (a) Schematic diagram of the displacement of the spiral line. (b) and (c) The transmission and reflection coefficients of the meta-molecule for y-polarization. (d), (e), (f), and (g) E_z distribution for the displacements -0.6, 0, 0.6, and 0.9 mm, respectively, at 8.975 GHz.

4.3 PARAMETER STUDY

In a meta-molecule the near-field interaction between the two resonators is the cause of the splitting of the resonance. Obviously, the distance between the two meta-atoms will influence the strength of this coupling and thus has to be studied.

Consider a displacement of the spiral line Δx, see Fig. 4-3. When Δx is positive the spiral line is moving towards the U resonator, and the coupling between them increases. Conversely, for a negative Δx the spiral line is moving away from the U resonator, which will reduce the coupling. Fig. 4-3 (b) and (c) compare four situations, Δx = -0.6 mm, 0 mm 0.6 mm, and 0.9 mm. The incident wave is y-polarized. The split of the spectrum becomes clearer and wider as the coupling increases. Meanwhile, the transmission window is becoming wider and higher. Fig. 4-3 (d)-(f) illustrates the Ez distribution at the peak of the transmission window. It can be seen that, relatively, the major part of the energy is stored around the spiral line when the coupling is strong, see for example Δx = 0.6 mm in Fig. 4-3 (f). The U shape stores only little energy and hardly influences the transmission. Since the spiral line is nearly dark under the y-directed incident wave, it can hardly couple with the electromagnetic wave directly. So the total meta-molecule also only slightly couples with the incident wave, which means that is almost transparent for the y-directed incident wave (Fig. 4-3 (b) shows that the transmission coefficient can reach about 0.7 at this point).

When Δx = 0.9 mm, which means that the arms of the spiral line and the U resonator overlap, the split of the resonance results in resonant frequencies considerably further apart compared with the other situations. The peak of the transmission coefficient reaches 0.87 in between them. The reason is the direct conductive contact, which implies a quasi zero distance, and thus also corresponds to a high inherent magnetic coupling, thus the phenomenon is more explicit [153]. At the lower hybridized resonance, the currents on the two overlapping arms are parallel. The result is that the lower resonant frequency shows a redshift. At the higher resonance, the anti-parallel currents on the two resonators totally cancel each other, and the position of the resonance shows a noticeable blueshift. In the center transmission window, the energy distribution will be more concentrated to the spiral line. Since the spiral line is weakly coupled with the incident wave, the transmission shows a much higher and wider bandwidth.

A prototype with Δx = 0.9 mm was fabricated and measured. The sample is composed of 35×50 unit cells, making the total size of the board equal to

17.5 cm × 25 cm. Fig. 4-4 (a) shows both measured and simulated results. The measured results are obtained by a vector network analyzer (Agilent 8510C) in a transmission measurement set-up using two standard gain horn antennas (Narda microwave-east standard gain horn 640). A good agreement is observed except for a little frequency shift. This could be caused by the tolerances on the dielectric constant of the substrate.

The refractive index neff is retrieved from the S-parameters [112] for this planar MM. Fig. 4-4 (b) shows the results, together with the figure of merit (FOM = |Re n_{eff}| / |Im n_{eff}|). A sharp dip in the real part of the effective refractive index is observed at about 8.9 GHz. This is due to the strong variation of the effective permeability around this resonant frequency. At the minimum the real part of neff is about 1, which is much lower than for the background FR4 board (ε_r = 3.8). A high FOM, corresponding to a low imaginary part of the effective refractive index, is observed at 9.23 GHz. A low refractive index can be used to design zero-index resonators for lens and antennas [45, 67].

It should be pointed out that the performance of a metamaterial is influenced by the size of its unit cell. In our structure, it is obvious that two neighboring U shape resonators (a left and a right one) will generate opposite magnetic fields at the positions of the corresponding spiral lines at the left and right, see Fig. 4-5 (c). The inductive effect is partially canceled and thus the current on the spiral line is reduced. Relatively, more energy will be focused around the U resonator, and the corresponding mode will couple with the incident wave and make the transmission become lower. If the period of the unit cell increases, the influence of the neighboring unit cells will be reduced. The transmission window will show a trend to increase, both in amplitude and bandwidth.

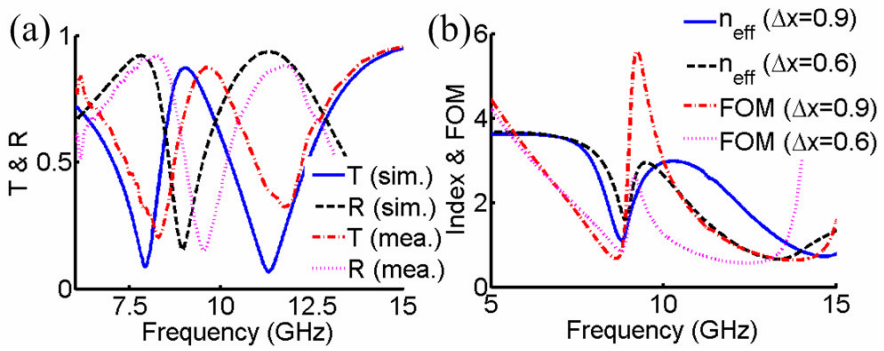

Fig. 4-4. (a) Measured results; (b) The refractive index and figure of merit.

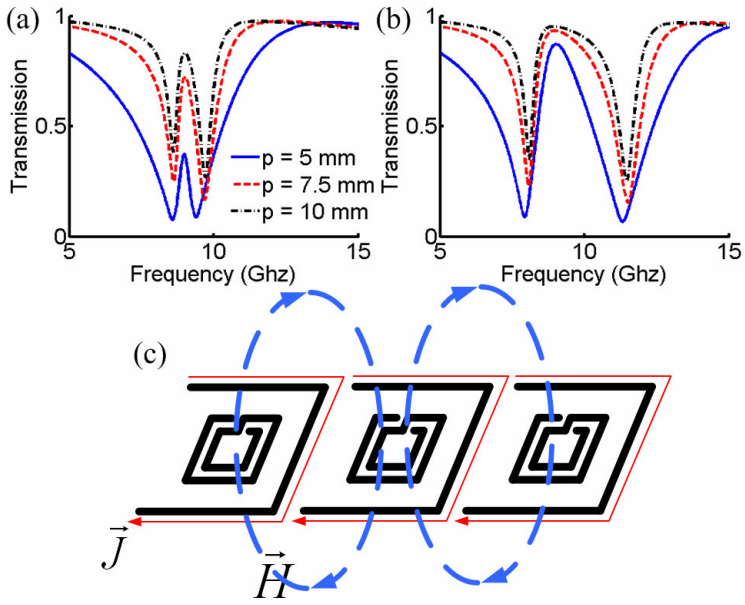

Fig. 4-5. The simulated transmission coefficients for different sizes of the unit cell for Δx = 0 mm (a) and 0.9 mm (b); (c) the coupling effect between two neighboring meta-molecules.

Fig. 4-5 (a) and (b) shows results for different sizes of the unit cell for Δx = 0 mm (left) and 0.9 mm (right), respectively. For the Δx = 0 mm situation, a significant diminution of the transmission window is indeed shown as the period is decreasing from 10 mm to 5 mm. The lower limit of 5 mm is directly related to the physical size of the conducting structure. The upper limit of 10 mm is related to the mutual coupling. For periods larger than 10 mm, the coupling is weak enough and no significant difference can be observed any more. For the Δx = 0.9 mm situation, the transmission only displays a slight decline. The reason is that the current distribution is concentrated on the center spiral line, see Fig. 4-3 (g). The U resonator does not seem to be excited since it does not carry any significant current. It is thus unable to contribute to any serious inductive coupling between unit cells. This means that the interference between the two resonances inside the unit cell (which creates the peak in the middle) is much less influenced by the mutual coupling between unit cells. This effect could be helpful in the design of miniaturized meta-molecules.

4.4 CONCLUSION

In conclusion, we present a new topology for a meta-molecule composed of a U shape resonator with an embedded spiral line inside. We demonstrate the coupling effect between these two resonators. The transmission spectrum splits due to the near-field interaction and two hybridized modes are formed, a symmetric and an antisymmetric one. A narrow transmission window is observed in the wide stop band. The relation between near-field interaction and the distance between the two resonators and the size of the unit cell is studied, leading to physical mechanisms explaining the phenomena observed. Although the structure in this letter is designed for ca. 10 GHz, it can also be realized at THz frequencies. This new topology may find its applications in the design of frequency selective surface (FSS) with high quality and small sensitive sensors. A refractive index based sensor based on this topology has been proposed in [157].

Chapter 5

TEXTILE DUAL-BAND ANTENNA BASED ON COMPOSITE RIGHT/LEFT-HANDED TRANSMISSION LINE

In this chapter, two types of textile patch antennas loaded with metamaterial structures are proposed for WLAN / WBAN applications. The concept of composite right/left-handed transmission line (CRLH TL) is introduced in the textile antenna. The occurring symmetric resonances cause the similar field distributions and radiation patterns in the two operating bands. Since the antennas are based on the microstrip patch topology, they feature a low backward radiation and low specific absorption rate (SAR) value. The antennas are fabricated fully using textile materials, and show flexible character and robust performance.

This chapter is based on the following four publications:

[1] S. Yan, P.J. Soh and G. A. E. Vandenbosch. "A wearable dual-band composite right/left-handed (CRLH) waveguide textile antenna for WLAN applications", Electronics Letters, 50. 6 (2014): 424-426.

[2] S. Yan, P.J. Soh and G. A. E. Vandenbosch. "Made to Worn", Electronics Letters, 50. 6 (2014): 420.

[3] S. Yan, P.J. Soh, and G. A. E. Vandenbosch. "Compact All-textile Dual-band Antenna Loaded with Metamaterial Inspired Structure", IEEE Antennas and Wireless Propag. Lett., doi: 10.1109/LAWP.2014.2370254.

[4] S. Yan, P.J. Soh, and G. A. E. Vandenbosch. "Performance on the Human Body of a Dual-Band Textile Antenna loaded with Metamaterials", European Conference on Antennas and Propagation, Lisbon, Portugal, April 2015.

5.1 INTRODUCTION

5.1.1 Wearable antennas

Over the past decade and in many sectors of society, wearable devices have attracted more and more attention. Wearable electronic systems are very attractive for e.g. continuous medical monitoring, emergency rescue services, physical training, care for children and the elderly, etc.. As a consequence, the concept of Wireless Body Area Networks (WBAN) has become a more widespread research topic. As a critical component of these systems, the wearable antenna plays a key role for the wireless communication with other devices on or off the body. However, the design flowchart for wearable antennas is quite different compared to the traditional ones. First, the electromagnetic coupling between the human body and the antenna will influence the performance of the antenna, but also poses questions related to potential health risks in case of long term irradiation of the human body. Secondly, different deformations, e.g. bending, crumpling, and wrinkling, need to be considered in the antenna design, especially if textile materials are used for the antenna. Next, although the properties of wearable materials are not necessarily stable when the body and clothes environment changes, the functions of the antennas should be robust under these conditions. Moreover, low profile, light weight, user comfort, mechanical robustness, low cost, and fabrication simplicity are essential characteristics for wearable antennas.

Considering the isolation between the antenna and human body, a piece of metal plane is usually required to shield one from the other. This leads to two types of wearable antennas. One is the patch or cavity antenna, and the other one is the reflective antenna. [65, 158, 159] In this chapter, we will discuss the former. The latter will be studied in section 7.2.

The microstrip patch antenna topology is a good candidate for wearable devices, since it is usually low profile and easy to fabricate. The large ground layer under the patch reduces the coupling between the human body and antenna, and enhances forward radiation. Several textile antennas based on the patch topology have been previously proposed and investigated on body [160-162]. When a dual-band function is needed, the patch antenna may be loaded using slots, lumped components, parasitic patches, or be stacked [39, 40, 42]. The first two methods will change the current distribution on the patch resulting in radiation distortion. The side radiation may then induce high coupling with the human body. Parasitic patches may significantly increase antenna size whereas stacked patches result in

fabrication complexity when using textile materials. Recently, another technology, i.e. substrate integrated waveguide (SIW) antennas [163-165] was also proposed for wearable applications. Despite obtaining good efficiencies and low body-coupling over a wide bandwidth, it also suffers from pattern distortion in dual-band operation. Indeed, the essence of SIW antennas is still a cavity antenna as the microstrip patch antenna.

5.1.2 Composite Right/Left-Handed Transmission Line

Recently, the use of CRLH-TL [45] has been introduced, yielding a new way for designing miniaturized antennas [73]. In essence, a CRLH-TL is a kind of metamaterial (MM). Unlike volumetric metamaterials made of resonant structures [6, 133], a CRLH TL is a kind of planar non-resonant TL, which is easily fabricated on printed circuit board (PCB) with etching technology. By loading the host TL with series inductances and shunt capacitances, the propagation constant (β) can be made positive, zero, or even negative. The unique dispersion relation can be easily used to design several kinds of patch antennas for special applications.

The concept of the ZOR antenna was first presented in 2003 by C. Caloz and T. Itoh [44, 166]. Rectangular patches integrating mushroom structures have been analyzed in detail by C-J. Lee and A. Lai in 2006 and 2007 [167, 168]. The input impedances and radiation characteristics were obtained for different unit cells. The dispersion diagram in CRLH structures has also been analyzed with other methods. [52, 169] Several kinds of dual-band antennas based on CRLH TL have been designed based on different resonant modes [52, 170, 171]. However, to the knowledge of the authors, the textile antenna version has never been studied before.

Using microstrip line (ML) technology to implement a CRLH TL, the left handed inductor (L_L) and capacitor (C_L) can be realized by surface mount technology (SMT) chip components or distributed components, while the right handed inductor (L_R) and capacitor (C_R) are induced by the host TL itself. Since the SMT elements are lossy and take only discrete values, they are not suitable for adjusting the phase shift accurately compared with the distributed components. However, components based on printed planar technology are also not ideal. It is usually hard to obtain a balance between the size of the components and the values of the parameters. Several topologies already have been proposed to solve this issue [172], like shorted stub inductors, meander-line inductors, virtual ground capacitors, interdigital capacitors, and mushroom structures.

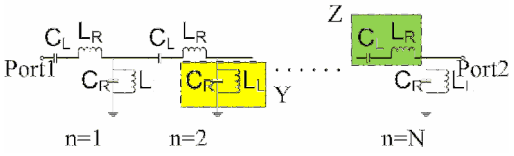

Fig. 5-1 Circuit model of CRLH TL. [43, 44]

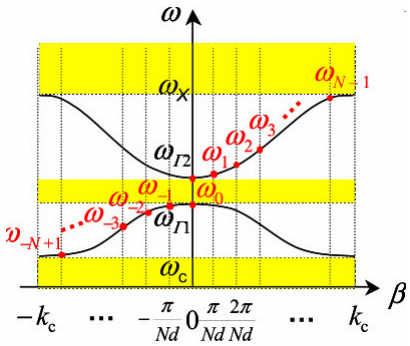

Fig. 5-2. Typical dispersion relation of the CRLH TL. The resonant frequencies of a open/short CRLH TL resonator are plotted with dots. [43, 44]

The dispersion characteristics of a CRLH TL shown in Fig. 5-1 can be obtained using the Bloch-Floquet periodic boundary condition

$$\beta(\omega)=\frac{1}{p}\cos^{-1}\left(1+\frac{ZY}{2}\right) \tag{5.1}$$

Since the electrical length of the unit cell (p) is much smaller than the wavelength, a Taylor approximation can be applied and we get

$$\beta(\omega)=s(\omega)\sqrt{\omega^2 L_R C_R+\frac{1}{\omega^2 L_L C_L}-\left(\frac{L_R}{L_L}+\frac{C_R}{C_L}\right)}, \tag{5.2}$$

where s (ω) is the sign function decided by the frequency.[45]
Consider a section of CRLH TL with open or short boundary. The resonance will occurs under the condition

$$\beta_n=\frac{n\pi}{Np}, \qquad n=0,\pm1,\pm2,\cdots\pm N-1 \tag{5.3}$$

where N is the number of unit cells. These resonant frequencies are labelled in Fig. 5-2. Among these resonances, we are more interested in two points. One is the zeroth order resonance (ZOR) and the other is the first negative resonance (n = -1). At the ZOR mode, the effective wavelength is infinite and its resonant frequency is independent with the physical dimension. The antenna can be designed much smaller than half a wavelength in order to

reach a compact size, or much larger than half a wavelength in order to reach high directivity. Unlike the traditional patch antenna, the open-ended ZOR antenna usually has an omnidirectional radiation pattern in the patch plane, also called monopolar radiation pattern. This kind of pattern radiation pattern is undesirable for wearable antennas, and it will be discussed in section 6.3 in detail.

In this chapter, we will firstly study the first negative resonance. Since a pair of symmetric resonant modes (± n) has similar field distributions, they will have similar radiation patterns at these two resonant frequencies. Since the dispersion relation of the CRLH TL can be easily controlled by tuning the effective circuit parameters in the unit cell, the frequencies of the two symmetric modes can be designed for different applications.

The radiation pattern of the wearable antennas should be directed outwards from the users' body to avoid dielectric coupling and ensure minimal absorption by the body, so the $n = \pm 1$ modes will be used to get the radiation pattern similar as for the normal microstrip patch antenna. In this chapter, two types of textile antennas will be proposed based on SIW and microstrip line topologies, respectively. The SIW antenna will have a wider bandwidth, but a larger size also compared to the microstrip patch. So the SIW antenna is more suitable for locating on the user's chest and back, and the microstrip patch is competitive when the antenna needs to put on the leg, arm or wrist. The performances of the antennas are studied both in free space and on body. The deformations of the antenna and SAR values are also considered.

5.2 WEARABLE DUAL-BAND CRLH WAVEGUIDE TEXTILE ANTENNA

A dual-band textile antenna based on the CRLH planar waveguide structure [173] is proposed for WLAN / WBAN applications. This planar waveguide structure is capable of providing a "negative permittivity" below its cut-off frequency. Meanwhile, a meander slot loading in the patch is used to generate a negative permeability around its resonant frequency. The CRLH model enables the generation of similar near-field distributions and analogous radiation patterns for two modes, traditionally called the positive and the negative mode, which is desirable for wearable antennas. To our best knowledge, this antenna is also the first CRLH waveguide antenna produced fully using textile, except for its feeding connector.

5.2.1 **Antenna topology and materials**

The antenna topology is presented in Fig. 5-3. A 3 mm thick felt substrate is used [174] (with a relative dielectric constant of 1.3, and a loss tangent of 0.044), and a 0.17 mm thick ShieldIt Super conductive textile from LessEMF Inc. [175] (with a conductivity of 1.18×10^5 S/m) forms the ground plane, radiating components, and the two shorting walls of the planar waveguide. The attachment of ShieldIt to the felt substrate is performed by heating the adhesive available on the reverse plane of the ShieldIt. An SMA connector feeds [176] the planar waveguide from its rear, avoiding any radiation pattern distortion that would be caused by microstrip or co-planar waveguide feeds. The feed position mainly determines the antenna's input impedance. Other physical parameters are labelled in Fig. 5-3 (a) and the fabricated prototype is shown in Fig. 5-3 (b).

5.2.2 **Antenna Performance in Free Space**

The commercial full-wave electromagnetic simulator CST Microwave Studio [177] is used in the design. The simulated and measured reflection coefficients are shown in Fig. 5-4 (a). Three significant bands can be observed, corresponding to the first negative mode (n = -1), infinite wavelength mode (n = 0), and the first positive mode (n = +1), respectively. In our design, modes n = -1 and n = +1 are adopted for WLAN as they generate radiation patterns similar to a classical microstrip patch antenna, with minimal backward radiation.

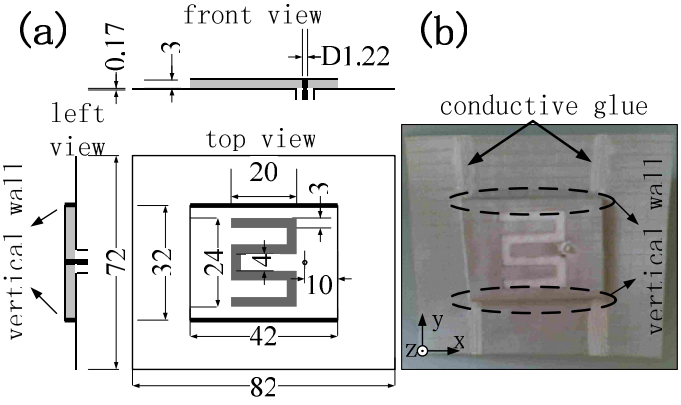

Fig. 5-3 Antenna topology. (a). Physical dimensions in mm, (b). Fabricated antenna prototype.

The simulated result agrees well with the measured curve when the antenna is placed in free space. The n = +1 mode shows a larger frequency bandwidth compared to the simulated one. The reasons are the larger relative inaccuracy by which the dielectric loss of the felt is known and the relatively larger inaccuracies due to the manual fabrication procedure employed. The latter may be improved by dimensioning using machine or laser cutting. Note the very small differences in Fig. 5-4 (a) when the antenna is measured on a volunteer's chest and back, respectively, compared to free space.

The measured radiation patterns shown in Fig. 5-4 (b)-(e) agree well with the simulated ones. Consistent with our previous predictions, microstrip-like radiation patterns are featured in both the low and the higher bands, along with very low cross polarizations and backward radiations. A summary of the antenna performance, including its gain, is presented in TABLE 5-I.

To better understand the two antenna operating modes, simulated electric field distributions (at z equal to half the substrate height) for the n = ±1 modes are presented in Fig. 5-5 (a) and (b), respectively. In both modes, a standard wave is seen along the direction of the wave propagation in the waveguide. The equivalent magnetic currents generated by the electric fields at the edges of the waveguide are parallel to each other, thus contributing as dominant radiators. In contrast, the mode n = 0 exhibits anti-parallel equivalent magnetic current sources, see Fig. 5-5 (c). The radiation of the two opposite magnetic current sources will be cancelled in the front direction of the antenna, causing very low radiation efficiency. This is in contrast to metamaterial-loaded patches, whose infinite wavelength mode n = 0 typically generates a monopole-like radiation pattern. [73]

TABLE 5-I
COMPARISON OF SIMULATED AND MEASURED PERFORMANCE.

Mode		**Freq. (GHz)**	**S_{11} (dB)**	**BW (MHz)**	**$G_{real.}$ (dB)**
n = -1 mode	**Sim.**	2.495	-23.6	95	-1.37
	Mea.	2.425	-12.4	68	-1.40
n = +1 mode	**Sim.**	5.452	-13.4	410	4.68
	Mea.	5.470	-24.3	755	5.20

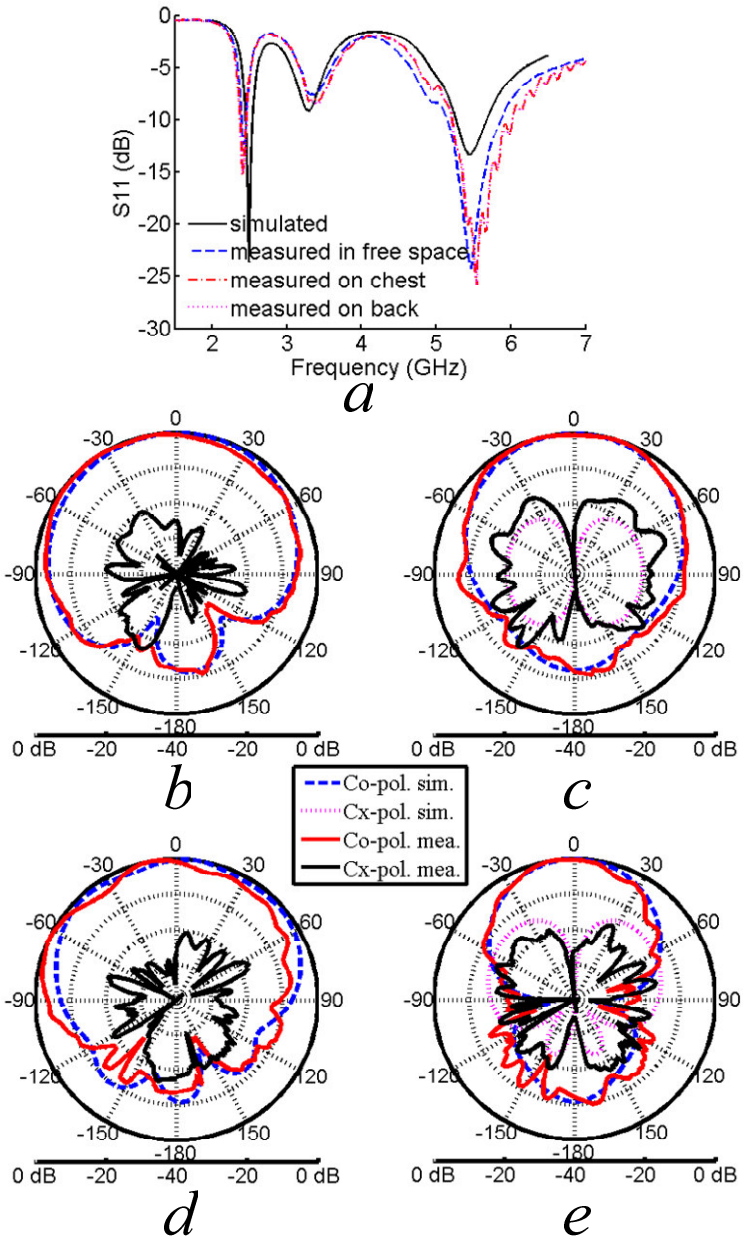

Fig. 5-4 (a) Reflection coefficient. Radiation patterns: (b) in x-z plane in the first band (n = -1), (c) in y-z plane in the first band (n = -1), (d) in x-z plane in the third band (n = +1), and (e) in y-z plane in the third band (n = +1). Simulated cross polarized patterns in *b* and *d* are lower than -40 dB in all directions.

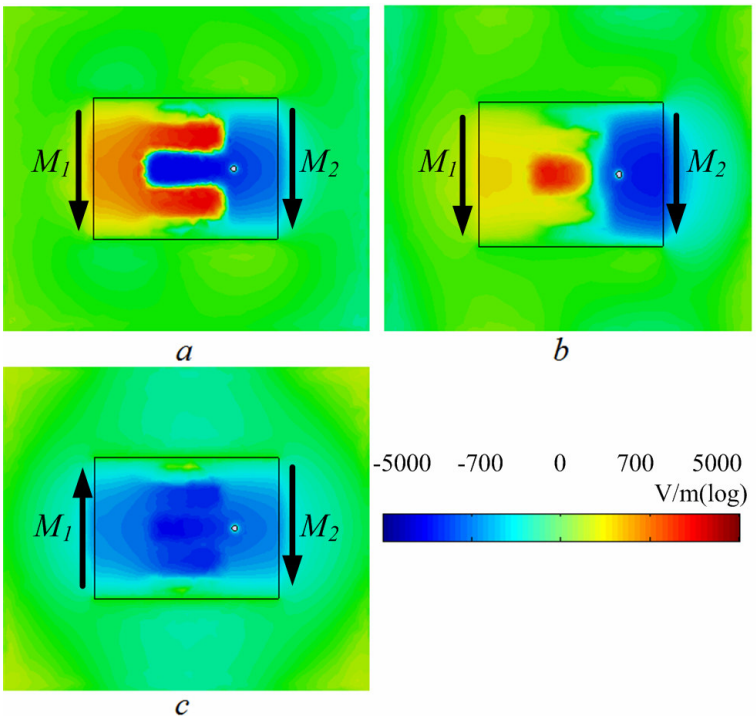

Fig. 5-5 Z-component of the electric field at half the substrate height. (a) negative mode n = -1, (b) positive mode n = +1, (c) infinite wavelength mode n = 0.

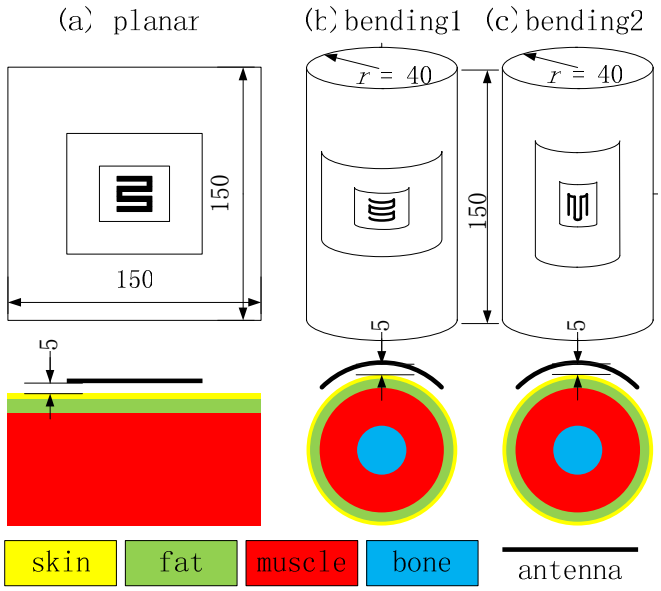

Fig. 5-6 Models of the antenna on top of different human tissue configurations.

5.2.3 **Antenna Performance on human body**

The influence of the human body should be considered in the initial stage of the design of a wearable antenna. In general, this may require huge calculation times and memory. However, since the proposed antenna contains a considerable ground plane under the patch, the coupling between the human body and the antenna is significantly reduced, and consequently the human body will not change the performance of the antenna a lot. Therefore, in these cases the design road map first optimizes the antenna in free space, and then checks its performance on a human body model. If the performance is not satisfactory, the topology of the antenna is modified and a new optimum is searched for.

Two types of human tissue structures are considered in this study, i.e., a planar and a bent structure. The former is used to mimic the chest or back of the human body. It consists of three layers: a 3 mm thick skin layer, a 7 mm thick fat layer and a 60 mm thick muscle layer. The total size of the human tissue is 150 × 150 mm^2, see Fig. 5-6 (a). Meanwhile, the bent tissue imitates the human forearm. Its radius is 40 mm and consists of 4 layers: a 2 mm thick skin layer, a 5 mm thick fat layer, a 20 mm thick muscle layer, and a 13 mm thick bone core. The length of the tissue is 150 mm, see Fig. 5-6 (b) and (c). The properties of the human tissues are listed in Fig. 5-7. Both tissue models have been validated in [159, 178].

In each bending configuration, the antenna is placed 5 mm away from the human body, which emulates the typical thickness of clothes. Fig. 5-7 illustrates the reflection coefficients of the antenna. It is clear that the impedance matching is not sensitive to bending. The performance in the lower band is quite stable, as only a 1.4 % frequency shift is observed for both bending situations. This is mainly caused by the loading of the capacitive slot, which changes only slightly when the patch is bent. For the upper band, the two types of bending result in different behaviors. For bending along the x-axis (bending 1), the resonant frequency and bandwidth are very similar as in the case of the planar structure. On the other hand, the bandwidth is observed to improve under y-axis bending (bending 2), mainly due to the bending of the radiation slot in this direction. Since the antenna is totally shielded by the rear ground, there is a minimal influence of the human tissue on the impedance matching, resulting in stable resonant frequencies and bandwidths when worn on a human body.

The radiation patterns of the antenna in free space and on the human body are illustrated in Fig. 5-8 and Fig. 5-9, respectively. In general, the radiation

pattern is quite stable. Bending will ultimately change the shape and spacing of the two radiation slots, thus slightly decreasing both the directivity and gain. It can also be noticed that when the antenna is operated near human tissue, the radiation efficiency decreases due to the losses caused by power absorption in the tissues. However, its directivity may marginally increase since the tissues are a form of lossy conductors, which mimic an increase of the size of the antenna ground. These two factors complement each other, ensuring a stable antenna gain when worn on body.

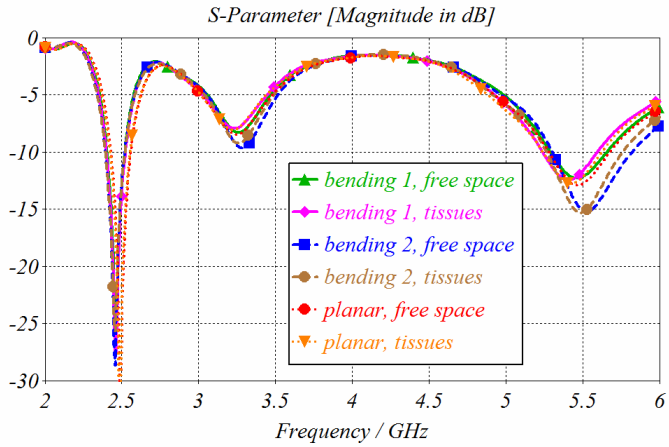

Fig. 5-7 Reflection coefficients of the antenna in different situations.

TABLE 5-II
PROPERTIES OF HUMAN TISSUES

tissues		**skin**	**fat**	**muscle**	**bone**
density (kg/m^3)		1100	910	1041	1850
ε'	**2.45 GHz**	38.05	5.302	53.08	11.42
	5.5 GHz	35.68	5.004	49.66	9.617
ε"	**2.45 GHz**	10.73	0.775	12.89	2.931
	5.5GHz	11.82	1.032	16.99	3.882
thickness (mm)	**planar**	3	7	60	/
	bending	2	5	20	13

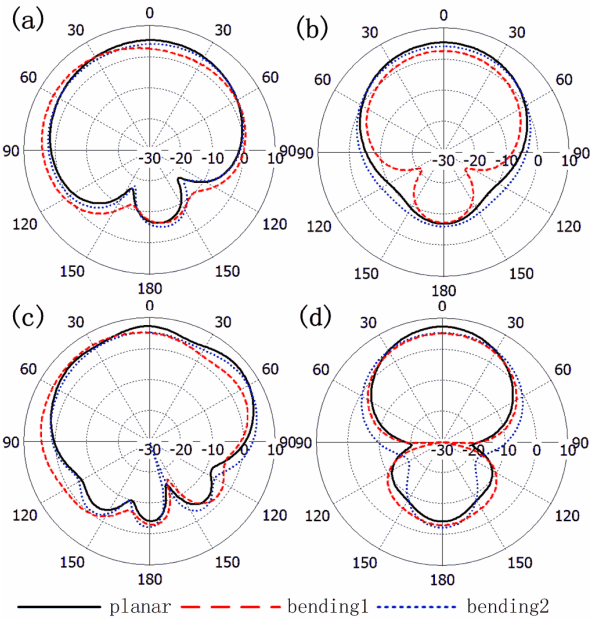

Fig. 5-8 Radiation pattern in free space, (a) x-z plane at 2.45 GHz, (b) y-z plane at 2.45 GHz, (c) x-z plane at 5.45 GHz, (d) y-z plane at 5.45 GHz.

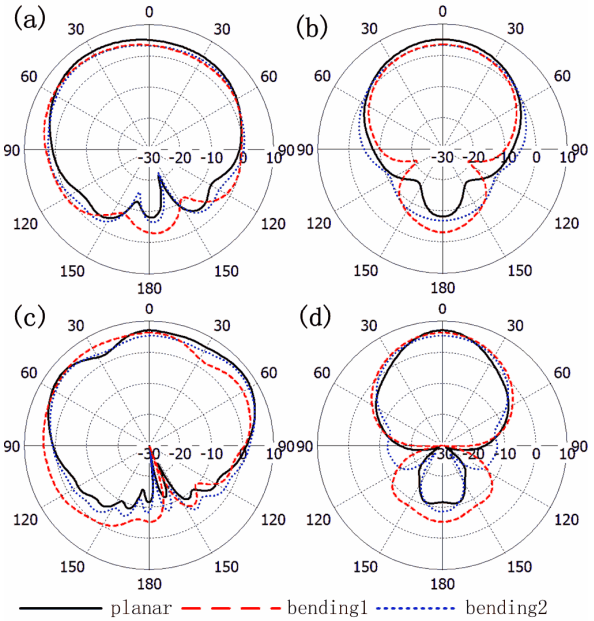

Fig. 5-9 Radiation pattern on human tissue, (a) x-z plane at 2.45 GHz, (b) y-z plane at 2.45 GHz, (c) x-z plane at 5.45 GHz, (d) y-z plane at 5.45 GHz.

The SAR value is calculated based on the IEEE C95.1 standard and averaged over 10 g of biological tissue. The input power to the antenna is 0.5 W (rms). Since the ground plane shields the human body from the radiation from the antenna, the estimated SAR values are far below the European threshold of 2 W/kg at all frequencies. The main performance of the antenna with different configurations are summarized in TABLE 5-III.

A prototype of the antenna was measured on a volunteer's body, see Fig. 5-10. The antenna was located on different parts of the body: the chest, the back, and the arm. It is clearly shown that, since the ground plane shields the antenna, major coupling between the antenna and the human body is avoided, and all results are very similar, even under bending conditions. For the chest and back, the S_{11} almost does not change compared to the result in free space, since the antenna keeps the planar configuration. When the antenna is bended around the arm, a little difference is observed, as predicted by the simulations, especially for the bending 2 situation. The bandwidth of the antenna increases a little bit in the upper band.

TABLE 5-III
COMPARISION OF THE ANTENNA IN DIFFERENT CONFIGURATIONS

			Freq. (GHz)	BW [a] (MHz)	Dir. (dB)	$G_{real.}$ (dB)	$\eta_{radi.}$ (%)	SAR (W/kg)
N=-1 mode (2.45 GHz)	**free space**	**Planar**	2.491	132	4.997	-2.307	19.5	/
		Bend1	2.456	117	5.070	-2.072	19.4	/
		Bend2	2.456	126	4.053	-1.437	28.3	/
	tissue model	**Planar**	2.484	131	6.124	-1.568	17.6	0.068
		Bend1	2.456	123	5.220	-2.361	17.5	0.046
		Bend2	2.456	138	4.860	-1.090	25.5	0.163
N=+1 mode (5.5 GHz)	**free space**	**Planar**	5.466	405	7.261	4.836	60.4	/
		Bend1	5.459	373	6.094	3.765	62.3	/
		Bend2	5.529	522	6.065	4.106	65.7	/
	tissue model	**Planar**	5.424	385	7.529	4.745	56.1	0.176
		Bend1	5.410	359	6.307	3.774	59.9	0.106
		Bend2	5.487	498	6.899	4.656	61.5	0.220

[a] Bandwidth is defined as the -10 dB bandwidt

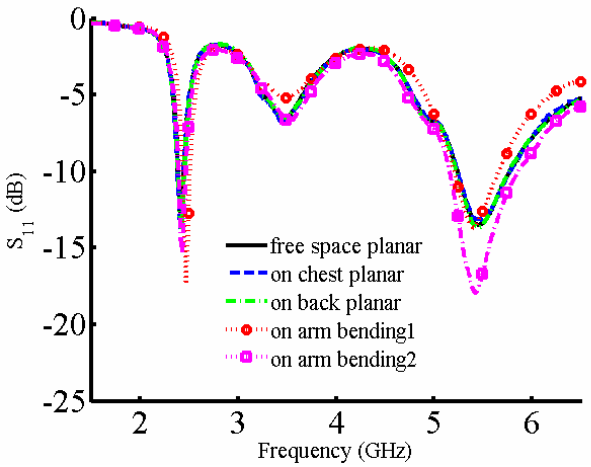

Fig. 5-10 Measured reflection coefficients of the antenna worn on a human body.

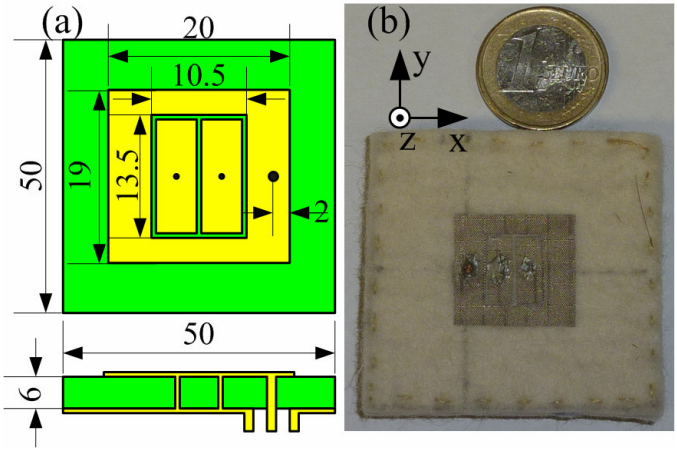

Fig. 5-11 Antenna topology. (a) Dimensions in mm. The width of all slots is 0.5 mm, the thickness of the metal layer is 0.17 mm, and the diameter of the metallic vias is 0.52 mm. (b) The fabricated antenna prototype.

5.3 COMPACT ALL-TEXTILE DUAL-BAND ANTENNA LOADED WITH METAMATERIAL INSPIRED STRUCTURE

A dual-band, wearable metamaterial-loaded antenna is proposed for 2.4/5.2 GHz WLAN applications. [179] The loading is with a composite right/left-handed transmission line (CRLH-TL) metamaterial, resulting in a significant

miniaturization down to $\lambda_0/6\times\lambda_0/6\times\lambda_0/20$. Similar radiation patterns are obtained by simultaneously exciting the first-order positive (n=+1) and negative (n=-1) modes. The antenna features a low backward radiation in both bands, which is highly desirable in minimizing electromagnetic coupling to the body. The antenna is fabricated fully using textiles except for the connector and is evaluated in free space and on body, under both planar and bent conditions. Besides a good agreement between simulations and measurements, results indicate that the proposed topology is reasonably immune to body coupling and robust with respect to mechanical changes. The specific absorption rate (SAR) level is numerically investigated to determine the on-body safety level.

5.3.1 **Antenna Topology and Materials**

The proposed antenna topology consists of a rectangular ring with 19 x 20 mm^2 outer dimensions, centered on a 50 x 50 mm^2 substrate. Two mushroom-like structures with overall dimensions of 10.5 x 13.5 mm^2 are introduced into the slot area at the center of the rectangular ring to form the CRLH-TL structure. These structures are designed on a 6 mm-thick felt substrate [180], with a relative permittivity (ε_r) and loss tangent (tan δ) of 1.3 and 0.044, respectively. A probe is positioned on the rectangular ring to feed the antenna. The antenna topology is shown in Fig. 5-11 (a). A 0.17 mm thick conductive textile, ShieldIt Super from LessEMF Inc. [175] is used to fabricate the metallic layers. Its estimated conductivity is 1.18×10^5 S/m. The vias are fabricated using cylindrical wires of 0.52 mm diameter. [181] To ensure proper galvanic contact from the via-ends to the patch and ground plane, high-frequency conductive epoxy is used. [182] The standard 50 Ω SMA connector [176], which is used here for evaluation purposes, can be easily replaced by a compact mini-coaxial connector which does not affect antenna conformality. A circuit model of this antenna is analyzed and presented in [52]. Numerical simulations were performed using CST Microwave Studio [177], while fabrication was performed using simple dimensioning tools. The fabricated antenna prototype is displayed in Fig. 5-11 (b).

5.3.2 **Antenna Performance in Free Space**

The reflection coefficient of the antenna was measured with a vector network analyzer (Agilent 8510C). The result agrees well with simulations, see Fig. 5-12. Two resonances are observed at 2.45GHz and 5.15 GHz,

corresponding to the first order of the negative mode (n = -1) and positive mode (n = +1). The antenna operates throughout the 2.4 GHz band (2.4 - 2.485 GHz) with at least S_{11} < -8.5 dB, and throughout the 5.2 GHz band (5.15 – 5.35 GHz) with at least S_{11} < -13 dB. At the lower frequency, the patch shows a significant miniaturization down to $\lambda_0/6\times\lambda_0/6\times\lambda_0/20$. The electric field distributions for these two modes are presented in Fig. 5-13. Outside the center region both modes feature a field distribution very similar as on a conventional half-wavelength patch antenna. This already partially explains the similar radiation pattern. Another important observation is the non-excitation of the zeroth order mode of the patch, the mode generating a quasi-monopolar pattern (see the slight dip in the middle of Fig. 5-12). If necessary, this mode can be obtained by adjusting the aspect ratio of the mushroom structure and the patch.

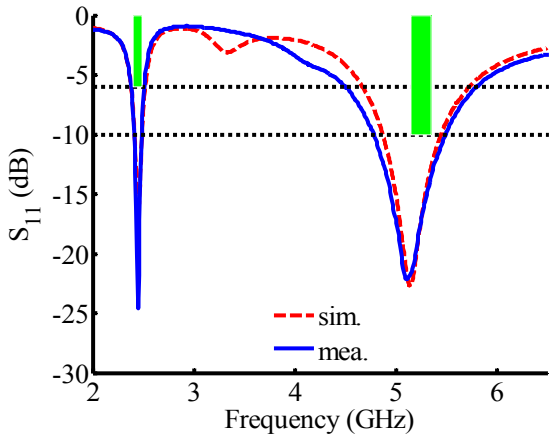

Fig. 5-12 Simulated and measured reflection coefficients.

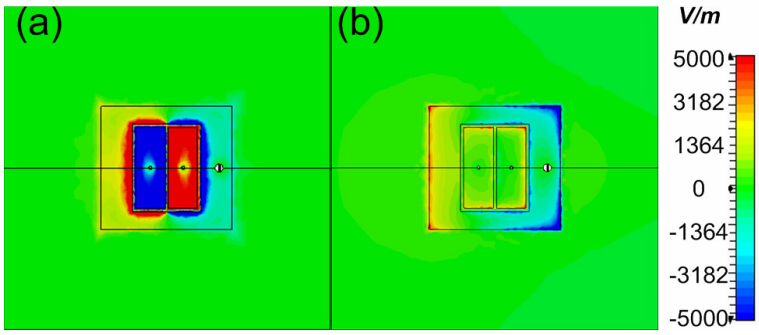

Fig. 5-13 Simulated z-component of electric field distribution at: (a) 2.45 GHz, (b) 5.2 GHz.

The antenna radiation patterns were measured in an anechoic chamber, and compared against simulations in Fig. 5-14. The antenna shows patterns similar to a conventional patch antenna in both operating bands. A higher cross polarization level is observed at oblique angles, and is caused by the fact that the feeding probe has a non-negligible length, especially at the higher frequency. This probe will radiate power as a monopole antenna and form the oblique cross polarization. TABLE 5-IV summarizes the performance of the antenna in both bands.

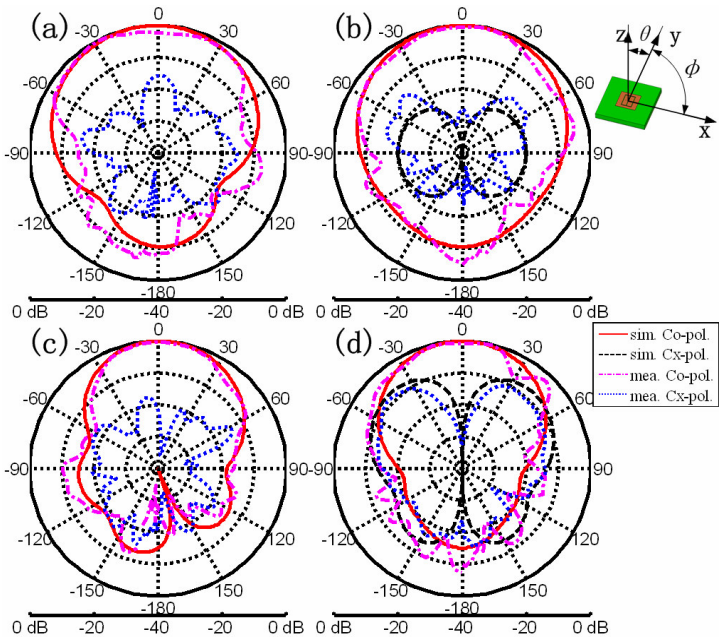

Fig. 5-14 Simulated and measured radiation patterns in the (a) lower band in x-z plane, (b) upper band in x-z plane, (c) lower band in y-z plane, (d) upper band in y-z plane.

TABLE 5-IV
COMPARISON OF SIMULATED AND MEASURED PERFORMANCE.

		Freq. (GHz)	S_{11} (dB)	BW* (MHz)	η_{rad} (%)	$\mathbf{G_{real.}}$ (dB)
Lower band	Sim.	2.450	-25.9	135	17	-3.5
	Mea.	2.447	-24.6	130	/	-3.8
Upper band	Sim.	5.140	-22.6	583	75	6.6
	Mea.	5.112	-22.2	698	/	6.2

*The bandwidth is defined as the band where the reflection coefficient is below -6 dB, for the lower band, and -10 dB for the upper band.

The sensitivity of the design is also studied. The lower band is mainly influenced by the via radius and the size of the inner patch, whereas the upper band can be tuned using the outer patch dimension. To guarantee bandwidth coverage for the two WLAN bands, the tolerance of the outer patch should be better than ± 0.5 mm, while the inner slot tolerance should be better than ± 0.2 mm.

The Q factor is calculated for this antenna, and that is far away from the Chu-Harrington fundamental limit. Two reasons may be responsible for that. The first one is the loss of the textile material, which is significantly higher than normal. The second one is that the antenna is optimized for dual-band operation. It must balance the performance in both bands. Actually, several papers have reported that metamaterials can help antennas to go to the Chu-limit, e.g. [183, 184]. We also proposed a metamaterial based antenna with normal substrate, which shows a better Q factor than the textile antennas [185].

5.3.3 **Antenna performance on human body**

1. Antenna under Bending

Since the antenna is designed to be worn on a user's arm or leg, it is necessary to evaluate its performance under deformations such as bending. The level of antenna deformation is dependent on the bending radius, and this is determined not only by the fact whether it is an arm or a leg, but actually even the exact placement on the limb in question Thus, several bending radii were selected to emulate the randomness of the bending radius of an on-body placement. Fig. 5-15 illustrates the simulated results for antennas placed in proximity of a cylindrically-shaped human tissue model. The cylindrical topology is 150 mm long and consists of three layers: a 2 mm-thick skin layer, a 5 mm-thick fat layer and a muscle core layer [159]. The antenna is centered on this model and located 5 mm away from the tissue surface. As seen in Fig. 5-15 (a), the antenna resonant frequencies are observed to be quite stable. As the bending radius is decreased (indicating further antenna bending), both the lower and higher mode consistently shift up to higher frequencies. However, the level of shifting is almost insignificant: 1.6 % and 1.4 % in the lower and upper band, respectively, when the bending radius is reduced from infinity (planar situation) to 20 mm.

The fabricated antenna prototype was then measured when worn by a human volunteer (176 cm in height and 65 kg in weight). Evaluations were performed on several on-body locations, i.e. the chest, the upper arm and the forearm. The results are shown in Fig. 5-15 (b). Compared to the antenna

performance in free space, the slightly larger bandwidth at the upper band is due to the additional losses as a consequence of the proximity of the human body. Consistent with simulations, the antenna resonant frequency also moves upwards with smaller radii. Nonetheless, bandwidths in both bands are constantly sufficient to enable WLAN operation.

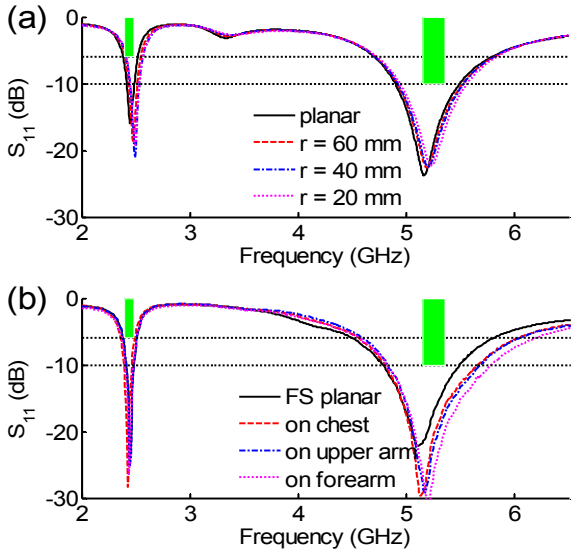

Fig. 5-15 (a) Simulated antenna bent on cylinders with different radii. (b) Measured antenna located on different parts of the human body. (FS: free space)

2. SAR Validation

The SAR level of an on body antenna must be validated in the design stage to ensure conformance to safety regulations. SAR is a measure of power absorbed per unit mass in a human body tissue. It is normally spatially averaged over a certain amount of exposed biological tissue. SAR is calculated using the root mean square (rms) of the electric field strength inside the human body, the conductivity, and the mass density of the tissue. Due to the equipment scarcity and costs involved in experimentally evaluating SAR, numerical evaluation is generally preferred as the means of validation. Moreover, such simulations have been shown to agree well with measurements for textile antennas [186]. The numerical SAR investigation in this work has been performed using CST Microwave Studio, with the antenna located on different parts of a Hugo human body model. [187] These locations are chosen specifically to enable antenna evaluation under different

bending radii. The antenna is bent with a bending radius of 20 mm, 40 mm, 60 mm and 80 mm when placed on the forearm, upper arm, thigh, and chest, respectively, see Fig. 5-16 (e). These bent antennas are placed at 5 mm from the outermost skin layer to mimic the spacing created by air gaps. The input power to the antenna for SAR calculations in this work is set at 0.5 W (rms), and their values were calculated based on the IEEE C95.1 standard, averaged over 10 g of biological tissue. Due to the large problem size (about 50 to 70 million mesh cells), calculations were performed using a workstation with Intel Xeon processors, 48 GB of RAM and an NVIDIA Quadro FX 580 graphic unit. The simulation results are shown in Fig. 5-16 and TABLE 5-V.

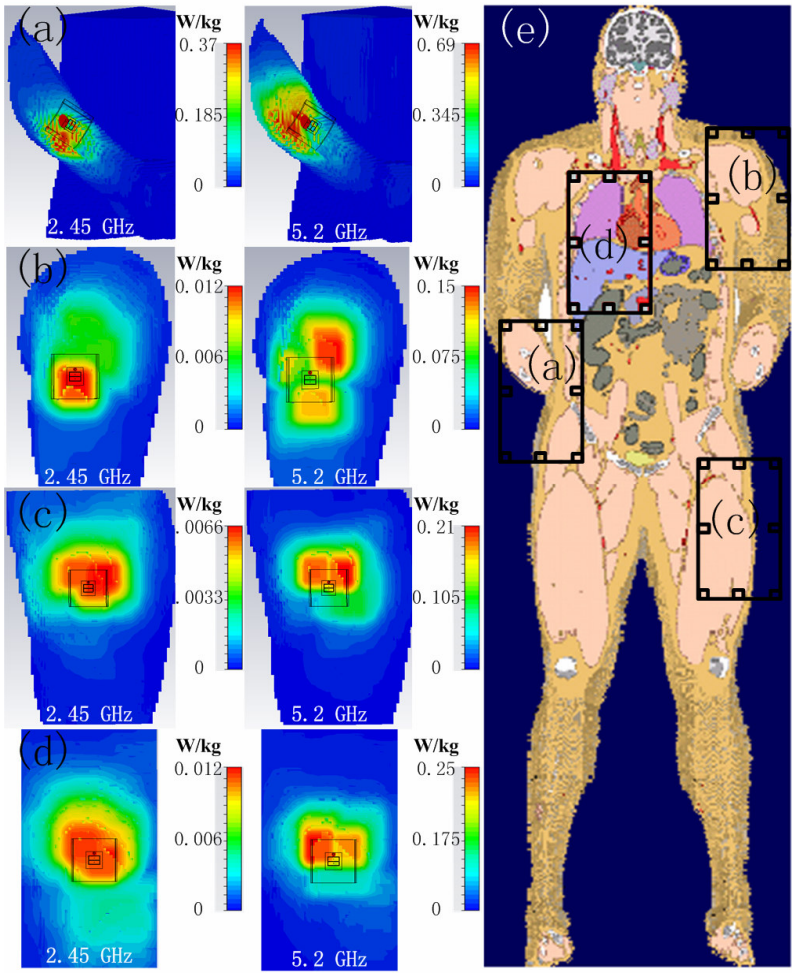

Fig. 5-16 SAR simulation setup and results when placed on the: (a) forearm, (b) upper arm, (c) thigh, (d) chest, (e) antenna locations on the truncated Hugo model.

TABLE 5-V
COMPARISON OF SIMULATED SARS ON THE HUGO MODEL

location	SAR at 2.45 GHz (W/kg)	SAR at 5.2 GHz (W/kg)
Forearm	0.37	0.69
Upper arm	0.012	0.15
Thigh	0.0066	0.21
Chest	0.012	0.25

Generally, the SAR values at 5.2 GHz are higher than at 2.4 GHz for the same bending radius. This is due to the intrinsic properties of the body phantom itself, where conductivity of the same tissue increases with frequency, resulting in the higher SAR. Bending with a radius larger than 40 mm results in very similar SAR values. This suggests that the antenna is robust in both bands regardless of the level of deformation. Most importantly, all evaluated SAR values are far below the regulated European threshold of 2 W/kg averaged over 10 g of tissue.

5.4 CONCLUSION

In this chapter, antennas based on the linear CRLH TL are studied. After a review of the theory of CRLH TL, we designed two kinds of textile antennas using this concept. One is with wider bandwidth and suitable to be located on chest or back. The other one has a more compact size and is prefered to be worn on arm, leg, or wrist. Since the symmetric modes are used to obtain the two operating bands, both of the antennas have similar field distributions and radiation patterns in the two bands. The antennas also feature a high FBR and extremely low SAR values. The overall structures are fully fabricated using textiles except for an SMA connector for evaluation purposes. The two antennas are also calculated on a human body model, and show robust performance for different bending radii.

Chapter 6

RADIAL PATCH ANTENNAS BASED ON COMPOSITE RIGHT/LEFT-HANDED TRANSMISSION LINE

In this chapter, the radial CRLH TL is studied. The circuit model of the radial transmission line loaded with metamaterials is conceived for the first time. Two kinds of antennas are designed, i.e. the circular patch antenna and the sector patch antenna. The proposed full circular patch works at ZOR mode, and its resonant frequency is independent of its physical dimensions. Two prototypes are built, one with an electrical small size and one with an electrical large size, respectively. The sector patch antenna can support a similar ZOR mode without significant performance degradation compared to the full circular patch. A matching network can be easily introduced to enhance the impedance bandwidth. Apart from the ZOR characteristics, this sector topology can also support a quasi-monopolar pattern at multiple modes.

This chapter is based on the following three publications:

[1] S. Yan, and G. A. E. Vandenbosch. "Zeroth-order Resonant Circular Patch Antenna Based on Periodic Structures", IET Microwaves, Antennas & Propagation, 8. 15 (2014): 1432-1439.

[2] S. Yan, and G. A. E. Vandenbosch, "Circuit Model of Circular Antenna Loaded with Composite Right/Left-Handed Transmission Line", The 8th European Conference on Antennas and Propagation, The Hague, The Netherlands, Apr. 2014.

[3] S. Yan, and G. A. E. Vandenbosch. "Meta-loaded Circular Sector Patch Antenna", IET Microwaves, Antennas & Propagation, under review.

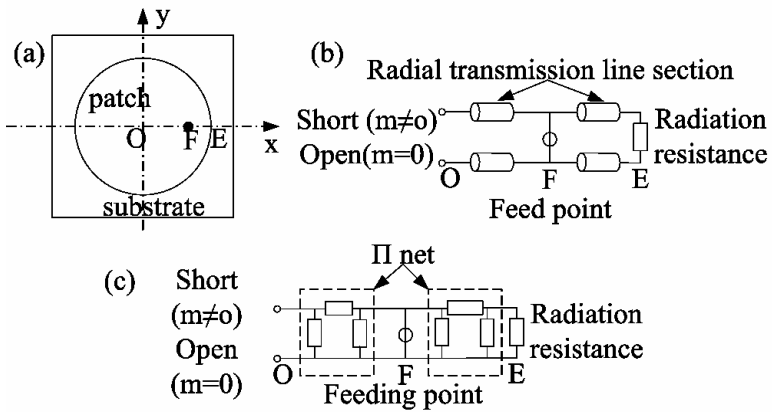

Fig. 6-1. Generalized transmission line model of conventional circular patch antenna. (a) configuration, (b) equivalent circuit, (c) equivalent circuit by replacing the radial TL by a Π network.

6.1 INTRODUCTION

Flexible portable devices like mobile phones, laptops, etc. have changed our daily lives. The requirement of compact size and light weight is a huge challenge for these applications. Since traditional antennas have a size in the order of the operation wavelength, a lot of effort has been done to overcome this constraint [40-42] leading to the planar inverted-F antenna (PIFA), the meander transmission line antenna, and the loaded microstrip antenna. Recently，the CRLH TL has shown great potential in the design of variable patch antennas. The linear topology has been discussed in Chapter 5. In this chapter, the radial topology will be studied.

Various methods can be used to analyze a conventional circular patch antenna [39, 188, 189], including the generalized transmission line model, the cavity model, and the integral equation model. For patches loaded with a CRLH TL, a dedicated transmission line model is naturally the most suited. A conventional circular patch can be modeled as two sections of radial TL [190, 191]. These radial TLs can be replaced by a T or Π network, as seen in Fig. 6-1. Since the mutual admittances modeling the mutual coupling between the two radial TLs are small, they can be neglected in order to simplify the model.

Several circular patch antennas based on metamaterials have been designed. Some studies have been published that load the antenna with an epsilon negative (ENG) layer , and a ring antenna with circular polarization

has been realized by folding a rectangular CRLH TL patch antenna [192]. However, to the knowledge of the authors, the circular patch antenna loaded with a CRLH TL, corresponding to a double negative (DNG) structure, has never been studied before. In this chapter, the circuit model of the radial CRLH TL will be firstly formed. And then the full circular patch and sector patch antennas will be studied. Several prototypes are designed and measured.

6.2 CIRCUIT MODEL OF RADIAL CRLH TL

For the circular patch antenna loaded with a CRLH TL, each cell of the TL is modeled as a T network, so the model is similar to the equivalent circuit of the linear CRLH TL in Fig. 5-1 . Fig. 6-2 (a) depicts an example of a circular patch loaded with three CRLH TL cells. This is a typical mushroom type CRLH TL, where the slots between the rings provide the series capacitances and the metallic pins provide the shunt inductances. However, in contrast to the linear CRLH TL, the equivalent circuit of each cell in the circular CRLH TL is not the same. In order to obtain a quasi-homogeneous metamaterial topology, the density of the metallic pins has to be quasi-constant over the surface. In a radial structure, this means that the number of pins has to grow as the radius of the cell increases. If each cell has the same width

$$r_1 = \frac{r_2}{2} = \frac{r_3}{3} = \frac{r_4}{4} = \cdots \frac{r_u}{u} \tag{6.1}$$

where u is the total number of cells, the number of pins p_u in each cell should increase proportionally to the area of the cells

$$\frac{r_1^2}{p_1} = \frac{r_2^2 - r_1^2}{p_2} = \frac{r_3^2 - r_2^2}{p_3} = \frac{r_4^2 - r_3^2}{p_4} = \cdots = \frac{r_u^2 - r_{u-1}^2}{p_u} \tag{6.2}$$

Inserting (6.1) into (6.2) yields

$$p_1 = \frac{p_2}{3} = \frac{p_3}{5} = \frac{p_4}{7} = \cdots = \frac{p_u}{2u-1} \tag{6.3}$$

The pins are positioned in the geometric centers of the cells

$$r_{pu} = \sqrt{\frac{r_u^2 + r_{u-1}^2}{2}} \tag{6.4}$$

Under these conditions, and assuming that the ratio of the slot width to the ring width is small enough, the equivalent components of each cell can be related as follows

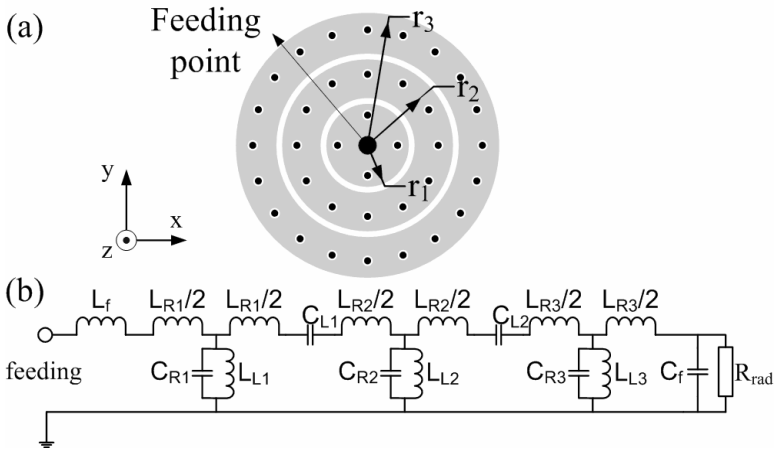

Fig. 6-2. Transmission line model of circular patch antenna based on CRLH TL. (a) configuration, (b) equivalent circuit.

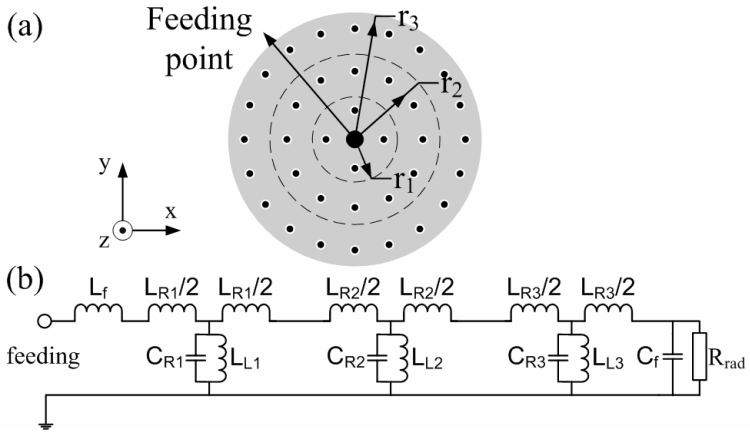

Fig. 6-3. Transmission line model of ENG MM based circular patch antenna. (a) configuration, (b) equivalent circuit.

$$C_{R1} = \frac{C_{R2}}{3} = \frac{C_{R3}}{5} = \frac{C_{R4}}{7} = \cdots = \frac{C_{Ru}}{2u-1} \tag{6.5}$$

$$L_{L1} = 3L_{L2} = 5L_{L3} = 7L_{L7} = \cdots = (2u-1)L_{Lu} \tag{6.6}$$

$$C_{L1} = \frac{C_{L2}}{2} = \frac{C_{L3}}{3} = \frac{C_{L4}}{4} = \cdots = \frac{C_{Lu}}{u} \tag{6.7}$$

$$L_{R1} = 3L_{R2} = 5L_{R3} = 7L_{R4} = \cdots (2u-1)L_{Ru} \tag{6.8}$$

C_R models the capacitive coupling between a metal ring and the ground. It is proportional to the area and, since their width is constant, thus to the length of the corresponding metal ring. C_L models the capacitive coupling between the metal rings, and is proportional to the length of the corresponding slot between them. L_L models the inductance of the pins and, since they are in parallel, is proportional to the inverse of the number of metal pins. L_R models the inductive effect linked to the radial currents flowing on the rings between the slots. Observed at the center radii of the rings, such a current is approximately proportional to the inverse of this center radius because the effective wavelength of the current flowing on the structure tends to infinity. The radiation resistor can be equally calculated based on the radiation produced by a magnetic current flowing in the circular slot at the edge of the patch. The width of this slot is taken the same as the thickness of the substrate. Note the series inductance L_f at the left due to the feeding probe and the capacitor C_f at the right due to the fringing fields at the edge of the patch. All the parameters can thus be calculated as lumped components [193].

As the open-ended ZOR mode is only related to the shunt components, the circular open circuit patch antenna only loaded with inductances (shunt pins) can also support this ZOR mode, as shown in. Since the inductor-loaded structure is linked to an epsilon negative characteristic [10] from a metamaterial point of view, further in this paper, we call this antenna the ENG MM based ZOR antenna. However, as shown in the next section, the ENG MM cannot support the other negative modes, as a CRLH TL does, which requires the effective permittivity and permeability to be simultaneously negative.

In this chapter, only TM_{0n0} modes, yielding a monopolar radiation pattern, are analyzed. Describing the field distribution under the circular patch with Bessel functions, the center of the circular patch corresponds to an open point (value $\neq 0$) if $m = 0$ (TM_{0n0}) and to a short point (value = 0) if $m \neq 0$ (TM_{mn0}). In the rest of the paper, all the patches are fed in their center to suppress the modes $m \neq 0$.

6.3 ZEROTH-ORDER RESONANT CIRCULAR PATCH ANTENNA BASED ON PERIODIC STRUCTURES

6.3.1 Basic Structure of ZOR Antenna

In this section, a three unit cell basic ZOR antenna is calculated to validate our circuit model. The substrate is chosen as Rogers RO3003 (ε_r = 3.0) with height 1.524 mm. The width of the unit cell rings is 20 mm, including the copper and gap, and the gaps between the rings are 0.3 mm. The number of pins in the inner ring (the first unit cell) is p_1 = 4 and the radius of the pins is 0.25 mm.

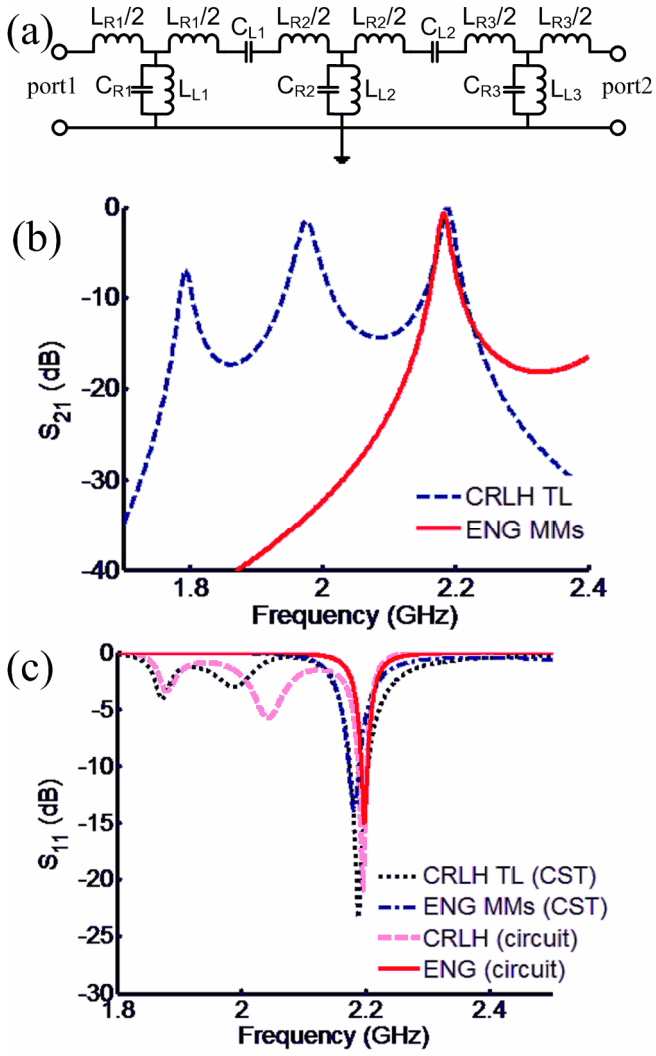

Fig. 6-4. (a) Transmission line model. (b) Transmission coefficient of the transmission line model. (c) Reflection coefficient of the circular patch antennas based on CRLH TL and ENG MM.

The basic structures studied first consist of three rings, with and without gaps, see Fig. 6-2 and Fig. 6-3, respectively. The equivalent circuits of these two antennas are also shown. As mentioned before, the circuit parameters can be calculated separately. The approximate values calculated with the empirical equations of [193] are as follows, L_{L1} = 134 pH, C_{R1} = 21.9 pF, C_{L1} = 5.3 pF and L_{R1} = 235 pH. The radiation resistance is 26 Ω at 2.2 GHz. The transmission results based on the TL model (considering a port 2 instead of a resistance R_{rad} at the right end, see Fig. 6-4 (a)) are shown in Fig. 6-4 (b), where the reference impedance is 50 Ω at both ports. It can be clearly seen that there are three obvious resonances for the structure based on the CRLH TL, representing the modes n = -2, n= -1 and n=0. However, for the structure based on ENG MM, only the mode n = 0 can be found. Fig. 6-4 (c) depicts the calculated results based on the circuit model and CST MWS, respectively, for the antennas. The full wave simulations show the same resonances as predicted by the circuit model. Only a little frequency shift is observable for the n = -1 mode, probably a consequence of the slight inaccuracy due to the empirical equations. The z-component of the electric field distributions is displayed in Fig. 6-5. The electric field distributions of the modes n = -1 and -2 are similar with n = 1 and 2 in conventional circular patch. At n = 0 mode, the electric field is nearly not changed under the patch, in both azimuthal direction and radial direction.

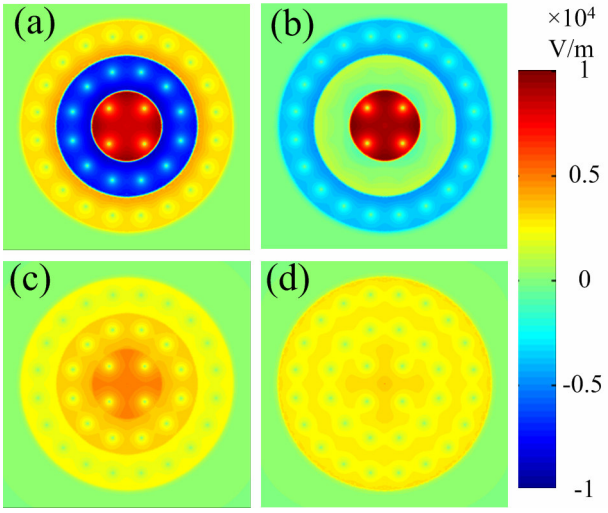

Fig. 6-5. Distributions of z component of electric field. (a) $TM_{0(-2)0}$ of CRLH TL antenna, (b) $TM_{0(-1)0}$ of CRLH TL antenna, (c) TM_{000} of CRLH TL antenna, (d) TM_{000} of ENG MM antenna

Comparing the circuit model for the equivalent radial CRLH TL used in this paper and a traditional linear CRLH TL, it can be clearly seen that they are considerably different. In the linear TL model, the circuit equivalent is based on a uniform unit cell, so ideal periodic boundary conditions can be adopted. The resonant frequency of the open boundary ZOR mode is totally depending on L_L and C_R. However, for a radial TL, although the effective permittivity and permeability of each unit cell is the same and thus the metamaterial is homogeneous, as can be clearly seen in formulas (6.5)-(6.8) the circuit parameters are changing from unit cell to unit cell. So a simple calculation of each unit cell is not enough to obtain the total performance of the antenna, but a complete analysis has to be performed with the circuit network (as in Fig. 6-2 and Fig. 6-3).

Here we mainly discuss the ZOR mode. Since the proposed antenna is open-ended, the resonant frequency is totally depending on the shunt components (C_R and L_L). Obviously, as the number of cells increases, the product of the values of these shunt components stays constant, i.e. ($C_{Ru}L_{Lu}$ = $(2u\text{-}1)C_{R1}\ L_{L1}/(2u\text{-}1) = C_{R1}L_{L1}$. The result is that the resonant frequency of the ZOR mode will not change significantly. In each cell, C_R is controlled by the area of the corresponding ring, and L_L is related to the number and diameter of the vias. In this way the ZOR mode can be easily controlled, e.g. increasing the width of the cells or reducing the radius of the vias will shift the resonant frequency to lower values. Since other modes relate to the number of cells or the radius of the patch, controlling their resonant frequencies is much more complex.

As we mentioned before, the number of unit cells will not affect the resonant frequency of the ZOR mode. However, enlarging the aperture may improve the directivity of the antenna. In the next two sections, two antennas working under ZOR mode conditions will be designed based on a different number of unit cells. One is using a single unit cell to obtain a compact size. The other is based on four unit cells and reaches a much higher directivity. The physical parameters, e.g., the patch radius, the number of pins, and the numbers of unit cells remain the same unless specified otherwise.

6.3.2 **Miniaturized ZOR Antenna**

Since the resonant frequency of the ZOR TM_{000} mode is totally determined by the shunt components, a large value of L_L and C_R yields a low resonant frequency. In mushroom structures, C_R is provided by sections of the patch and ground plane, so its value is completely determined by the patch size. This is not helpful for miniaturizing the antenna. L_L is provided by the pins

under the patch. Obviously a small pin cannot give a large inductance [189, 194]. In several papers about rectangular ZOR patch antennas [195, 196], slots are introduced in the ground to enlarge the shunt inductance. Here the same idea is used for the circular patch antenna.

Since the pins related to the left-handed inductances are in parallel with each other, their number should be chosen as small as possible in order to lower the resonant frequency. Here four pins are used in the design. Only one unit cell ring is used and the patch radius is fixed to 10 mm, as shown in Fig. 6-6. A spiral slot with width 0.2 mm is put under each pin. The center of each spiral is coincident with its pin, and the spiral polar equation is $r = 0.1\theta$ *for* $5\pi<\theta<\theta_m$, with variable θ_m in order to get different spiral slot lengths. The feeding pin is added in the center of the patch directly. Table 6-I displays the results of the simulations with CST. While prolonging the length of the slot from 0 to 1.5 turns, the resonant frequency falls from 4.412 GHz to 2.179 GHz, which is caused by the increase of L_L. However, the radiation efficiency falls enormously from -0.56 dB to -10.08 dB. So, as could be expected, the price to pay for a small size is very low radiation efficiency.

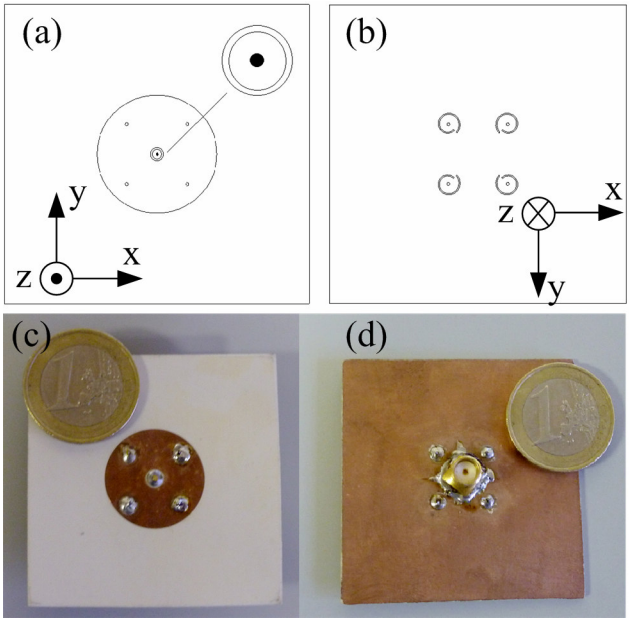

Fig. 6-6. Configuration of miniaturized ZOR antenna. (a) top view, (b) bottom view, (c) and (d) photo. In (a) a zoomed in feeding region is shown.

TABLE 6-I
CHANGING THE LENGTH OF THE SPIRAL SLOT.

Length of spiral slot (turns)	f_0 **(GHz)**	$Z_{in}=R_{in}+jX_{in}$ **(Ω)**	**Rad. eff. (dB)**	**Directivity (dB)**
0	4.412	347+j115	-0.56	2.68
0.5	4.233	408+j102	-0.81	2.67
0.75	3.942	469+j93.1	-1.28	2.26
1	3.413	644+j57.1	-2.80	1.29
1.25	2.683	984+j17.4	-6.69	1.02
1.5	2.179	1140-j10.1	-10.08	1.19

Another problem is that for long spiral slots the input resistance becomes very high, hindering impedance matching. A simple solution is to put a slot around the feeding point. The capacitive coupling over the slot can reduce the input resistance of the antenna. The radius of this slot can be optimized to get the smallest possible return loss. As an example, a circular patch with this type of feeding is shown in In order to keep the radiation efficiency acceptable, the length of the spiral slots in the ground is chosen one turn long. The inner radius of the feeding slot is 1.1 mm and its width is 0.3 mm. Fig. 6-7 (a) compares the return losses of the directly fed antenna and the slot fed antenna. With the introduction of the feeding slot, the working frequency decreases slightly, and S_{11} is reduced to -24 dB and -15 dB in the simulation and measurement, respectively. Fig. 6-7 (b) shows that this antenna has a monopolar pattern with no power radiated in the forward direction. This is different compared to the conventional patch antenna working in the TM_{010} mode. The measured results agree well with the simulated ones. The only difference is in the back radiation, which is caused by the presence of the feeding coaxial cable.

We wish to emphasize that an additional numerical study showed that the performance of the antenna is not strongly related with the size of the ground. A considerable frequency shift appears only when the ground is too small, which may be caused by the fringing effect at the edges of the ground. Even when the ground is reduced to 25mm x 25mm, the resonance centered at 3.39 GHz still has a bandwidth of 14 MHz. Note that a small ground allows to keep the design compact.

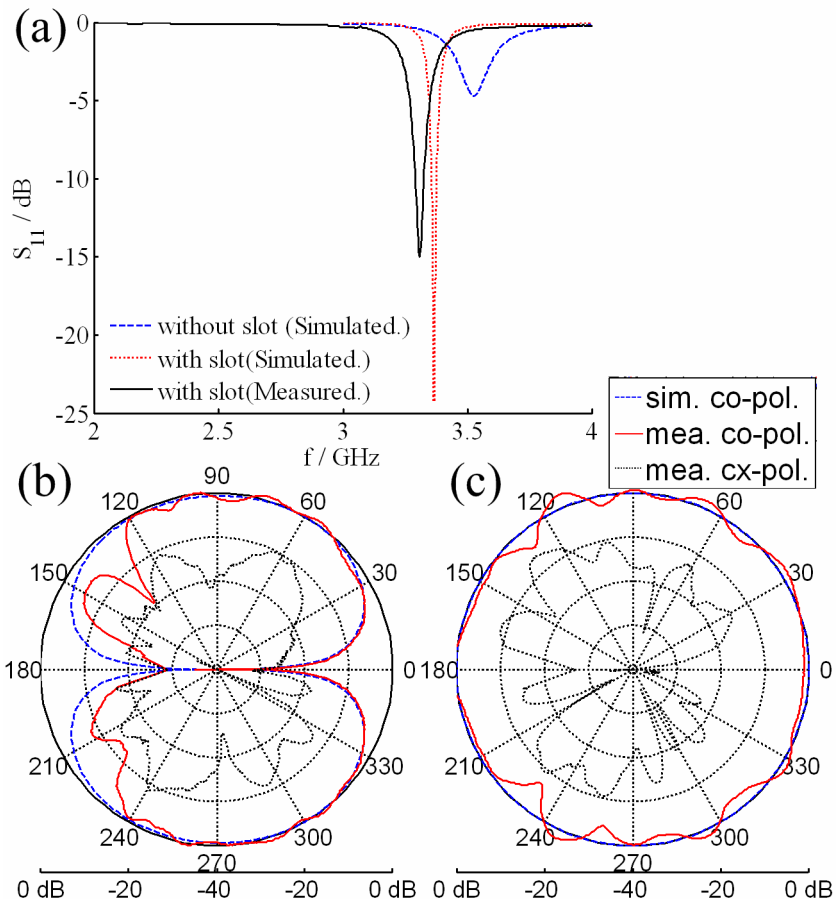

Fig. 6-7. Simulation results of antenna in Fig. 7. (a) return loss, (b) radiation pattern in x-y plane, (c) radiation pattern in x-z plane. The simulated cross polar component is negligible. The measured one is mainly due to the feeding structure, since the ground plane is only ca. 0.55 λ_0 × 0.55 λ_0.

TABLE 6-II
COMPARISON OF CONVENTIONAL PATCH AND ENG MM PATCH ANTENNA IN FIG. 6-6.

	r (mm)	d/λ_0		f_0 (GHz)	BW (MHz)	$\eta_{rad.}$ (dB)	$\eta_{tot.}$ (dB)	Dir. (dB)	$G_{real.}$ (dB)
Conventional (TM_{010})	30	0.68	Sim.	3.403	46	-0.41	-0.42	4.57	4.15
ENG MM patch (TM_{000})	10	0.22	Sim.	3.366	20	-3.07	-3.14	1.24	-1.90
			Mea.	3.309	34	/	-2.68	1.58	-1.1

Table 6-II compares this miniaturized ZOR patch antenna with a conventional circular patch antenna operating at 3.35 GHz (TM_{010} mode with monopolar radiation pattern). The radius of the patch falls from 30 mm to 10 mm in our design, which yields a reduction in used area of 89 %. Even compared to the circular patch antenna loaded with metamaterial [197, 198], this design shows a significant reduction in size. The price to pay is the drop in radiation efficiency (from -0.42 dB to -3.14 dB in the simulation), and the narrower bandwidth. The measured directivity is calculated from the half power beamwidth [39], and the total efficiency is measured by the Wheeler cap method [199]. The measured results show a slightly higher bandwidth, efficiency, and gain compared with the simulated results. This may be caused by the parasitic capacitance induced by sealing the SMA connector. The extra capacitance partially neutralizes the inductance of the antenna itself.

In [198], a CRLH ZOR antenna is proposed, which comprises a circular patch coupled to a circular ring mushroom structure. This can be recognized as a patch partly loaded with metamaterial. Although this antenna also can be considered as a low-profile monopole when operating at the ZOR mode, and featuring a size reduction when operating at the -1st mode, the circuit model developed there is only usable to design this very specific topology. Our circuit model, developed for the circular patch antenna fully loaded with metamaterial, is usable for different numbers of rings (or unit cells) and different "component" densities within a unit cell. This section IV shows the antenna with only one unit cell, which has an even smaller size than the antenna in [198]. In section V, another design with four unit cells, yielding a high gain, will be introduced.

6.3.3 **High Directivity ZOR Antenna**

As mentioned previously, by increasing the number of unit cells, the directivity is enhanced [200] for both the CRLH TL based antenna and the ENG MM based antenna.

In Fig. 6-8 an antenna based on the CRLH TL structure is presented, containing four unit cells of identical width 10 mm. With four unit cells, the input resistance is not very high and the input reactance almost equals the resistance. The use of slot feeding like in the previous section can induce a large capacitance and thus counteract the input reactance, while simultaneously reducing the input resistance. Here, a split ring slot type of feeding is used, as shown in Fig. 6-8. The slot can cancel the input reactance,

while the small "gap" in the slot does not considerably affect the input resistance.

After optimizing the radius of the slot in order to obtain the lowest reflection, the inner radius of the slot is 4.5 mm, the width of the slot is 0.3 mm, and the width of the split is 0.5 mm. Fig. 6-9 (a) shows the return loss of the antenna in Fig. 6-8. It can be seen that the return loss of the antenna fed with the split slot topology decreases significantly compared with the original design. However, the measured result shows a noticeable frequency shift in the lower frequency range. After carefully examining the sample, it was found that the reason is that the metallic wires used as vias are narrower than the diameters of the holes on the PCB, due to the fact that the soldering tin cannot fill the gaps between the wires and holes completely. The diameter of the vias directly determines the shunt left-handed inductance (L_L), and also the resonant frequency of the ZOR mode, see Fig. 6-2 and Fig. 6-3. Using the real diameter of the wires in the simulation, i.e. 0.35 mm, the results agree much better, as shown in Fig. 6-9 (b).

Fig. 6-9 (c) and (d) yield the radiation patterns of the antenna. Since a finite ground plane is used, the maximum angle is not accurate at 90° in the x-z plane. But the zeros are still located at $\theta = 0°$ and 180°, as expected for a monopolar radiation pattern. Table 6-III gives a comparison between the conventional circular patch (TM_{010}) and the patch loaded with the periodic structures (TM_{000}). The radius of the loaded patch is 40 mm, yielding operation at 4.62 GHz. The conventional patch operating at the same frequency has a radius of 22.2 mm. Since the active aperture is increased in our design, the directivity increases from 5.31 dB to 7.42 dB (simulation) and 7.9 dB (measurement). Although the radiation efficiencies fall down a little, the improvement of the realized gain is still about 1.8 dB.

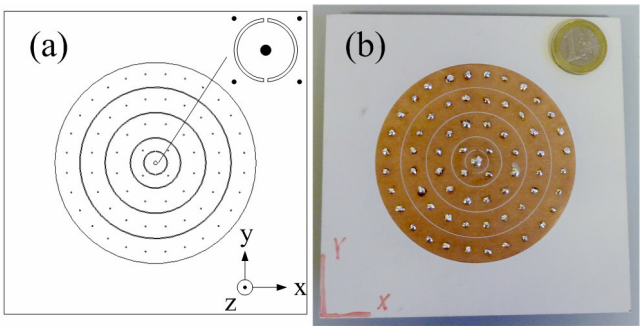

Fig. 6-8. Configuration of high directivity ZOR antenna, (a) top view, (b) photo. In (a) the zoomed in feeding region is shown.

The ENG MM based antenna can also be used to provide a high directivity for the TM_{000} mode. However, it will not show the negative modes, see Fig. 6-4.

In [63] at first sight a similar configuration is used. The goal there is to increase the gain of a simple patch antenna and a so-called cylindrical electromagnetic crystal substrate is positioned at the perimeter of the patch in the center. The electromagnetic band gap structure obtained reduces the surface wave, in this way improving the gain. The radiation pattern of that antenna is similar to the one of the traditional patch antenna. It has to be emphasized that the working principle of our design is totally different. It uses the whole periodic topology as radiating structure, and the resonant mode is totally different. The increase of the gain is caused by the increase of the antenna area, and the radiation pattern resembles the one of a monopole antenna.

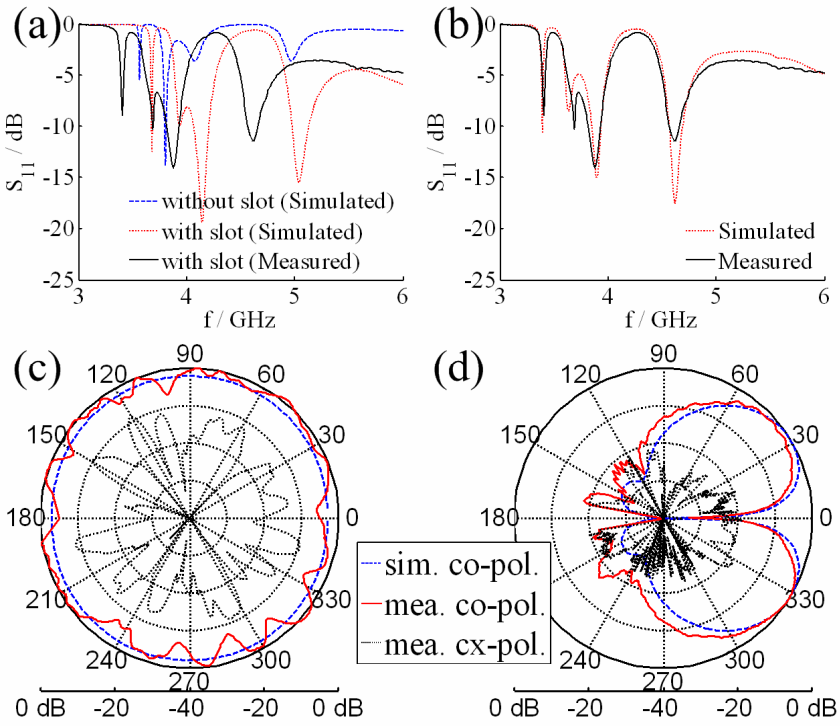

Fig. 6-9. Simulation and measurement results of antenna loaded with four CRLH TL unit cells. (a) return loss (diameter of metallic wires is 0.5 mm in simulation), (b) return loss (diameter of metallic wires is 0.35 mm in simulation), (c) radiation pattern in x-y plane, (d) radiation pattern in x-z plane.

TABLE 6-III
COMPARISON OF CONVENTIONAL PATCH AND PATCH WITH PERIODIC STRUCTURE IN FIG. 6-8.

	r (mm)	d/λ_0		f_0 (GHz)	BW (MHz)	$\eta_{rad.}$ (dB)	$\eta_{tot.}$ (dB)	Dir. (dB)	$G_{real.}$ (dB)
Conventional (TM_{010})	22.2	0.68	Sim.	4.62	100	-0.24	-0.26	5.31	5.05
CRLH TL patch (TM_{000})	40	1.23	Sim.	4.62	126	-0.53	-0.64	7.42	6.77
			Mea.	4.62	57	/	-1.1	7.9	6.8

6.4 META-LOADED CIRCULAR SECTOR PATCH ANTENNA

A circular sector patch antenna loaded with a periodic metamaterial topology is presented. Several shapes of the circular sector patch are analyzed and the input impedances and radiation patterns are compared. The topology reveals a nearly constant resonant frequency at zeroth-order resonance (ZOR) while the radiation performance approaches the one of the ZOR full circular patch antenna. Compared with rectangular and circular patch antennas, the sector patch offers more tuning possibilities. A matching network can be easily introduced to enhance the impedance bandwidth. Apart from the ZOR characteristics, this topology can also support a quasi-monopolar pattern at multiple modes. A semicircular patch operating at 4.1 GHz together with an impedance matching network and a dual-band semicircular patch antenna are fabricated and measured.

6.4.1 Circular Patch Antenna

A typical mushroom CRLH-TL circular patch antenna topology shown in Fig. 6-10 (a) has been discussed in section 6.3. The CRLH-TL can be recognized as a double negative metamaterial, which can form negative modes. An alternative, the inductor loaded structure (without slots between the unit cells) is displayed in Fig. 6-10 (b), which is in essence a kind of epsilon negative metamaterial and can only support ZOR mode and the positive modes. Both the CRLH-TL and inductor loaded structure can be analyzed based on the concept of a radial transmission line topology. A circuit model already has been proposed in section 6.2.

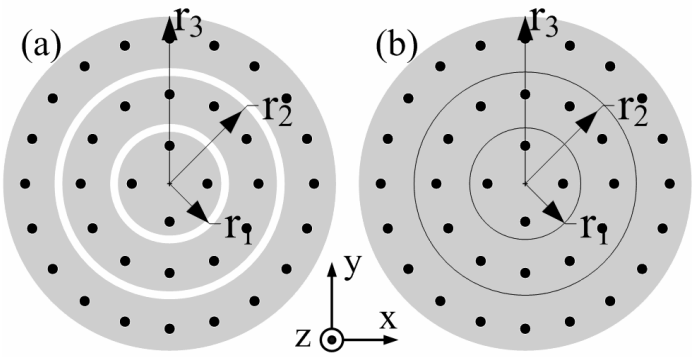

Fig. 6-10. Topology of circular patch antenna with meta-loading. (a) CRLH-TL loaded structure, (b) Inductor loaded structure.

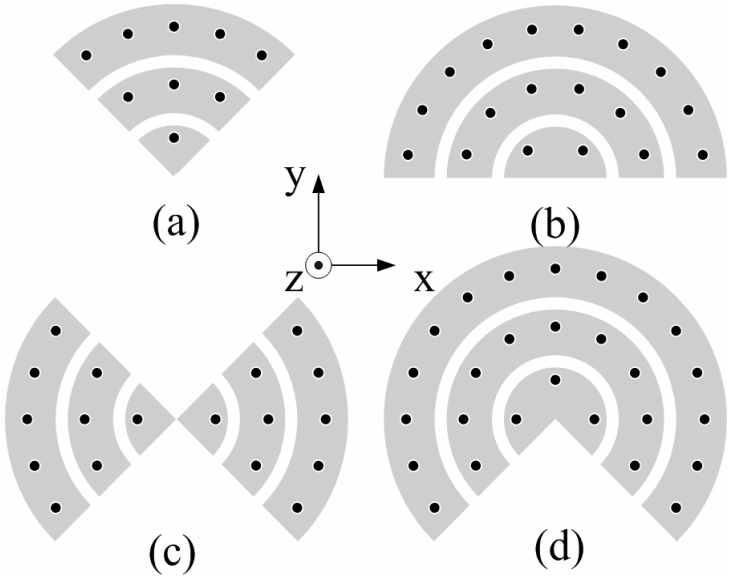

Fig. 6-11. Several circular sector patch antenna types. (a) a quarter sector (90°), (b) semicircular sector (180°), (c) double quarter sector (each sector is 90°), (d) three quarter sector (270°).

6.4.2 **Circular Sector Patch Antenna**

For a circular patch antenna operating in ZOR mode, the electric field under the patch is nearly constant in both the azimuthal and the radial direction. It is reasonable to assume that just a sector of the circular patch can also support the same ZOR mode as the circular patch.

TABLE 6-IV
CHANGING THE WIDTH OF THE UNIT CELL

	Shape	f_0 (GHz)	$Z_{in}=R_{in}+jX_{in}$ (Ω)	Rad. eff. (dB)	Dir. (dB)
CRLH-TL	Fig. 6-11 (a)	4.135	104.4+j51.3	-0.51	7.1
	Fig. 6-11 (b)	4.262	74.1+j82.4	-0.44	7.2
	Fig. 6-11 (c)	4.115	98.2+j79.8	-0.84	7.1
	Fig. 6-11 (d)	4.34	66.4+j93.1	-0.54	6.6
	Fig. 6-10 (a)	4.495	46.8+j102.3	-0.44	5.4
Inductor loaded structures*	Fig. 6-11 (a)	4.085	268.7+j160.9	-0.50	6.67
	Fig. 6-11 (b)	4.232	89.2+j122.6	-0.44	7.03
	Fig. 6-11 (c)	4.13	170.2+j119.2	-0.84	7.2
	Fig. 6-11 (d)	4.3	56.2+j115.1	-0.55	6.6
	Fig. 6-10 (b)	4.435	22.9+j115.2	-0.52	5.6

*The shapes of the circular sector patches loaded with the inductor loaded structures are almost the same as in Fig. 6-11, but without slots, as depicted in Fig. 6-10 (b).

In the following, we will analyze the circular sector patch antennas shown in Fig. 6-11. The substrate used is Rogers RO 4003 (ε_r = 3.55, tan δ = 0.0027) with thickness 1.524 mm, and the width of each unit cell is 10 mm ($r_1 = r_2/2 = r_3/3$). The width of the gap between the copper rings is 0.3 mm, and the number of the pins in the unit cells is given in Fig. 6-11. The diameter of the pins is 0.5 mm. The antennas are fed by a probe in the center of the circle. In all structures, the size of the substrate and the ground is 120 × 120 mm^2, and the center points of all the sectors are located in the center of the substrate. The minimum distance from the patch to the edge of the substrate is 30 mm, which is larger than a half wavelength at the operating frequency.

CST MWS was used to perform a numerical analysis of all sector patch antennas in Fig. 6-11, working in the ZOR mode. TABLE 6-IV compares the resonant frequencies, input impedances, radiation efficiencies, and directivities.

First of all, it is important to note that, although there is a large variation in antenna size, all resonant frequencies are nearly the same. The maximum difference is about 10 %, both for the CRLH and inductor loaded antennas. This characteristic of the ZOR antenna gives engineers quite some freedom to choose the shape of the antenna in a dedicated way for a specific compact system. The efficiency of the antennas remains at a high level even with

decreasing size. The directivities are higher than the one for the full circle. This is due to the fact that the radiation patterns become asymmetric, which is caused by the loss of the circular symmetry of the patch itself. The highest directivities are found for the (b) and (c) structures. The only parameter changing a lot is the input impedance. This means that special feeding methods, including an impedance matching, are needed.

It was also clearly observed that the effect of other physical parameters (e.g. the number of unit cells, the width of the unit cells, the number of pins, etc.) on the antenna characteristics is similar as in case of the whole circular patch antenna. We refer to the previous sections 6.2 and 6.3 for a discussion on this.

6.4.3 **Semicircular Patch with Matching Network**

Since the impedances of the antennas in Fig. 6-11 are very different and far from 50 Ω, an impedance matching network has to be used in order to feed power efficiently. In sections 6.2, coaxial cable feeding from the back of the antenna is used, with a slot near the feeding point for impedance matching. In this section a microstrip feeding line is used. It can provide more bandwidth than the coaxial feeding.

Fig. 6-12 (a) shows the details of the feeding network used. An interdigital capacitor and an additional transmission line provide the matching. For different circular sectors, different values for the capacitor have to be used. This can be reached by changing the number, width, spacing and length of the fingers, and the width and length of the transmission line. A genetic algorithm is used to optimize this matching network in order to obtain the smallest possible return loss. A semicircular sector patch is used to illustrate the topology. The optimium dimensions are discribed in Fig. 6-12 (a) and TABLE 6-V. A prototype was fabricated and is shown in Fig. 6-12 (b).

The simulated and measured reflection coefficients are displayed in Fig. 6-12 (c). The order of a mode can be uniquely determined based on the field distribution. A significant ZOR resonance can be observed. However, the measured result (4.109 GHz) shows a noticeable shift to lower frequencies compared to the original simulations. The reason is that the metallic wires used as vias are narrower than the diameters of the holes in the PCB, and that the soldering tin cannot fill the gaps between wires and holes completely. Using the real diameter of the wires in the simulation, i.e. 0.45 mm, the result agrees much better, as shown in Fig. 6-12 (c). Meanwhile, a small resonance can also be observed around 3.462 GHz, which corresponds to the n = -1 mode. The n = -2 mode can hardly be seen due to mismatching.

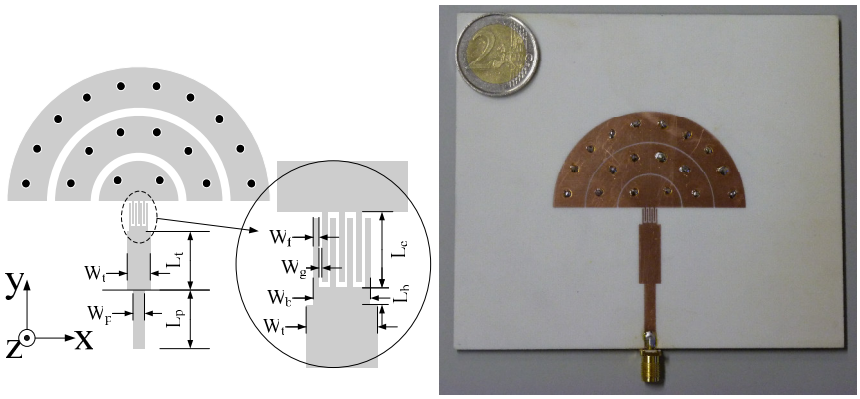

(a) (b)

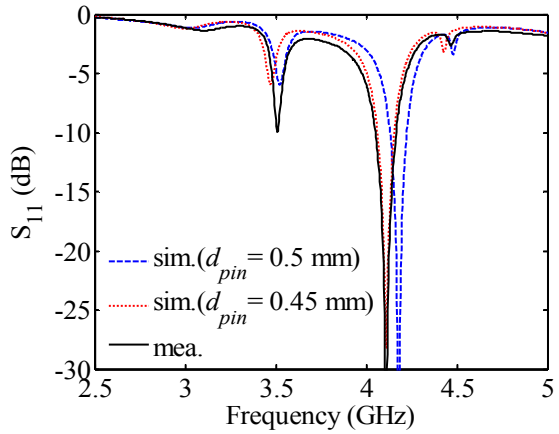

(c)

Fig. 6-12 Semicircular sector patch antenna with matching network. (a) topology, (b) fabricated prototype, (c) reflection coefficient.

TABLE 6-V
THE PARAMETERS OF THE FEEDING NETWORK (UNIT: MM)

W_p	L_p	W_t	L_t	W_f	W_g	L_c	W_b	L_b
3.45	20	6.8	18	0.4	0.3	4.5	4.6	0.5

The simulated z component of the electric field (E_z) is shown for the n = -1 and the ZOR mode in Fig. 6-13. For the n = -1 mode (3.462 GHz), E_z has a standing wave behavior in the radial direction from the center of the patch to the edge. For the n = 0 mode (4.110 GHz), the field distribution is totally different. The electric field is nearly constant under the patch, in both azimuthal and radial direction, which is characteristic for the ZOR mode.

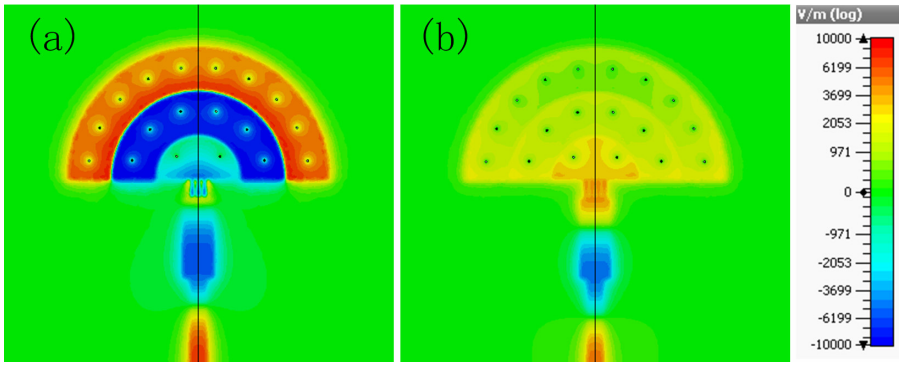

Fig. 6-13 Distribution of z component of the electric field. (a) 3.462 GHz, (b) 4.110 GHz.

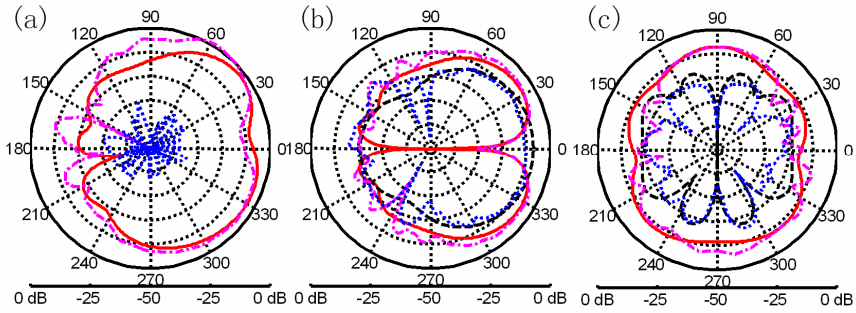

Fig. 6-14 Radiation patterns of the semicircular patch antenna at 4.11 GHz. (a) y-z plane (θ = 90°), (b) x-z plane (φ = 0°), (c) x-y plane (φ = 90°). The coordinate system is defined as in Fig. 6-12 (a). (solid (red) line: simulated θ component, dashdot (magenta) line: measured θ component, dashed (black) line: simulated φ component, dotted (blue) line: measured φ component.)

The radiation pattern of the ZOR mode is shown in Fig. 6-14. The measured results agree well with the simulated ones. The only difference is the back radiation, which is caused by the presence of the feeding coaxial cable in the measurement set-up. The semicircular sector patch also shows a quasi-monopolar pattern in the x-y plane. The omnidirctionality is not as good as for the circular patch. On the z-axis, the θ component of the electric field is zero, as in the case of a monopole. The maximum radiation level is observed at about θ = 40° and φ = 90°. Several other important parameters of the antenna are given in

TABLE 6-VI. The cross polarization in the y-z plane is mainly due to the feeding lines.

TABLE 6-VI
SIMULATED AND MEASURED RESULTS

	Freq. (GHz)	S_{11} (dB)	BW (MHz)	Dir. (dB)	$G_{real.}$ (dB)	η_{tot} (%)
Simulated	4.110	-28	91	6.34	5.65	85
Measured	4.109	-57	114	/	5.82	82

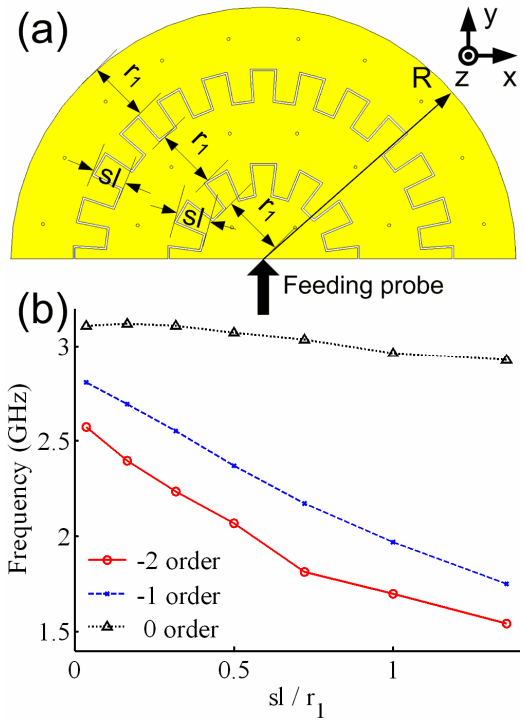

Fig. 6-15 (a) Model of the multi-band semicircular patch, (b) the resonant frequencies.

6.4.4 **Dual-band Semicircular Patch Antenna**

It has been shown in Fig. 6-12 that the CRLH-TL antenna can support a dual-band behavior. However, two issues need to be studied: one is the tuning of the frequency ratio; the other is the impedance matching. Here, interdigital capacitors are introduced to replace the series slot capacitors, see Fig. 6-15 (a). By changing the number, length and width of the fingers, the left-handed capacitor (C_L) can be easily adjusted to control the tuning of the

frequency ratio. Fig. 6-15 (b) shows the resonant frequency for different lengths of the capacitor fingers. The radius of the whole patch (R) is fixed at 40 mm. As the ratio of Sl and r_1 is increasing, the resonant frequency of the ZOR mode only slightly decreases, since it is not related to the left-handed capacitors (C_L). However, the resonant frequencies of the other two (negative) modes are decreasing, as C_L becomes larger. By tuning the shape of the patch (sl/r_1), the frequency ratio of the modes can be easily adjusted.

After obtaining the required frequency ratio, the double stub tuning method can be used to form a matching network. An example is displayed in Fig. 6-16 (a) and (b), in which r_1 and sl is 10 mm and 5 mm, respectively. The dimensions of the double stub matching network are optimized to obtain the minimum return loss at the n = -1 mode and the ZOR mode. The measured results are in Fig. 6-16 (c). A high qualitative agreement is observed. The slight frequency shifts are easily explained by the tolerances on the material parameters and the fabrication dimensions.

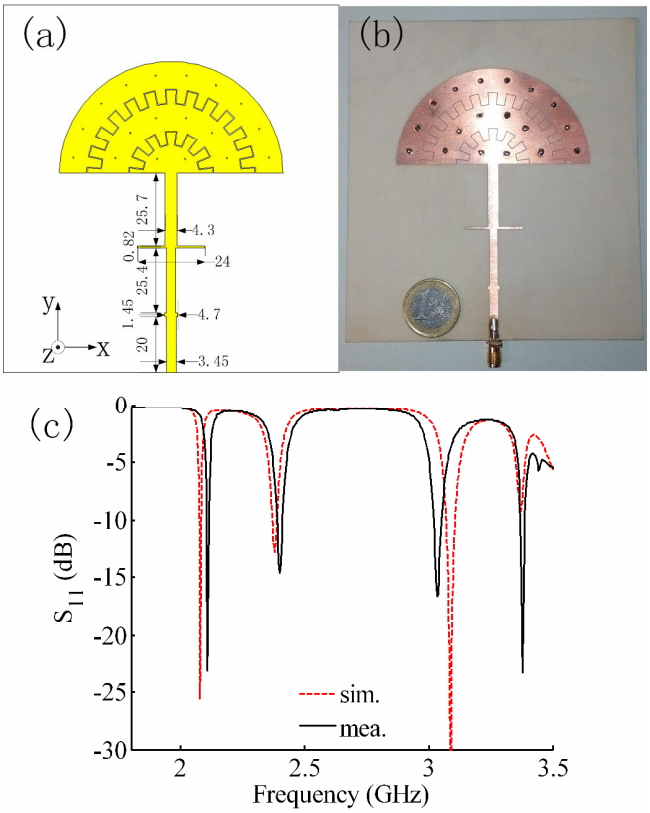

Fig. 6-16 Dual-band semicircular patch antenna with matching network. (a) topology, (b) fabricated prototype, (c) measured and simulated S_{11}.

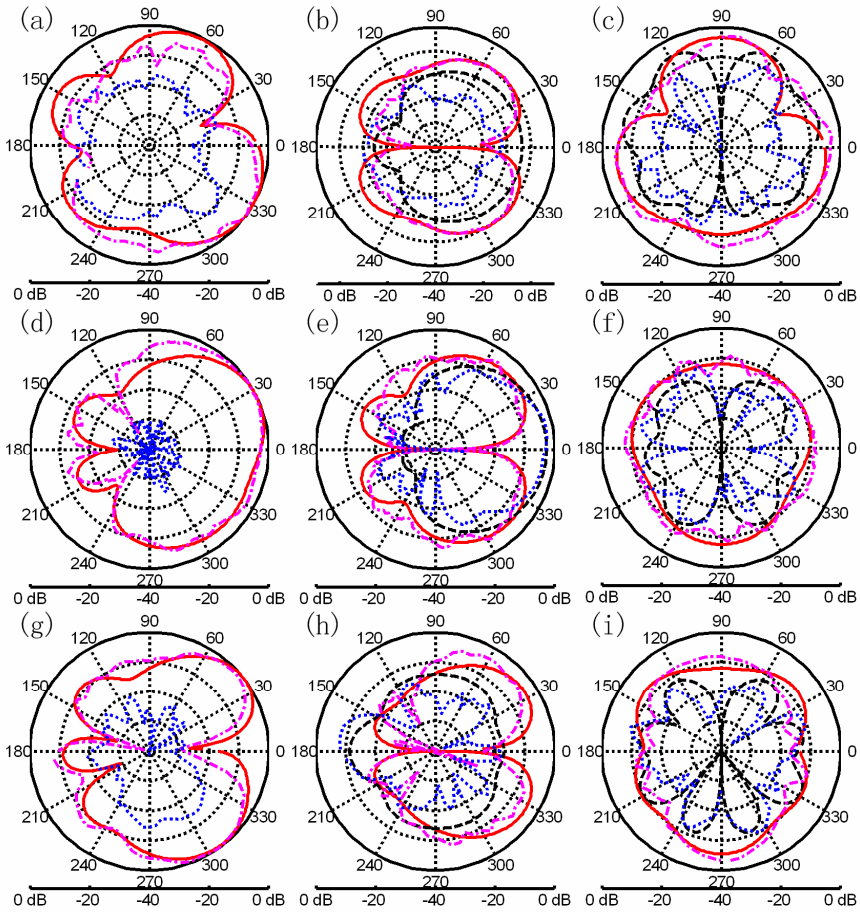

Fig. 6-17. Radiation patterns of the semicircular patch antenna. (a) y-z,(b) x-z, (c) x-y plane at 2.08 GHz, (d) y-z,(e) x-z, (f) x-y plane at 2.38 GHz, (g) y-z,(h) x-z, (i) x-y plane at 3.03 GHz. The coordinate system is defined as in Fig. 6-16 (a). (solid (red) line: simulated θ component, dashdot (magenta) line: measured θ component, dashed (black) line: simulated φ component, dotted (blue) line: measured φ component.)

The pattern of the antenna is measured in an anechoic chamber and is shown in Fig. 6-17. Note that the antenna displays a monopolar pattern at each resonant frequency. This is very attractive in many communication systems. The performance of the antenna is given in TABLE 6-VII. Since the efficiency at n = -2 mode is very low, the antenna is proposed to operate at n = -1 mode and ZOR mode. The n = +1 mode is also matched at 3.37 GHz. It is possible to tune this mode to a desired frequency, but this is not considered in this design.

TABLE 6-VII
SIMULATED AND MEASURED RESULTS

		Freq. (GHz)	S_{11} (dB)	BW (MHz)	Dir. (dB)	$G_{real.}$ (dB)	η_{tot} (%)
***n* = -2**	**Sim.**	2.080	-25.6	8	6.1	-1.5	22
	Mea.	2.105	-23.0	10	/	-1.8	27
***n* = -1**	**Sim.**	2.380	-12.9	17	6.5	4.9	67
	Mea.	2.394	-14.7	21	/	5.1	64
***n* = 0**	**Sim.**	3.088	-43.5	35	6.6	5.2	74
	Mea.	3.033	-16.7	32	/	5.8	75

6.5 CONCLUSION

In this chapter，the radial CRLH TL structure is studied. We first formed the circuit model of this kind of periodic structure, and then proposed several types of antenna based on it.

Since the resonant frequency of a ZOR mode is independent of the total physical size of the loaded patch, the antenna can be designed at arbitrary frequency with arbitrary size. A compact circular patch antenna with only 11 % of the size of the conventional patch antenna is designed. The cost of the miniaturization is a low radiation efficiency. A relatively large circular patch is also designed yielding a high directivity. A 70 % growth of the antenna radius gives a 2 dB increase of the directivity.

The sector patches can also support the ZOR mode. The reduction of the aperture will not bring a significant decline of the radiation performance, but the topology can be fed by an impedance matching network easily, which yields a wider bandwidth than for the circular patch. Besides, the multi-band sector patch antenna is also designed based on the ZOR mode and negative mode. The feature of this multi-band antenna is that it shows a quasi-monopolar pattern at all working frequencies.

Chapter 7

LOW PROFILE DUAL-BAND ANTENNA BASED ON ARTIFICIAL MAGNETIC CONDUCTOR PLANE

The low profile antenna based on an artificial magnetic conductor (AMC) plane will be studied in this chapter. Its dual-band operation is enabled by a rectangular patch in the 2.4 GHz band and a patch-etched slot dipole in the higher band. Since the AMC approaches a perfect magnetic conductor (PMC) in the higher band, the slot dipole can be located close to the ground. This enables a low profile structure, while simultaneously maintaining a large bandwidth and a high front-to-back ratio (FBR). Two antennas are designed for different applications, i.e. a wearable antenna and an antenna for a fall detection radar system.

This chapter is based on the following two publications:

[1] S. Yan, P. Soh, and G. A. E. Vandenbosch. "Low-profile dual-band textile antenna with artificial magnetic conductor plane", IEEE Transactions on Antennas and Propagation, 62. 12 (2014): 6487-6490.

[2] S. Yan, P. Soh, M. Mercuri, D. Schreurs, and G. A. E. Vandenbosch. "A low profile dual-band antenna loaded with artificial magnetic conductor for indoor radar systems", IET Radar, Sonar & Navigation, 2015 DOI: 10.1049/iet-rsn.2014.0202.

[3] P.J. Soh, S. Yan and G.A.E. Vandenbosch. "SAR MITIGATION OF TEXTILE ANTENNA VIA AN ARTIFICIAL MAGNETIC CONDUCTOR (AMC) PLANE", URSI Atlantic Radio Science Conference 2015 (AT-RASC 2015), Gran Ganaria, Canary Islands, May 2015, accepted.

7.1 INTRODUCTION

In Chapter 5 and Chapter 6, we discussed the patch antenna loaded with a CRLH TL. This kind of antennas can be designed with various planar shapes and sizes, and also operating in dual- or multi-bands. However, the bandwidth of a patch antenna is inherently narrow. A conventional microstrip patch antenna typically produces 3 to 5% of bandwidth. That is far away from the requirements in some applications, e.g. the 5 GHz band for WLAN applications and radar systems.

A dipole/monopole antenna can easily achieve a much wider bandwidth compared to the conventional simple patch antenna，but the omnidirectional pattern should be amended for some applications where a broadside radiation pattern is required. A planar metallic plane is usually used as the reflector for the dipole/monopole antenna. However, a certain distance should be kept between the dipole/monopole and the metal reflector [39, 201]. If the electric dipole/monopole is placed too close to the reflector, the anti-phase property of the mirrored current image will significantly reduce the radiation resistance. This will result in a significant mismatch and extremely low radiation efficiency. Conversely, a magnetic dipole/monopole antenna or slot dipole can be placed close to a perfect electric plane (PEC) without radiation impedance reduction. However, a parallel plate mode can be excited in between the antenna layer and the PEC plane. This mode will cause energy leakage and radiation pattern distortion, besides limiting antenna bandwidth.

An artificial magnetic conductor (AMC) plane is a kind of two-dimensional metasurface. It has been widely used already in the design of planar antennas [21, 22]. Since the PMC/AMC forms an in-phase mirror current for the dipole/monopole antenna, the radiation resistance will nearly be doubled compared to the situation in free space, and the antenna can maintain a high efficiency across a wide frequency band [22, 23, 56, 57, 62, 202, 203]. For the magnetic (slot) dipole antenna, the AMC plane functions as an electromagnetic band gap (EBG) structure which makes it possible to suppress any parallel plate modes and in this way avoid leaky radiation [64].

Several popular AMC structures, including mushroom topologies, square patch arrays, Jerusalem crosses, etc., have been demonstrated in literature via the design of several low profile AMC-based antennas for wideband or dual-band operation [64]. In order to generate dual-band AMC structures, different resonators are usually introduced [24, 60, 158], or the higher modes

of more complex resonators are used [58, 203]. Both methods result in a reduction of the AMC bandwidth and also perplex the design diaphragm and fabrication processes.

In this chapter, a new type of dual-band antenna based on the AMC structure is proposed. A slot dipole antenna is etched on a microstrip patch antenna. The AMC works as a PEC ground plane in the lower band for the microstrip patch antenna. In the upper band, the AMC approaches a perfect magnetic conductor (PMC), allowing an efficiently-radiating magnetic dipole without exciting the parallel plate mode in between the antenna plane and the ground plane [64]. To our best knowledge, this is the first antenna to utilize such concept. Compared with other designs, the proposed antenna is advantageous in two aspects. Firstly, the AMC layer is very simple. Since only a single resonance is required, the unit cell can be designed either using square or rectangular patches. This simplifies the fabrication using textile materials and the manual fabrication procedure. Secondly, the wide bandwidth in the upper band enables the AMC to easily cover the very wide upper band for some applications, e.g. the whole WLAN 5 GHz band or the wide band necessary in some radar systems. Although the patch topology limits the bandwidth at the lower frequency, the antenna still meets the requirements for normal WLAN communication in the 2.4 GHz band.

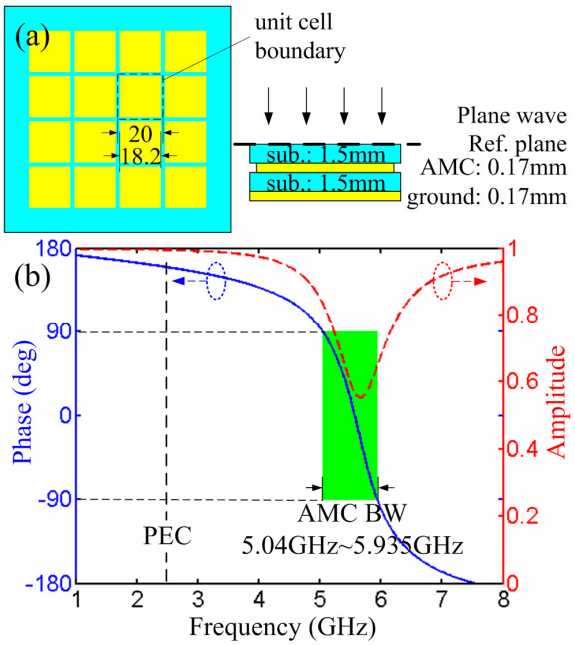

Fig. 7-1 Topology (a) and reflection coefficient (b) of the AMC plane.

7.2 LOW-PROFILE DUAL-BAND TEXTILE ANTENNA WITH ARTIFICIAL MAGNETIC CONDUCTOR PLANE

A dual-band textile antenna loaded with an artificial magnetic conductor (AMC) plane is proposed for WLAN applications. Its dual-band operation is enabled by a rectangular patch in the 2.4 GHz band and a patch-etched slot dipole in the 5 GHz band. The proposed antenna is fully fabricated using textiles except for a feeding connector used for testing purposes and a via. Simulations and experiments agree well and validate that this low profile antenna operates with a good reflection coefficient, a high front-to-back ratio (FBR), and a low SAR value within the desired bands.

7.2.1 Characteristics of AMC plane

Various types of AMC plane have been studied in literature, . In this design, the square patch structure is chosen due to its ease in obtaining a large bandwidth [58], besides its fabrication simplicity when using textile materials. The topology of a single AMC unit cell is shown in Fig. 7-1 (a). The dielectric constant and loss tangent of the 1.5 mm thick felt substrate are 1.2 and 0.044 [204], respectively. ShieldIt Super conductive textile from LessEMF Inc. [175, 205], with an estimated conductivity of 1.18×10^5 S/m is used to form the metallic layers. The complete AMC plane consists of a periodic square patch structure on the top layer, a layer of substrate and a layer of ground at the reverse side. Each square patch is 18.2 mm in size and the period is 20 mm. Another layer of substrate is placed on top to separate the AMC plane from the antenna. CST MMS [177] is used to simulate the structure, using unit cell boundaries and Floquet ports to mimic the infinite planar periodicity. Fig. 7-1 (b) depicts the reflection coefficient (S_{11}) of the AMC with a plane wave incident from the normal direction. It can be clearly seen that the reflected wave is nearly in anti-phase at 2.45 GHz, where it is supposed to behave as a PEC. On the contrary, the phase of the reflected wave is about 0^o in the 5 GHz band, which exhibits a PMC-like characteristic. The operating bandwidth of the proposed AMC plane, defined by the phase of the reflected wave lying between $0^o \pm 90^o$, is from 5.04 GHz to 5.935 GHz. It is clear from the calculations that this proposed structure is capable of operating within the desired WLAN bands.

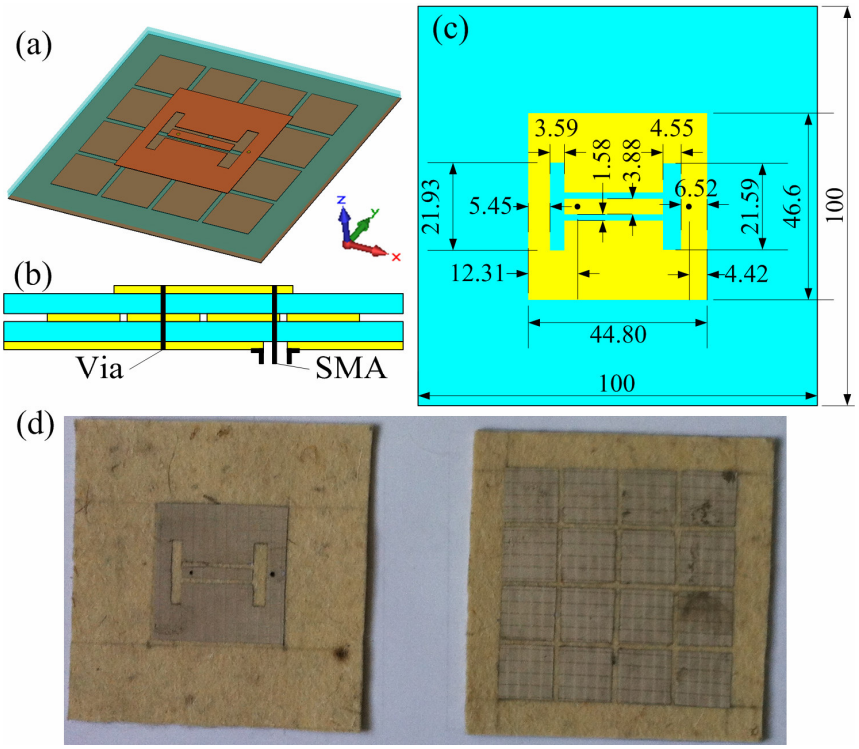

Fig. 7-2 Topology of the proposed antenna. (a) 3-D view, (d) side view, (c) top view, (d) fabricated prototype

7.2.2 **Antenna on AMC Plane**

The overall topology of the antenna is illustrated in Fig. 7-2. A coaxially-fed, rectangular patch antenna functions as a 2.45 GHz radiator. Due to the PEC-like behavior of the AMC plane in this band, the antenna performs similarly as a conventional microstrip patch antenna. Next, two slots in y-direction are introduced onto the rectangular patch. The rectangular dipole is chosen since it is easy to fabricate manually with simple tools. Note that different slot widths and lengths are selected to enable a wide impedance bandwidth. A coplanar waveguide (CPW) line which is about a quarter wavelength at 5.5 GHz is used to connect these two slots. The CPW line is connected with the structure's ground by a via, between the patch and the CPW strip. Since the slots cause perturbations of the current distribution on the patch in the lower 2.45 GHz band, the size of the patch has to be adjusted upon the integration of the slots. The antenna is optimized using the genetic algorithm in CST MWS with the aim of obtaining the best S_{11} in both frequency bands. The final dimensions of the proposed antenna are given in Fig. 7-2 (c).

The fabricated antenna prototype is shown in Fig. 7-2 (d). A comparison between simulated and measured S_{11} is shown in Fig. 7-3 (a). In the lower band, the maximum S_{11} is -16.2 dB (simulated) and -8.3 dB (measured), whereas this is -11.7 dB (simulated) and -12.5 dB (measured) in the upper band. Note that the slot dipole enables a much wider bandwidth than a simple microstrip patch antenna. Little disagreement between the simulated and measured curves is observed. This may be caused by the uncertainty concerning the textile substrate properties and the mechanical inaccuracies caused by the manual fabrication procedure with simple tools. Note that using machine dimensioning or laser cutting does not necessary lead to better results in practice, due to the unavoidable deformations of the antenna during practical operation. The most important is that the antenna performance still fulfills the requirements for WLAN communication.

A noticeable point is that the lower band splits into two resonances. This is related to the coupling between the large patch and the center CPW patch. At the first resonance, the currents on these two patches are in phase while at the second resonance they are out of phase. More details about mode coupling can be found in [151]. The S_{11} dip around 4 GHz represents the second mode (TM_{20}) of the patch.

The measured radiation patterns at 2.45 GHz and 5.2 GHz are shown in Fig. 7-3 (b)-(e). The FBR is higher than 12 dB in both bands. The high cross polarization in y-z plane is mainly caused by the CPW line which is perpendicular to the radiated slot, but that is not a concern in WLAN communication systems. The realized gain of the antenna is about 2.5 dB at 2.45 GHz, and between 0 to 4 dB in the higher band. The total efficiency is above 40 % throughout the whole operating band. This value is typical for textile antennas fabricated using this type of materials [206].

7.2.3 **Performance on Body**

The fabricated antenna prototype is measured on the chest of a male volunteer, who weighs 90 kg and is 178 cm in height. The result of this evaluation performed in an anechoic chamber is also shown in Fig. 7-3 (a). Due to the effectiveness of the ground plane, the S_{11} is only slightly affected by the coupling between the human body and the antenna. The maximum S_{11} is -9.8 dB and -8.4 dB in the lower and upper band, respectively.

Thanks to the large area available on the human chest and back, it is possible to enlarge the ground plane in order to further reduce the backward radiation. If this additional ground layer is a thin conductive textile layer, this may not affect the antenna conformability or the users' comfort.

Simulations for ground planes up to 200 × 200 mm^2 show that the S_{11} is nearly not affected while the back radiation is further reduced by a value between 5 and 10 dB, see Fig. 7-4.

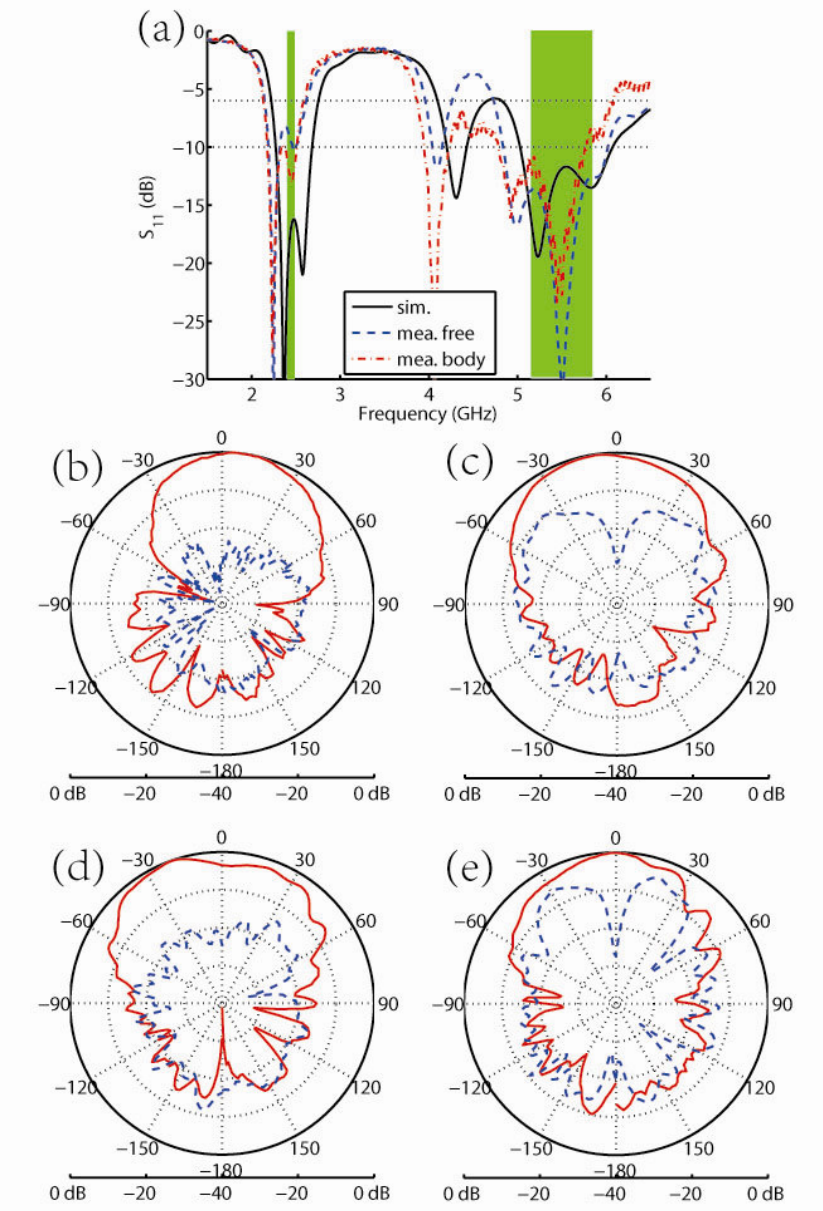

Fig. 7-3 Measured results of the antenna, (a) reflection coefficient, radiation pattern at 2.45 GHz in x-z plane (b) and y-z plane (c), radiation pattern at 5.2 GHz in x-z plane (d) and y-z plane (e). Solid (red) line: co-polarization, dashed (blue) line: cross-polarization.

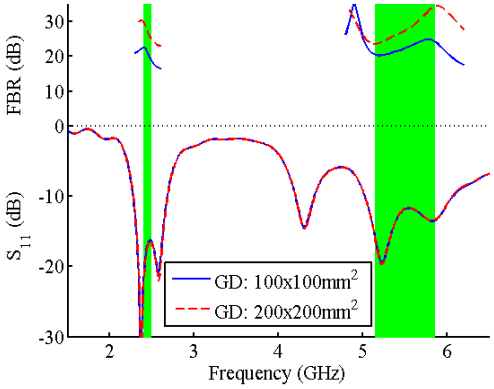

Fig. 7-4 Simulated results for several ground sizes.

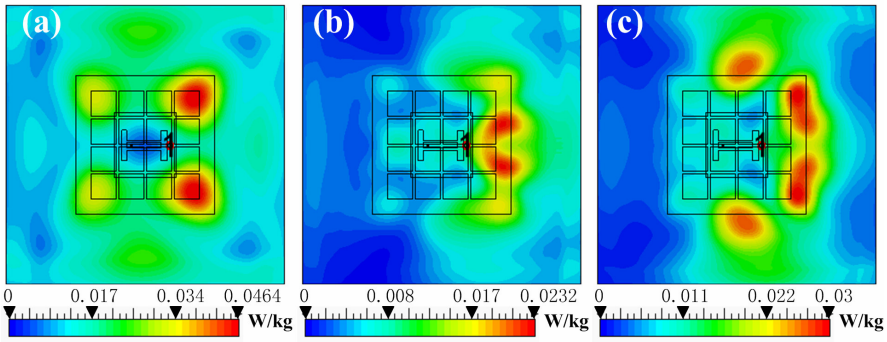

Fig. 7-5 SAR distributions at different frequencies. (a) 2.45 GHz, (b) 5.2 GHz, (c) 5.8 GHz.

The large ground is also expected to significantly reduce the SAR value. To analyze the contribution of the metasurface placed between the antenna and the human body, a series of SAR simulations was performed using a simplified human model in CST MWS. This model is defined behind the antenna, at 10 mm distance from the antenna ground layer in order to emulate practical antenna to skin distances in clothing. This distance is also larger than λ/4 at the lower operating frequency of 2.4 GHz, ensuring a proper distance from the edges of the combined antenna / metasurface. The model combines a 3 mm thick layer of skin, a 7 mm thick layer of fat, and a 60 mm thick muscle layer. This model has been validated in [178]. The input power to the antenna for SAR calculations in this work is set at 0.5 W (rms). SAR values were calculated based on the IEEE C95.1 standard and averaged over 10 g of biological tissue. The SAR distributions in both bands are displayed in Fig. 7-5. The calculated results are summarized in TABLE 7-I. Intuitively, measuring SAR at the exact same position using a common

antenna will result in higher SAR with increasing frequency. This is due to the conductivity of the human tissues, which increases with frequency [207]. However, in this case, it is clear from the simulated SAR values that the AMC is functioning well as a PMC at the higher frequencies. The SAR values observed in the 5 GHz band are lower compared to the 2.4 GHz band. Using an enlarged 200 x 200 m^2 ground plane, see TABLE 7-I, the SAR values were reduced with a factor of more than 10.

The antenna was also simulated when bent over a cylinder along the two main axes and for different radii. For the cylinder oriented along the x-axis, no significant S_{11} changes are observed. This is due to the direction of bending, which is parallel to the current on the patch, in this way not affecting the current distribution considerably. Conversely, the antenna S_{11} changes are more profound when it is bent along the y-axis, see Fig. 7-6. In the lower band, the resonant frequency shifts upwards as the radius of the cylinder is decreased. Nonetheless, even when bent the -10 dB operational bandwidth still covers the whole 2.4 GHz WLAN band. Meanwhile, the antenna operation in the upper band remains quasi unchanged. Only a slight S_{11} degradation can be seen at 5.85 GHz (with S_{11} = -9.32 dB).

TABLE 7-I
SIMULATED SAR

Freq. (GHz)	Antenna with 100x100 mm^2	Antenna with 200x200 mm^2
2.45	0.0464	0.00424
5.2	0.0232	0.00130
5.8	0.0300	0.00168

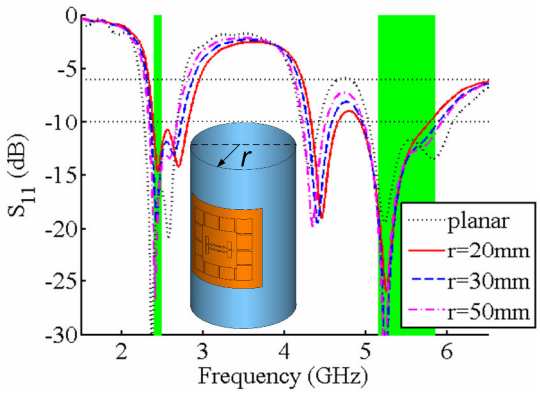

Fig. 7-6 Simulated reflection coefficients for bent topology.

TABLE 7-II
COMPARISON OF SEVERAL TEXTILE DUAL-BAND ANTENNAS

		CRLH-TL pach antenna	CRLH SIW antenna	Shorted SIW antenna	Patch & dipole on AMC	Magneto -electric dipole
References		[179]	[54]	[208]	[65]	[209]
Patch size (mm^2)		20 x 19	42 x 32	42 x 32	47 x 45	63 x 52
Ground size (mm^2)		50 x 50	82 x 72	102 x 92	100 x 100	100 x 100
Thickness (mm)		6.35	3.35	3.35	6.525	6.525
Lower band (2.4 GHz)	BW (MHz)	135	95	163	412	539
	η_{rad} (%)	17	20	55	40	50
	Gain (dB)	-3.5	-1.4	3.2	2.5	4.7
	FBR (dB)	10	10	15	15	20
	SAR (W/kg)	0.012	0.068	0.056	0.046	0.044
Upper band (5-6 GHz)	BW (MHz)	583	410	716	1046	1593
	η_{rad} (%)	75	60	61	55	60
	Gain (dB)	6.6	4.7	5.8	4	3.5
	FBR (dB)	15	10	18	20	20
	SAR (W/kg)	0.25	0.176	0.067	0.03	0.026

7.2.4 **Comparison of several textile dual-band antennas**

In Chapter 5, two dual-band textile patch antenna types were designed based on CRLH TL structures. In this chapter, two more textile antenna types were proposed. In TABLE 7-III, the performances of all these antennas are compared. The results in the table are calculated in free space for the planar topology.

The two antennas based on CRLH TL have the most compact size, but the price to pay is the limited bandwidth and the low radiation efficiency, especially in the lower frequency band. The reason is that the resonances in the structure yield large current densities in the lossy metallic vias or vertical walls, and the corresponding ohmic losses, significantly reducing the efficiency. Besides, the small grounds yield a relatively low FBR and high SAR values. Ref [208] proposed a kind of cavity antenna based on SIW technology. Its bandwidth and efficiency are improved compared to the two antennas discussed just above, but its radiation pattern shows a high level of

cross polarization. The antenna in [209] is a type of complementary dipole. This antenna and the antenna in this chapter (patch and dipole in combination with an AMC plane) have significantly larger sizes, but they support the largest bandwidth.

In general, a trade-off has to be made between the size and the performance of the antenna. The selection of a specific type should be based on the real application, involving the location of the antenna on the human body, and the bandwidth and gain required by the communication system.

7.3 A LOW PROFILE DUAL-BAND ANTENNA LOADED WITH ARTIFICIAL MAGNETIC CONDUCTOR FOR INDOOR RADAR SYSTEMS

A dual-band antenna is designed for a fall-detection radar and telemetry system. The radar is designed based on the Stepped Frequency Continuous Wave (SFCW) concept, which requires Ultra Wideband (UWB) operation, low inter-element coupling and a directive radiation pattern with low backlobe throughout its operating frequency band. The telemetry system uses the 2.45 GHz band to enable signal transmission/reception in an indoor environment and the 6–7.5 GHz band for radar sensing part. A main dual-band radiator with a slotted patch is used as the basis for the antenna design: the patch resonates at 2.45 GHz whereas the antenna slot enables a wide band operation for the radar system. This enables small (3.12 mm) structure thickness, while simultaneously maintaining a large bandwidth and a high front-to-back ratio (FBR). Numerical and experimental results show a good agreement and indicate a satisfactory antenna performance in terms of reflection coefficient and radiation pattern in the desired frequency bands. The antenna was also integrated into the radar system and tested in a real environment on three subjects at fixed distances. A fall-detection up to 6 meter was achieved.

7.3.1 A fall-detection radar and telemetry system

The elderly population (older than 65 years) numbered 500 million in 2006 worldwide. This is expected to double up to about 1 billion by 2030 [210]. While this number represents a socio-economic and medical advancement triumph over diseases, it also poses a serious challenge to the healthcare systems globally. The increase of age-related chronic diseases, such as congestive heart failure, chronic obstructive pulmonary disease, arthritis,

osteoporosis, and dementia also translates into a shortage of healthcare personnel, rising healthcare costs in tandem with the healthcare demands [211]. As privacy preference mainly motivates the elderly's wish to stay longer at home, an integrated home monitoring system is one of the most practical solutions.

Such system tracks an individual's activities on a continuous basis, feeding relevant information back to medical professionals and automatically alerts when an emergency occurs. It prevents delays in the deployment of emergency medical services in the event of accidents, which often result in serious physical and psychological consequences, permanent disabilities or even fatalities. During an emergency, conventional systems with a worn emergency press button are rendered useless in the event that an individual is already unconscious. Other monitoring based systems using video cameras, floor vibrations, or acoustic sensors, thus far are still unfavorable. In fact, video camera systems still present problems in case of low light environments, field of view, and the amount of data to be processed is very high. In addition, privacy is also a concern. Floor vibration and acoustic sensors are limited due to enviromental interference and background noise. Moreover, they present limitations in detecting soft falls, which is when the subject collides with an object (table, carpet, chair, etc).

The solution proposed in our previous work [212] uses a home-integrated radar system. It potentially overcomes above mentioned limitations via the deployment of several sensors, which are to be integrated in a wireless network. The home-monitoring radar system operates from 6 to 7.5 GHz based on the Stepped Frequency Continuous Wave (SFCW) concept for localization and speed detection using the Doppler principle. Moreover, it also requires operation at 2.4 GHz for telemetry. Besides operational requirements, the antenna also needs to be physically compact and low profile. This section is focusing on the antenna design of this system, with the aim of improving its front to back ratio (FBR) and further miniaturization of the antennas compared to [213]. Besides, it must radiate directionally within the frequency band of the radar, which will enable maximum transmitted power to the monitored user, and a maximum reflected power received by the receiving antenna during radar operation. Such antenna does not exist off-the-shelf and has to be custom-designed for this system.

It should be specified that a monostatic structure, that integrates a single antenna as transmitter and receiver simultaneously, will result in a more compact solution. Although it does not experience the cross talk, the poor

isolation between transmitter and receiver and the possible mismatch between the antenna and its feed line introduces a strong reflection that overwhelms the reflected signal. This unwanted reflection can be easily reduced in the case of a pure CW radar by an adequate passive microwave design. However, it cannot be reduced below a practical value (i.e., -30 dB as demonstrated in [212]) in ultra-wideband applications, where SFCW or FMCW are involved. It should be also noted that, in pulse radar, the undesired reflection can be avoided by time gating. However, this solution requires high-speed ADCs and high level processors, which is not preferable in low-cost in-door applications.

As mentioned earlier, the health monitoring system used in this work is based on an SFCW radar described by the authors in [212]. It consists of a sensor, combining both radar and wireless communications features, and a base station for offline data processing (Fig. 7-7). The sensor consists of a Quadrature SFCW radar, a Zigbee module, and a microcontroller, while the base station, consisting of a Zigbee module, a microcontroller, and a laptop, is used to determine offline the target's absolute distance and to distinguish a fall event from normal movements.

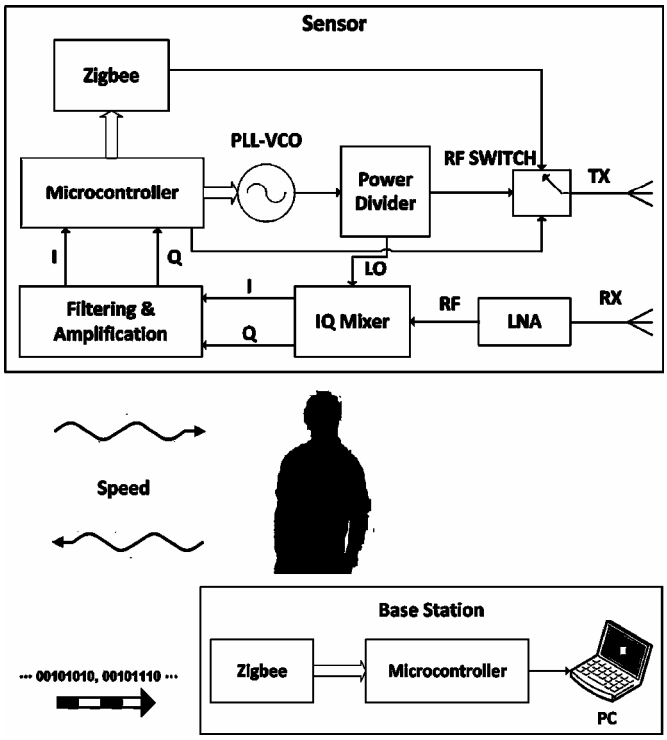

Fig. 7-7 Simplified block diagram of the indoor radar and health monitoring system [212].

The SFCW radar transmits N = 40 CW pulses, called *burst*, whose frequencies are increased from pulse to pulse by a fixed frequency increment Δf = 25 MHz. Each pulse is T = 100 μs long, while the total band $N \cdot \Delta f$ is 1 GHz positioned in the UWB band between 6 and 7 GHz. This solution allows having an unambiguous range of 6 m with a resolution of 15 cm. A transmitted power of 0 dBm is sent to the antenna. More details on the system architecture are available from [214].

In order to determine the target's absolute distance, the entire burst is received and processed by combining the resulting IQ baseband signals to produce complex samples. The target's range profile can then be determined applying the Inverse Fast Fourier Transformer (IFFT) [215]. For the fall detection purpose, a movement classification based on a Least Squares Support Vector Machines (LS-SVM) framework combined with Global Alignment (GA) kernel [214] is applied to discriminate fall events from other activities, such as random walking, sitting down, standing up, and no movements. This technique, aiming at evaluating the changes in speed experienced during a fall or a normal movement, consists of two stages of data analysis, namely the training phase and the testing phase. In the training phase, speed activities experienced during on the one hand falling, and on the other hand daily activities (e.g., walking, sitting down, and standing up) are used to built a model that groups those signals into two main classes; fall events and normal movements. The testing phase is then used to validate the classification model considering activities which have not been used to train the model. Both phases use a digitized speed signal as input. The target's speed can be determined considering only one frequency among the 40 CW pulses from the SFCW waveform, utilizing the Doppler concept. In this work, the frequency 6.5 GHz has been chosen to realize a CW Doppler radar. A detailed description of the data processing techniques for fall detection and tagless localization purposes are well beyond the scope of this work. More details are provided in [214, 215].

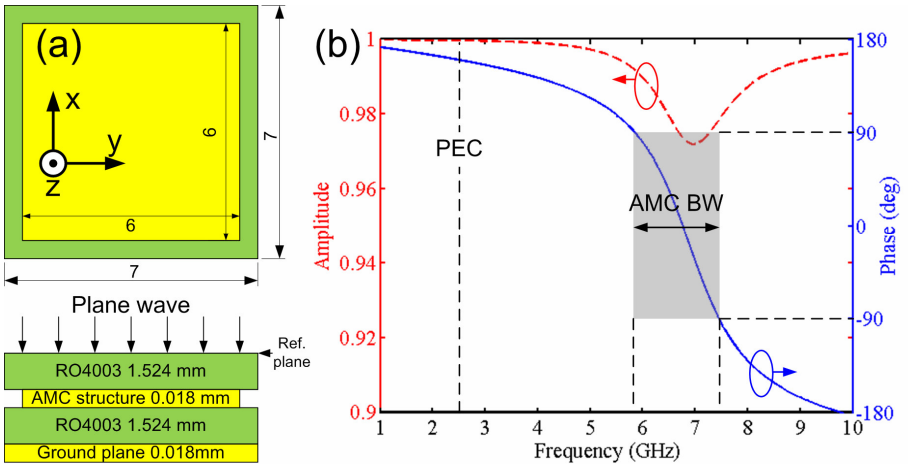

Fig. 7-8 (a) Topology, and (b) reflection coefficient of the AMC structure.

7.3.2 **AMC structure**

To maintain fabrication simplicity, a simple square patch array with out vias is chosen as the basis of the AMC. Vias across layers, which add to fabrication complexity and are avoided [25]. The topology of the AMC structure is shown in Fig. 7-8 (a). The substrate chosen is Rogers RO4003 (ε_r = 3.55, tan δ = 0.027), each with a thickness of 1.524 mm. Another layer of substrate with the same thickness is used on top to separate the antenna and the AMC structure. Fig. 7-8 (b) displays the reflection for this structure for an incident plane wave simulated using CST Microwave Studio. Unit cell boundaries and Floquet ports are used in the simulation. It can be seen that the reflective phase is nearly 180^o around 2.45 GHz, which confirms the functioning as a normal conducting plane. The reflective phase of the AMC changes to zero at 6.75 GHz, which is necessary to function as a PMC. The upper bandwidth defined as $0^o \pm 90^o$ is from 5.8 GHz to 7.5 GHz.

7.3.3 **AMC-loaded patch antenna**

Since the AMC plane is working as a PEC plane around 2.45 GHz, the design process for the patch antenna is quite straightforward. An 8 × 8 array is used in the finite AMC design. The patch is located in the center of the AMC plane and a coaxial connector is used to feed the patch from the rear side of the AMC. The width and length of the patch are nearly half a wavelength. However, considering that the AMC slightly influences the substrate permittivity and permeability, the size of the patch had to be optimized.

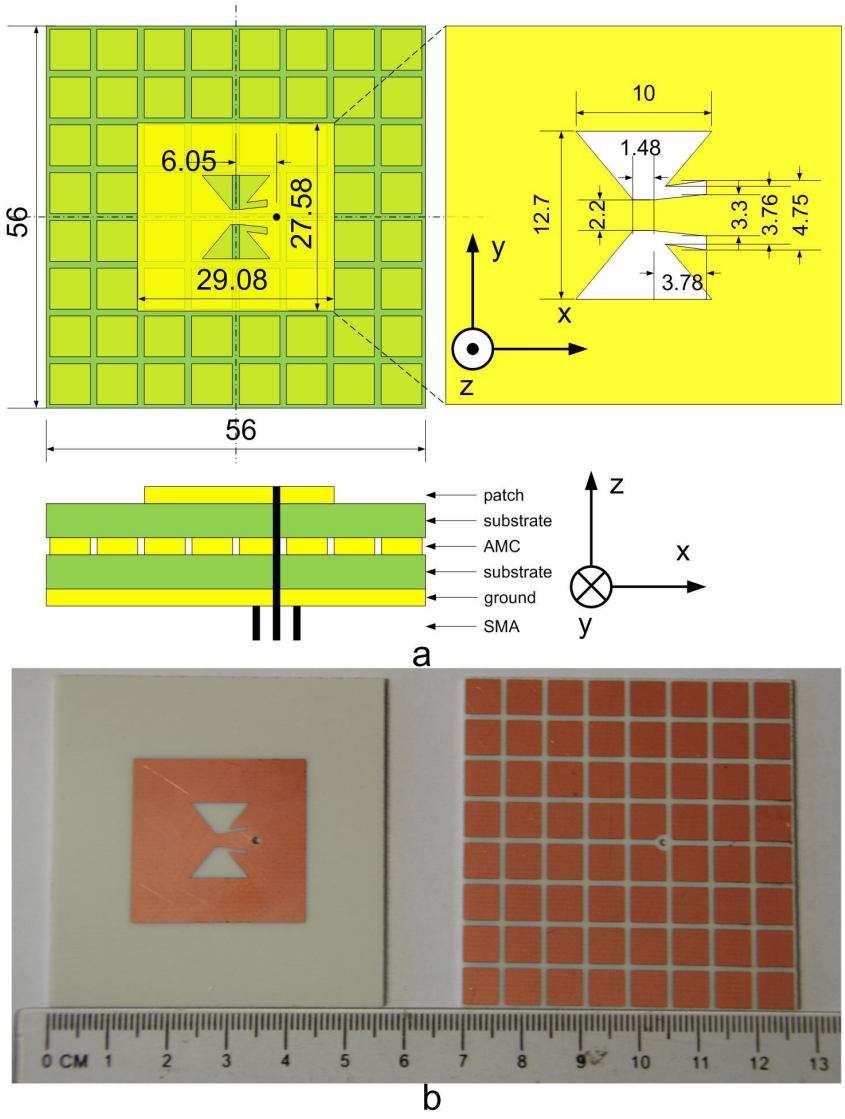

Fig. 7-9 Antenna topology. (a) Antenna layout and cross section with physical dimensions in mm, (b) Fabricated antenna prototype, left: top metal layer with a patch antenna and a slot dipole; right: intermediate metal layer showing the square AMC plane.

Next, a bowtie slot is embedded within the patch, as shown in Fig. 7-9. This idea was initiated by the fact that a bowtie dipole provides a wider bandwidth than a simple dipole antenna. The bowtie slot is parallel to the radiating edges of the patch in order to match polarization. The slot antenna is fed by a CPW line, which is optimized in order to obtain proper

impedance matching. Since the slot changes the current distribution on the patch, the size of the patch and the position of the feeding probe have to be chosen with care. The genetic algorithm optimizer in CST MWS is used to obtain the best reflection coefficient in both frequency bands.

Fig. 7-10 gives the simulated and measured reflection coefficient of this antenna. Simulation shows a -10 dB bandwidth from 2.4 GHz to 2.85 GHz, whereas measurements yield a minimum -6 dB reflection coefficient (S_{11}) within the same operating frequency band. A second patch resonance also exists at about 5.2 GHz. However, since in this case the main beam is not directed broadside, this frequency band is not suitable for use in our radar system. In the upper band, the slot bowtie antenna functions as the major radiator. The simulated and measured frequency bandwidths are from 5.8 GHz to 8.9 GHz and from 5.95 GHz to 9.1 GHz, respectively. The minor frequency shift is caused by a small air gap in between the two substrates. Simulations showed that this level of shift is obtained for an air gap of 0.07 to 0.08 mm, which is very feasible in the fabricated structure.

It is also interesting to evaluate the practical functionality of the AMC. This is performed by calculating the proposed antenna with and without the AMC layer, see Fig. 7-10 (red dashed line). This validation clearly indicates that the patch antenna is immune for the influence of the AMC structure. It confirms the AMC functionality as a PEC plane in the 2.45 GHz band. Conversely, the AMC improves the impedance matching significantly in the upper frequency band when functioning as a PMC plane.

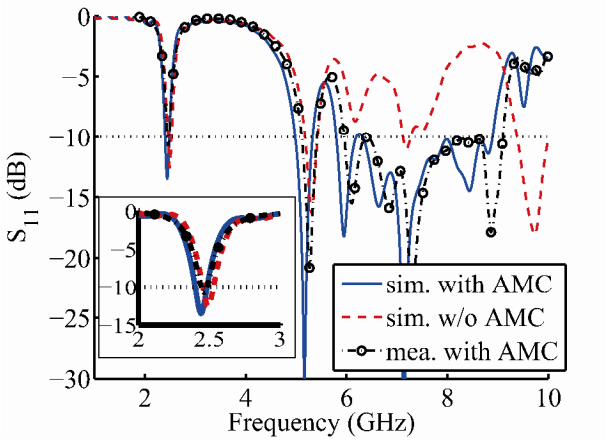

Fig. 7-10 Measured and simulated reflection coefficient (S_{11}) of the antenna, the zoomed around 2.5 GHz is shown.

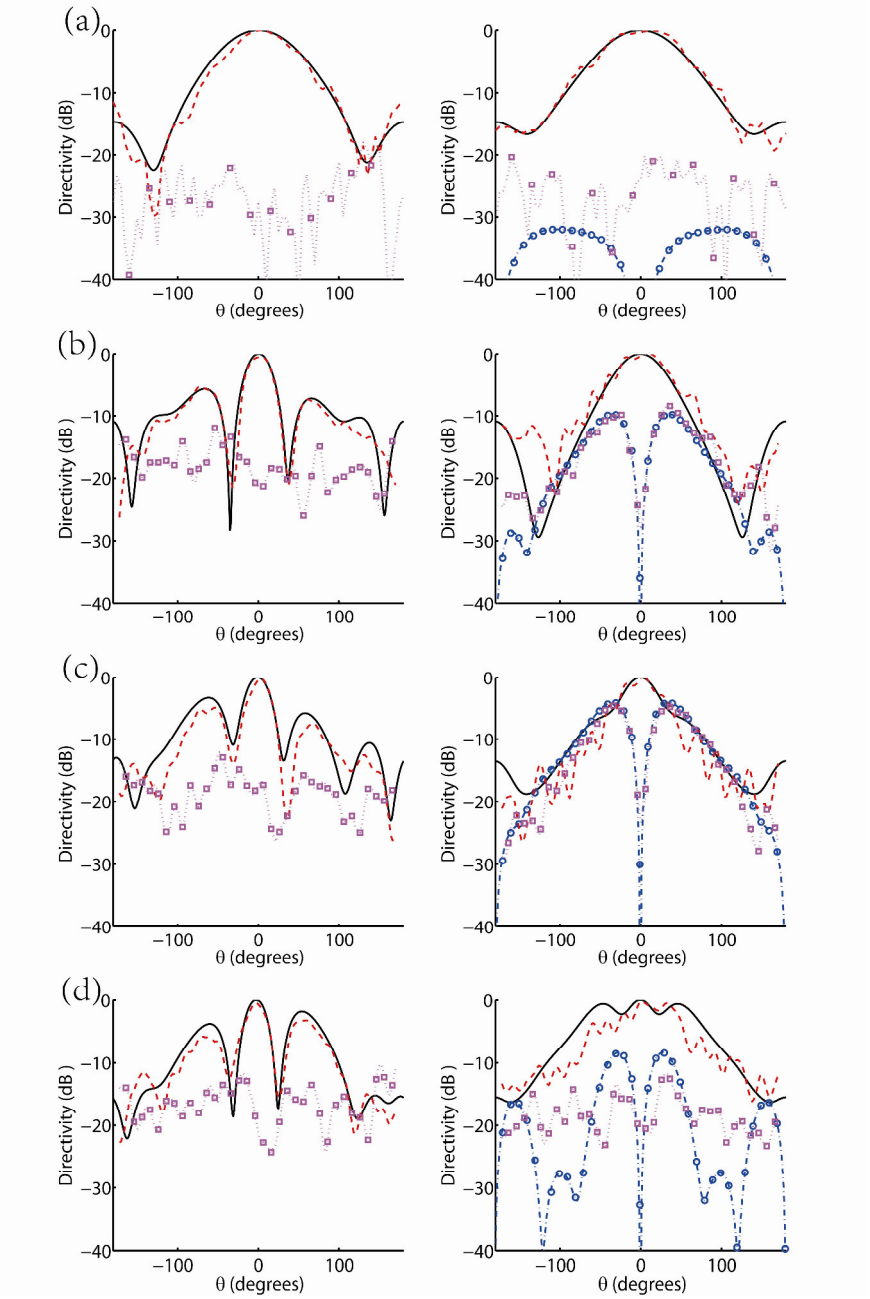

Fig. 7-11 Radiation pattern of the antenna. a. radiation pattern at 2.45 GHz; b. radiation pattern at 6.5 GHz; c. radiation pattern at 7.0 GHz; d. radiation pattern at 7.5 GHz. black solid line: simulated co-polarized, red dashed line: measured co-polarized, blue dashdot line with circular markers: simulated cross-polarized, magenta dotted line with square markers: measured cross-polarized. (In x-z plane, the simulated cross polarized levels are below -30 dB)

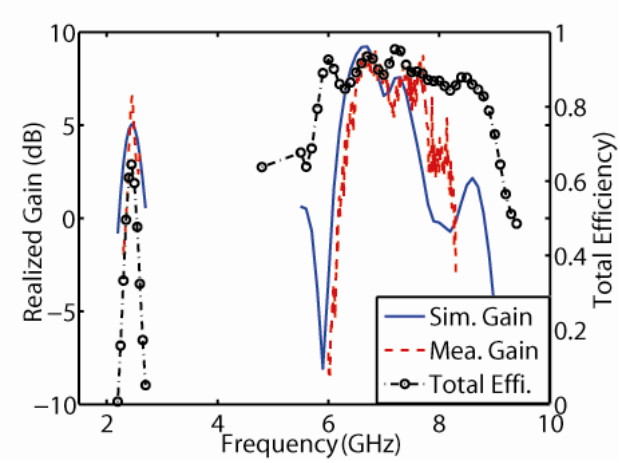

Fig. 7-12 Realized gain and total efficiency of the antenna.

Fig. 7-11 shows the radiation patterns of the antenna. Since around 2.45 GHz the operating mechanism is similar to the one of a conventional patch antenna, the radiation pattern exhibits a good 15 dB FBR at 2.45 GHz. Since the current on the patch surface is distorted by the slot dipole and CPW lines, the efficiency of the patch mode is a little lower than the conventional patch antenna. Nonetheless, the totally efficiency of 72 % at 2.45 GHz is still acceptable for WLAN operation. Moreover, FBRs of more than 11 dB are produced by the slot dipole throughout the whole AMC operating bandwidth, see Fig. 7-8 (b), due to the latter's effectiveness as a reflector. Note that although the antenna's simulated total efficiency is nearly 90% throughout the whole band (see Fig. 7-12), its radiation pattern is incapable of maintaining a consistent forward main beam when operating outside the AMC bandwidth [56, 57]. This is evident from Fig. 7-11 (d), where sidelobes that are larger than the main lobe occur. A simultaneous degradation of the antenna's realized gain from 5 dB to 0 dB also confirms this behavior. The higher measured cross polarization in x-z plane is believed to be due to the feeding cables placed perpendicularly to the antenna during evaluation. With these observations, it is concluded that the suitable frequency band for this antenna for application in the radar system is from 6 GHz to 7.5 GHz.

7.3.4 **Antenna cross-coupling**

Since two antennas are needed for radar transmission and reception, cross-coupling can overwhelm an already weak reflected signal [213]. A simple method to reduce such cross-coupling is to increase the element spacing

between the two antennas, besides implementing vertical walls, as used in our previous investigation [213]. However, using any of the two techniques used will result in either a larger area and/or thickness requirements for deployment of the radar system. Thus a tradeoff must be found. Fig. 7-13 presents the measured cross-coupling between two antennas. The distance between the antennas is varied from 10 cm to 20 cm, representing wavelengths of between 2.25 λ and 4.5 λ. (with λ the free space wavelength at the center frequency 6.75 GHz). When a 10 cm distance between the centers of the antennas is set, less than -25 dB of cross-coupling exists within the radar frequency band. This is significantly reduced to lower than -38 dB when the spacing is increased to 20 cm. Since a cross-coupling lower than -25 dB is estimated to be sufficient for a 5 m detection, as will be presented in section 6, the 10 cm spacing has been chosen for the practical radar system implementation. Note that this distance is the center-to-center spacing between the antennas, which means that the antenna edges are only 4.4 cm apart. Compared to our previous work in [213], a 4 cm edge-to-edge antenna spacing was used, besides the need to implement a metallic vertical wall to reduce cross-coupling between the two antennas. The antenna spacing used in the previous work is comparable to the current implementation, with the added advantages of a larger detection distance, better resolution and a compact (thinner) antenna size with the use of the proposed antenna. The total performance of the antenna is compared to the bowtie monopole antenna of [213] in TABLE 7-III.

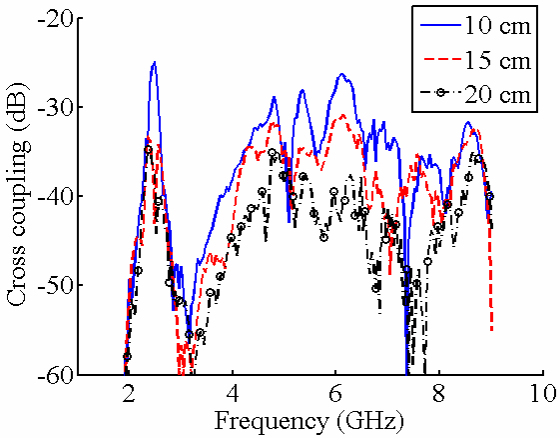

Fig. 7-13 Measured cross-coupling between two antennas with different distances: 10 cm, 15 cm and 20 cm.

TABLE 7-III
COMPARISON OF THE PROPOSED ANTENNA TO THE BOWTIE MONOPOLE ANTENNA IN [213]

	Proposed antenna	**Antenna in [213]**
Size (mm^3)	56×56×3.12	42×36×32
Low Freq. Band (GHz)	2.395-2.485	2.22-2.48
High Freq. Band (GHz)	5.78-8.89	5.8-6.77
Gain (dB) 2.45 GHz	5.05	5.7
Gain (dB) 6-7 GHz	>7.0	>7.2
FBR (dB) 2.45 GHz	15	0
FBR (dB) 6-7 GHz	>11	>7.5
Cross coupling (dB) without metallic wall	<-25	<-25 (with wall)

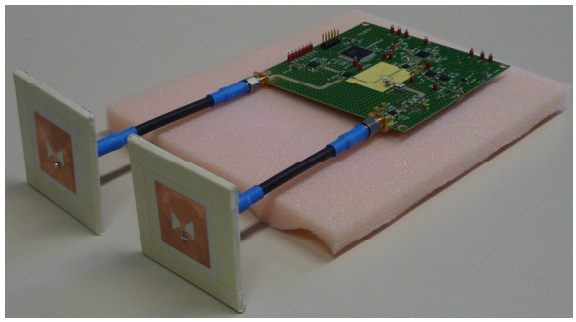

Fig. 7-14 Photo of the radar system set-up

7.3.5 **Radar experimental results**

The system set-up is shown in Fig. 7-14. Similar to the previous work, experimental validations have been conducted in a 4 x 6 m^2 corridor on three human volunteers with the sensor fixed to the wall at 1.25 m of height. Furniture and metal shelves were deliberately left to be present in the environment to test the system under real circumstances. In this evaluation, the three subjects are similar in their heights (1.75 m) and weighs between 65 kg and 90 kg. Only one subject was present in the corridor at a time during evaluations, and was allowed to move without any constraints. Since a series of sensors are planned to be deployed within a room, only frontal falls were considered and invoked at different absolute distances away from the radar antennas. Two big pillows have been used to avoid injuries.

1. Fall Detection

The classification model has been generated using 80 activities of one person, who did not contribute to the testing phase. More precisely, 25 of these

activities are random walking activities, 30 signals were acquired during sitting down and standing up repetitions with the target located at different distances and orientations from the antenna, and finally 25 frontal falls were acquired with the target falling at different positions in the corridor.

The model has been tested on 120 signals acquired from three different persons under test who had not contributed to the training phase. In particular, 60 activities were fall events invoked at four distances, from 3 m to 6 m, with a distance step of 1 m, and 60 were walking movements. Each subject performed 5 frontal falls for each position. The corresponding experimental results are presented in TABLE 7-IV. The experimental evaluations indicate that the radar sensor with the dual-band antenna is able to successfully detect a high rate of fall events even at far distances away from the antennas, without reporting any false positives.

TABLE 7-IV
SUCCESS RATE IN FALL DETECTION AND FALSE POSITIVES

% Fall Detection Success Rate				% False Positives
Distance	Target 1	Target 2	Target 3	
3 m	100	100	100	
4 m	100	100	100	0
5 m	100	80	100	
6 m	100	80	80	

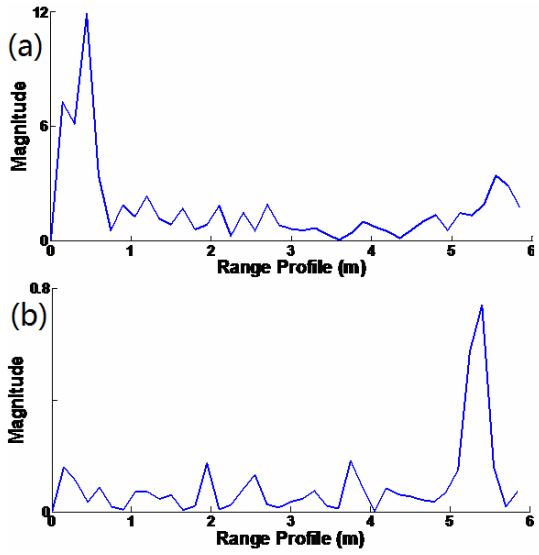

Fig. 7-15 Range profile of a target at about 5.5 m away from the antennas before (a) and after (b) applying data processing.

2. Tagless localization

Fig. 7-15 shows the range profile of a person at about 5.5 m away from the antennas. This range profile shows the signal reflection from the objects/persons within the radar detection range on the x-axis. The magnitude of the signal reflected by the target after processing using FFT is shown on the y-axis. Fig. 7-15 (a) shows that the target's peak is totally overwhelmed by the undesired reflections originating from the clutter and the antenna's cross-coupling. However, upon applying the data processing technique described in [215], the target's peak can be clearly detected, as shown in Fig. 7-15 (b). Since the radar range resolution is 15 cm, the maximum error in localization is about 7.5 cm.

It should be noted that the increased target detection distance results from the significantly reduced cross-coupling and signal backscattering from the antennas. In fact, in indoor remote radar sensing applications, the signal-to-clutter ratio is the factor that typically limits the performance of radar systems. Thus, as was measured in section 5, the new antennas' cross-coupling and backscattering is confirmed to have improved these ratios, enabling better radar system capabilities and more desirable hardware characteristics.

7.4 CONCLUSION

A type of low profile dual-band antenna is proposed based on the AMC plane. This novel structure combines a patch antenna and a slot dipole to enable its dual-band property, whereas the AMC is used to effectively suppress back radiation and, consequently, electromagnetic coupling with the objects behind the antenna. The simplicity of the topology used enables its realization using flexible textile materials and a simple manual fabrication procedure. Both simulations and measurements performed in free space and on body indicated a satisfactory performance in terms of bandwidth and radiation properties for dual-band WBAN/WLAN applications. Another prototype is designed for an indoor radar and telemetry system. Features like low-profile, high FBR, wide band, antenna isolation of less than – 25 dB are obtained with a 10 cm centre-to-centre antenna spacing within the radar operating band. The antennas were integrated into an indoor radar system before being practically evaluated on three human volunteers performing frontal falls and normal movements at different distances away from the setup. Proper radar operation in detecting falls of up to 6 m with at least 80 % success rate and 7.5 cm distance resolution in a real indoor environment was obtained.

Chapter 8

CONCLUSION AND OUTLOOK

8.1 CONCLUSIONS

The main target of this PhD was to deeply study the characteristics of metamaterials, and to use them to improve the performance of microwave antennas. The research performed can be subdivided into two parts, one is pure metamaterial design, and the other is antenna design.

The first part of this research mainly focused on the design of the metamaterial itself. This included three topics: wideband negative refractive index (NRI) metamaterials, planar chiral metasurfaces, and complex meta-molecules.

The volumetric NRI metamaterial is the most popular type of metamaterial, but the narrow NRI bandwidth limits its application in the design of microwave antennas and devices. A coating method has been proposed to increase the NRI bandwidth for metamaterials composed by dielectric spheres. By using suitable coating materials with optimal permittivity and thickness, the NRI bandwidth can be increased 60% compared with nude spheres (without coating). This kind of dielectric sphere metamaterial has no conductor losses and is quasi isotropic due to inherent symmetries, which is not only desirable in the microwave frequency band, but also at optical frequencies.

Another group of metamaterials is chiral media, which generate a large chirality that can hardly be obtained with natural materials. Two types of planar chiral structures have been studied: one is based on a twisted pair of resonators and the other is based on a displaced pair or resonators. Prototypes were fabricated and measured in the microwave frequency band. The chiral phenomenon is physically explained based on the field distributions in the structures. Since these designs have a totally planar

topology, it is easy to fabricate and integrate them with other devices. Applications as polarizers and tunable metamaterials have been discussed.

To obtain novel properties for metamaterials, it is necessary to design dedicated unit cells for metamaterials, also called metamolucules. A new kind of planar metamaterial was investigated, which consists of meta-molecules where a first resonator encapsulates a second resonator. The near-field coupling between these resonators is the dominating effect determining the characteristics of the material. This coupling has been discussed in detail at a physical level. The technique of encapsulating allows both to miniaturize the unit cell, which is advantageous with respect to making the material homogeneous, and to invoke strong coupling, which is advantageous for tuning the material and have wide application in the field of compact sensors.

The second part of this PhD project has been the design of antennas loaded with metamaterials. This part can further be subdivided into three subparts: dual-band textile patch antennas, radial patch antennas loaded with CRLH TL, and low profile antennas based on an AMC plane.

To the best knowledge of the author, in this work metamaterals have been introduced in wearable antenna design for the first time. Dual-band patch antennas have been proposed based on linear composite right/left-handed transmission lines (CRLH TL). The symmetric modes of the CRLH TL are used in the design, and produce similar field distributions and radiation patterns in the two operating bands. The antennas show high front-to-back ratio (FBR) and low specific absorption rate (SAR) values, which is quite suitable for textile materials. A final prototype has been designed that shows flexible characteristics and a robust performance.

A radial CRLH TL has different characteristics compared to a linear one. The circuit model for this kind of structures has been conceived in this PhD for the first time. This has been used in the design of circular and sector patch antennas operating at zeroth order resonance (ZOR) mode. Since the resonant frequency of this mode is independent of its physical size, it can be used to design electrically small antennas with a compact size, or electrically large antennas with a high directivity. A matching network has also been considered, which may provide a wider operating band than simple probe feeding. Similar as in the case of the linear CRLH TL, the radial CRLH TL can also be used to design dual-band or multi-band antennas. A noticeable advantage is that the radiation patterns in all the bands are omni-directional in the horizontal plane. This is desirable in a lot of wireless communication

systems. Several prototypes have been fabricated. Measured results agree well with numerical results.

Low profile antennas based on an artificial magnetic conductor (AMC) plane can provide a wider bandwidth than simple patch antennas. A patch-etched slot dipole antenna with AMC ground plane has been designed. In the lower band, the AMC operates as a normal perfect electric conductor (PEC) ground for the patch antenna, while in the upper band, the behavior of the AMC plane is like a perfect magnetic conductor (PMC) plane, which can be used as the reflector for the slot dipole antenna. Since the unit cell of the AMC plane is a simple square patch, the antenna is easy to design and optimize. It is also suitable to be fabricated from textile materials. One textile antenna has been designed and fabricated, featuring a high FBR and low SAR value in a wide band. Another antenna prototype has been designed for a fall-detection radar and telemetry system. Both the antenna and the system show a very good performance.

8.2 OUTLOOK AND FUTURE RESEARCH

The research in metamaterials is an interdisciplinary field which involves a lot of subjects, e.g. physics and chemistry, material technology, computational electromagnetics, and application in devices. Metamaterials have attracted huge attention and obtained remarkable successes in all these fields. Here, we only point out several potential directions that can be investigated in the field of antenna design.

1. Metamaterial based antennas for wearable applications. Wearable electronic systems are very attractive for e.g. continuous medical monitoring, emergency rescue services, physical training, care for children and the elderly, etc. As a consequence, the concept of Wireless Body Area Networks (WBAN) has become a more widespread research topic. As a critical component of these systems, the wearable antenna plays a key role for the wireless communication with other devices on or off the body. However, the design flowchart for wearable antennas is quite different compared to the traditional ones because of the special material properties and various operating environments of the wearable antennas. The antennas are desired to have robust performances under slight deformation and large fabrication tolerances. The coupling between the antennas and the human body will influence the performance of the antenna. The human health risk under long exposure conditions to the radiation involved should also be considered in the design. Based on our initial study, metamaterials have shown great advantages and potential in the field of

wearable antennas.

2. Implanted antenna design. Implanted antennas and devices have abundant medical applications. However, the operating environment is totally different from the “normal” environment for antennas. The human body causes noticeable radiation loss for the necessarily compact antennas. Obviously, implanted antennas may benefit from the features of metamaterials, which may provide a sufficient miniaturization while keeping a reasonable radiation level. Besides, reconfigurable antennas may be realized by using tuneable metamaterials. They could keep their operating frequency constant in varying surroundings with different physical parameters.

3. Antenna design for next generation wireless communication systems. This new generation is typically assigned new frequency bands and a wider spectrum per frequency channel. The application of millimeter wave communication needs antennas operating in the 60 GHz band or the 90 GHz band. Besides, multiple-input and multiple-output (MIMO) technology requires antenna diversity. Metamaterials allow an antenna with a more flexible shape and size, while being independent of the operating frequency. They can also help to improve the isolation from neighboring antennas in a diversity array, so to improve the MIMO performance.

4. Chip antenna design. When operating in the millimeter wave frequency band, the chip antenna may become more popular, since printed circuit board (PCB) technology cannot provide a sufficiently low dimensional tolerance, which may invoke a too high insertion loss from the circuit to the antenna. The design of chip antennas needs to comply with the basic rules of chip technology, with given substrate thicknesses and the special vertical connection technology. The main challenge in chip antenna design is the low thickness of the substrates, which will limit the bandwidth and radiation efficiency of the antennas. The technology studied in this PhD can be used to yield a wider bandwidth with a lower profile for these thin substrates. Chip antennas in combination with external structures, like lenses, reflectors, or especially superstrates based on metasurfaces are also a possibility, possibly providing more functionality. The topologies as described Chapters 5 and 6 could form a basis for that.

BIBLIOGRAPHY

[1] Wikipedia. Metamaterial. Available http://en.wikipedia.org/wiki/Metamaterial.

[2] M. Lapine, and S. Tretyakov, "Contemporary notes on metamaterials," *IET Microwaves, Antennas & Propagation,* vol. 1, no. 1, pp. 3-11, 2007.

[3] A. Sihvola, "Metamaterials in electromagnetics," *Metamaterials,* vol. 1, no. 1, pp. 2-11, 2007.

[4] J. B. Mandelstam, "Group velocity in crystal lattice," *Zh. Eksp. Teor. Fiz,* vol. 15, no. 9, pp. 475-478, 1945.

[5] V. G. Veselago, "The electrodynamics of substances with simultaneously negative values of ε and μ," *Soviet Physics Uspekhi,* vol. 10, pp. 509-514, 1968.

[6] R. A. Shelby, D. R. Smith, and S. Schultz, "Experimental Verification of a Negative Index of Refraction," *Science,* vol. 292, no. 5514, pp. 77-79, 2001.

[7] J. B. Pendry, A. J. Holden, D. J. Robbins *et al.*, "Magnetism from Conductors and Enhanced Nonlinear Phenomena," *IEEE Transactions on Microwave Theory and Techniques,* vol. 47, pp. 2075-2084, 1999.

[8] W. J. Padilla, D. N. Basov, and D. R. Smith, "Negative refractive index metamaterials," *Materials today,* vol. 9, no. 7, pp. 28-35, 2006.

[9] N. I. Zheludev, "The Road Ahead for Metamaterials," *Science,* vol. 328, no. 5978, pp. 582-583, 2010.

[10] C. Caloz, "Next-Generation Metamaterials for Unprecedented Microwave Systems," in TELSIKS, Serbia, Nis, Oct. 2011, pp. 3-12.

[11] R. C. McPhedran, I. V. Shadrivov, B. T. Kuhlmey *et al.*, "Metamaterials and metaoptics," *NPG Asia Materials,* vol. 3, no. 11, pp. 100-108, 2011.

[12] N. Zheludev, and Y. S. Kivshar, "From metamaterials to metadevices," *Nature Materials,* vol. 11, pp. 917-924, Nov. 2012.

[13] A. Alu, N. Engheta, A. Erentok *et al.*, "Single-negative, double-negative, and low-index metamaterials and their electromagnetic applications," *IEEE Antennas and Propagation Magazine,* vol. 49, no. 1, pp. 23-36, 2007.

[14] M. Wheeler, J. Aitchison, and M. Mojahedi, "Coated nonmagnetic spheres with a negative index of refraction at infrared frequencies," *Physical Review B,* vol. 73, no. 4, 2006.

[15] S. H. Lee, C. M. Park, Y. M. Seo *et al.*, "Reversed Doppler effect in double negative metamaterials," *Physical Review B,* vol. 81, no. 24, pp. 241102, 2010.

[16] N. Seddon, and T. Bearpark, "Observation of the iverse doppler effect," *Science,* vol. 302, no. 5650, pp. 1537-1540, 2003.

[17] J. Lu, T. M. Grzegorczyk, Y. Zhang *et al.*, "Crenkov radiation in materials with negative permittivity and permeability," *Optics Express,* vol. 11, no. 7, pp. 723-734, 2003.

[18] S. N. Galyamin, A. V. Tyukhtin, A. Kanareykin *et al.*, "Reversed Cherenkov-transition radiation by a charge crossing a left-handed medium boundary," *physical Review Letters,* vol. 103, no. 19, pp. 194802, 2009.

[19] G. Dolling, C. Enkrich, M. Wegener *et al.*, "Simultaneous Negative Phase and Group Velocity of Light in a Metamaterial," *Science,* vol. 312, pp. 892-894, May 2006.

[20] O. F. Siddiqui, M. Mojahedi, and G. V. Eleftheriades, "Periodically loaded transmission line with effective negative refractive index and negative group velocity," *IEEE Transactions on Antennas and Propagation,* vol. 51, no. 10, pp. 2619-2625, Oct. 2003.

[21] D. Sievenpiper, L. Zhang, R. F. Broas *et al.*, "High-Impedance Electromagnetic Surfaces with a Forbidden Frequency Band," *IEEE Transactions on Microwave Theory and Techniques,* vol. 47, no. 11, pp. 2059-2074, 1999.

[22] F. Yang, and Y. Rahmat-Samii, "Reflection phase characterizations of the EBG ground plane for low profile wire antenna applications," *IEEE Transactions on Antennas and Propagation,* vol. 51, no. 10, pp. 2691-2703, 2003.

[23] A. Vallecchi, J. R. De Luis, F. Capolino *et al.*, "Low Profile Fully Planar Folded Dipole Antenna on a High Impedance Surface," *IEEE Transactions on Antennas and Propagation,* vol. 60, no. 1, pp. 51-62, 2012.

[24] A. Pirhadi, M. Hakkak, F. Keshmiri *et al.*, "Design of Compact Dual Band High Directive Electromagnetic Bandgap (EBG) Resonator Antenna Using Artificial Magnetic Conductor," *IEEE Transactions on Antennas and Propagation,* vol. 55, no. 6, pp. 1682-1690, 2007.

[25] H. Mosallaei, and K. Sarabandi, "Antenna miniaturization and bandwidth enhancement using a reactive impedance substrate," *IEEE Transactions on Antennas and Propagation,* vol. 52, no. 9, pp. 2403-2414, 2004.

[26] X. Chen, L. Li, C. Liang *et al.*, "Dual-Band High Impedance Surface With Mushroom-Type Cells Loaded by Symmetric Meandered Slots," *IEEE Transactions on Antennas and Propagation,* vol. 60, no. 10, pp. 4677-4687, Oct. 2012.

[27] N. Landy, S. Sajuyigbe, J. Mock *et al.*, "Perfect Metamaterial Absorber," *Physical Review Letters,* vol. 100, no. 20, pp. 207402, 2008.

[28] M. Li, S. Xiao, Y. Bai *et al.*, "An Ultrathin and Broadband Radar Absorber Using Resistive FSS," *IEEE Antennas and Wireless Propagation Letters,* vol. 11, pp. 748-751, 2012.

[29] Wikipedia. Chirality (electromagnetism). Available http://en.wikipedia.org/wiki/Chirality_%28electromagnetism%29.

[30] J. K. Gansel, M. Thiel, M. S. Rill *et al.*, "Gold Helix Photonic Metamaterial as Broadband Circular Polarizer," *Science,* vol. 325, no. 5947, pp. 1513-1515, 2009.

[31] Y. Ye, and S. He, "90° polarization rotator using a bilayered chiral metamaterial with giant optical activity," *Applied Physics Letters,* vol. 96, no. 20, pp. 203501, 2010.

[32] N. I. Zheludev, E. Plum, and V. A. Fedotov, "Metamaterial polarization spectral filter: Isolated transmission line at any prescribed wavelength," *Applied Physics Letters,* vol. 99, no. 17, pp. 171915, 2011.

[33] J. H. Shi, H. F. Ma, W. X. Jiang *et al.*, "Multiband stereometamaterial-based polarization spectral filter," *Physical Review B,* vol. 86, no. 3, pp. 035103, 2012.

[34] S. Yan, and G. A. E. Vandenbosch, "Compact circular polarizer based on chiral twisted double split-ring resonator," *Applied Physics Letters,* vol. 102, no. 10, pp. 103503, 2013.

[35] I. V. Lindell, A. H. Sihvola, S. A. Tretyakov *et al.*, *Electromagnetic waves in chiral and bi-isotropic media*: Artech House, Norwood, MA, 1994.

[36] A. Serdyukov, I. Semchenko, S. Tretyakov *et al.*, *Electromagnetics of bi-anisotropic materials: Theory and applications*, Amsterdam: Gordon and Breach, 2001.

[37] M. Gorkunov, and M. Lapine, "Tuning of a nonlinear metamaterial band gap by an external magnetic field," *Physical Review B,* vol. 70, no. 23, pp. 235109, 2004.

[38] I. V. Shadrivov, A. B. Kozyrev, D. W. Van der Weide *et al.*, "Tunable transmission and harmonic generation in nonlinear metamaterials," *Applied Physics Letters,* vol. 93, no. 16, pp. 161903, 2008.

[39] C. A. Balanis, *Antenna Theory: Analysis and Design*: John Wiley & Sons, 2012.

[40] K. L. Wong, *Compact and Broadband Microstrip Antennas*: Wiley, 2002.

[41] G. Kumar, and K. P. Ray, *Broadband Microstrip Antennas*: Artech House, 2003.

[42] R. Garg, P. Bhartia, I. Bahl *et al.*, *Microstrip Antenna Design Handbook*: Artech House, 2001.

[43] A. Sanada, C. Caloz, and T. Itoh, "NOVEL ZEROTH-ORDER RESONANCE IN COMPOSITE RIGHT/LEFT-HANDED TRANSMISSION LINE RESONATORS," in In Proc. Asia-Pacific Microwave Conference, 2003, pp. 1588-1591.

[44] A. Sanada, M. Kimura, I. Awai *et al.*, "A Planar Zeroth-Order Resonator Antenna Using a Left-Handed Transmission Line," in In Microwave Conference, 2004. 34th European, IEEE, Amsterdam, 2004, pp. 1341-1344.

[45] A. Lai, T. Itoh, and C. Caloz, "Composite right/left-handed transmission line metamaterials," *IEEE Microwave Magazine,* vol. 5, no. 3, pp. 34-50, 2004.

[46] S. Yan, and G. A. E. Vandenbosch, "Zeroth-order resonant circular patch antenna based on periodic structures," *IET Microwaves, Antennas & Propagation,* vol. 8, no. 15, pp. 1432-1439, Dec. 2014.

[47] S. Liao, Q. Xue, and J. Xu, "Parallel-Plate Transmission Line and L-Plate Feeding Differentially Driven H-Slot Patch Antenna," *IEEE Antennas and Wireless Propagation Letters,* vol. 11, pp. 640-644, 2012.

[48] A. A. Deshmukh, and K. P. Pay, "Multi-Band Configurations of Stub-Loaded Slotted Rectangular Microstrip Antennas," *IEEE Antennas and Propagation Magazine,* vol. 52, no. 1, pp. 89-103, Feb. 2010.

[49] K. F. Lee, S. L. S. Yang, A. A. Kishk *et al.*, "The Versatile U-Slot Patch Antenna," *IEEE Antennas and Propagation Magazine,* vol. 52, no. 1, pp. 71-88, Feb. 2010.

[50] K. F. Lee, K. M. Luk, K. M. Mak *et al.*, "On the Use of U-Slots in the Design of Dual-and Triple-Band Patch Antennas," *IEEE Antennas and Propagation Magazine,* vol. 53, no. 3, pp. 60-74, June 2011.

[51] A. A. Deshmukh, and K. P. Ray, "Formulation of Resonance Frequencies for Dual-Band Slotted Rectangular Microstrip Antennas," *IEEE Antennas and Propagation Magazine,* vol. 54, no. 4, pp. 78-97, Aug. 2012.

[52] F. J. Herraiz-Martinez, V. Gonzalez-Posadas, L. E. Garcia-Munoz *et al.*, "Multifrequency and Dual-Mode Patch Antennas Partially Filled With Left-Handed

Structures," *IEEE Transactions on Antennas and Propagation,* vol. 56, no. 8, pp. 2527-2539, 2008.

[53] Y. Dong, H. Toyao, and T. Itoh, "Design and Characterization of Miniaturized Patch Antennas Loaded With Complementary Split-Ring Resonators," *IEEE Transactions on Antennas and Propagation,* vol. 60, no. 2, pp. 772-785, Feb. 2012.

[54] S. Yan, P. J. Soh, and G. A. E. Vandenbosch, "Wearable dual-band composite right/left-handed waveguide textile antenna for WLAN applications," *Electronics Letters,* vol. 50, no. 6, pp. 424-426, Match 2014.

[55] C. Wang, B.-J. Hu, and X.-Y. Zhang, "Compact Triband Patch Antenna With Large Scale of Frequency Ratio Using CRLH-TL Structures," *IEEE Antennas and Wireless Propagation Letters,* vol. 9, pp. 744-747, 2010.

[56] L. Akhoondzadeh-Asl, D. J. Kern, P. S. Hall *et al.*, "Wideband Dipoles on Electromagnetic Bandgap Ground Planes," *IEEE Transactions on Antennas and Propagation,* vol. 55, no. 9, pp. 2426-2434, 2007.

[57] S. R. Best, and D. L. Hanna, "Design of a Broadband Dipole in Close Proximity to an EBG Ground Plane," *IEEE Antennas and Propagation Magazine,* vol. 50, no. 6, pp. 52-64, 2008.

[58] O. Folayan, and R. Langley, "Dual frequency band antenna combined with a high impedance band gap surface," *IET Microwaves, Antennas & Propagation,* vol. 3, no. 7, pp. 1118-1126, 2009.

[59] R. C. Hadarig, M. E. de Cos Gomez, Y. Alvarez *et al.*, "Novel Bow-tie–AMC Combination for 5.8-GHz RFID Tags Usable With Metallic Objects," *IEEE Antennas and Wireless Propagation Letters,* vol. 9, pp. 1217-1220, 2011.

[60] N. A. Abbasi, and R. J. Langley, "Multiband-integrated antenna/artificial magnetic conductor," *IET Microwaves, Antennas & Propagation,* vol. 5, no. 6, pp. 711-717, 2011.

[61] D. Kim, and J. Yeo, "Dual-Band Long-Range Passive RFID Tag Antenna Using an AMC Ground Plane," *IEEE Transactions on Antennas and Propagation,* vol. 60, no. 6, pp. 2620-2626, June 2012.

[62] D. Cure, T. M. Weller, and F. A. Miranda, "Study of a Low-Profile le 2.4-GHz Planar Dipole Antenna Using a High-Impedance Surface With 1-D Varactor Tuning," *IEEE Transactions on Antennas and Propagation,* vol. 61, no. 2, pp. 506-515, 2013.

[63] H. Boutayeb, and T. A. Denidni, "Gain Enhancement of a CPW-Fed Monopole Antenna Using Polarization-Insensitive AMC Structure," *IEEE Transactions on Antennas and Propagation,* vol. 55, no. 11, pp. 3140-3145, 2007.

[64] J. Joubert, J. C. Vardaxoglou, W. G. Whittow *et al.*, "CPW-Fed Cavity-Backed Slot Radiator Loaded With an AMC Reflector," *IEEE Transactions on Antennas and Propagation,* vol. 60, no. 2, pp. 735-742, 2012.

[65] S. Yan, P. J. Soh, and G. A. E. Vandenbosch, "Low-profile dual-band textile antenna with artificial magnetic conductor plane," *IEEE Transactions on Antennas and Propagation,* vol. 62, no. 12, pp. 6487-6490, 2014.

[66] S. Yan, P. J. Soh, M. Mercuri *et al.*, "Low profile dual-band antenna loaded with artificial magnetic conductor for indoor radar systems," *IET Radar, Sonar & Navigation,* vol. 9, no. 2, pp. 184-190, Feb. 2015.

[67] Q. Wu, P. Pan, F. Y. Meng *et al.*, "A novel flat lens horn antenna designed based on zero refraction principle of metamaterials," *Applied Physics A,* vol. 87, no. 2, pp. 151-156, 2007.

[68] A. Grbic, R. Merlin, E. M. Thomas *et al.*, "Near-Field Plates Metamaterial Surfaces Arrays for Subwavelength Focusing and Probing," *Proceedings of IEEE,* vol. 99, no. 10, pp. 1806-1815, Oct. 2011.

[69] S. E. Hosseininnejad, N. Komjani, D. Zarifi *et al.*, "Directivity enhancement of circularly polarized microstrip antennas by chiral metamaterial covers," *IEICE Electronics Express,* vol. 9, no. 2, pp. 117-121, 2012.

[70] H. L. Zhu, S. W. Cheung, K. L. Chung *et al.*, "Linear-to-Circular Polarization Conversion Using Metasurface," *IEEE Transactions on Antennas and Propagation,* vol. 61, no. 9, pp. 4615-4623, Sep. 2013.

[71] H. L. Zhu, S. W. Cheung, X. H. Liu *et al.*, "Design of Polarization Reconfigurable Antenna Using Metasurface," *IEEE Transactions on Antennas and Propagation,* vol. 62, no. 6, pp. 2891-2898, June 2014.

[72] C. Caloz, and T. Itoh, "Array factor approach of leaky-wave antennas and application to 1-D 2-D composite right left-handed (CRLH) structures," *IEEE Microwave and Wireless Components Letters,* vol. 14, no. 6, pp. 274-276, June 2004.

[73] C. Caloz, T. Itoh, and A. Rennings, "CRLH Metamaterial Leaky-Wave and Resonant Antennas," *IEEE Antennas and Propagation Magazine,* vol. 50, no. 5, pp. 25-39, 2008.

[74] H. V. Nguyen, S. Abielmona, A. Rennings *et al.*, "Pencil-Beam Full-Space Scanning 2D CRLH Leaky-Wave Antenna Array," in IEEE Signals, Systems and Electronics, 2007. ISSSE'07. International Symposium on, 2007, pp. 139-142.

[75] O. Losito, M. Gallo, V. Dimiccoli *et al.*, "A tapered design of a CRLH-TL Leaky wave antenna," in Proceedings of the 5th European Conference on, IEEE, April, 2011, pp. 357-360.

[76] P. M. T. Ikonen, S. I. Maslovski, C. R. Simovski *et al.*, "On artificial magnetodielectric loading for improving the impedance bandwidth properties of microstrip antennas," *IEEE Transactions on Antennas and Propagation,* vol. 54, no. 6, pp. 1654-1662, June 2006.

[77] H. Mosallaei, and K. Sarabandi, "Design and Modeling of Patch Antenna Printed on Magneto-Dielectric Embedded-Circuit Metasubstrate," *IEEE Transactions on Antennas and Propagation,* vol. 55, no. 1, pp. 45-52, Jan. 2007.

[78] Y. Zhang, W. Hong, C. Yu *et al.*, "Planar Ultrawideband Antennas With Multiple Notched Bands Based on Etched Slots on the Patch andor Split Ring Resonators on the Feed Line," *IEEE Transactions on Antennas and Propagation,* vol. 56, no. 9, pp. 3063-3068, Sep. 2008.

[79] J. Y. Kim, B. C. Oh, N. Kim *et al.*, "Triple band-notched UWB antenna based on complementary meander line SRR," *Electronics Letters,* vol. 48, no. 15, pp. 896-897, July 2012.

[80] K. Buell, H. Mosallaei, and K. S. Sarabandi, "Metamaterial Insulator Enabled Superdirective Array," *IEEE Transactions on Antennas and Propagation,* vol. 55, no. 4, pp. 1074-1085, April 2007.

[81] A. Habashi, J. Nourinia, and C. Ghobadi, "Mutual Coupling Reduction Between Very Closely Spaced Patch Antennas Using Low-Pro fi le Folded Split-Ring

Resonators (FSRRs)," *IEEE Antennas and Wireless Propagation Letters,* vol. 10, pp. 862-865, 2011.

[82] M. A. Antoniades, and G. V. Eleftheriades, "A Broadband Series Power Divider Using Zero-Degree Metamaterial Phase-Shifting Lines," *IEEE Microwave and Wireless Components Letters,* vol. 15, no. 11, pp. 808-810, Nov. 2005.

[83] Y. Wu, Y. Liu, and S. Li, "Unequal dual-frequency Wilkinson power divider including series resistor–inductor–capacitor isolation structure," *IET Microwaves, Antennas & Propagation,* vol. 3, no. 7, pp. 1079-1085, 2009.

[84] M. A. Antoniades, and G. V. Eleftheriades, "compact linear lead lag metamaterial phase shifters for broadband applications," *IEEE Antennas and Wireless Propagation Letters,* vol. 2, pp. 103-106, 2003.

[85] C. Enkrich, M. Wegener, S. Linden *et al.*, "Magnetic metamaterials at telecommunication and visible frequencies," *physical Review Letters,* vol. 95, pp. 203901, 2005.

[86] J. Huangfu, L. Ran, H. Chen *et al.*, "Experimental confirmation of negative refractive index of a metamaterial composed of Ω-like metallic patterns," *Applied Physics Letters,* vol. 84, pp. 15537-1539, 2004.

[87] H. Chen, L. Ran, J. Huangfu *et al.*, "Magnetic properties of S-shaped split-ring resonators," *progress In Electromagnetics Research,* vol. 51, pp. 231-247, 2005.

[88] S. Linden, C. Enkrich, M. Wegener *et al.*, "Magnetic Response of Metamaterials at 100 Terahertz," *Science,* vol. 306, pp. 1351-1353, 2004.

[89] F. Bilotti, A. Tossano, and L. Vegni, "Design of Spiral and Multiple Split-Ring Resonators for the Realization of Miniaturized Metamaterial Samples," *IEEE Transactions on Antennas and Propagation,* vol. 55, pp. 2267, 2007.

[90] R. Gans, and H. Happel, "Zur Optik kolloidaler MetallÄosungen," *Ann. Physik, 4th Folge, Bd.,* vol. 29, pp. 277-300, 1909.

[91] C. L. Holloway, E. F. Kuester, J. Baker-Jarvis *et al.*, "A Double Negative (DNG) Composite Medium Composed of Magnetodielectric Spherical Particles Embedded in a Matrix," *IEEE Transactions on Antennas and Propagation,* vol. 51, pp. 2603, 2003.

[92] L. Lewin, "THE ELECTRICAL CONSTANTS OF A MATERIAL LOADED WITH SPHERICAL PARTICLES," *Electrical Engineers --- Part III: Radio and Commnication Engineering,* vol. 94, pp. 65-68, 1947.

[93] O. G. Vendik, and M. S. Gashinova, "Artificial Double Negative (DNG) Media Composed by Two Different Dielectric Sphere Lattices Embedded in a Dielectric Matrix," in 34th European Microwave Conference 2004, 2004, pp. 1209-1212.

[94] L. Jylhä, I. Kolmakov, S. Maslovski *et al.*, "Modeling of isotropic backward-wave materials composed of resonant spheres," *Journal of Applied Physics,* vol. 99, no. 4, pp. 043102, 2006.

[95] A. Sihvola, "Electromagnetic Mixing Formulas and Applications," in IEE Electromagnetic Waves Series 47, , Stevenage, Herts, UK, 1999.

[96] L. I. Basilio, L. K. Warne, W. L. Langston *et al.*, "Microwave-Frequency, Negative-Index Metamaterial Designs Based on Degenerate Dielectric Resonators," *IEEE Antennas and Wireless Propagation Letters,* vol. 11, pp. 113-116, 2012.

[97] E. F. Kuester, N. Memic, S. Shen *et al.*, "A NEGATIVE REFRACTIVE INDEX METAMATERIAL BASED ON A CUBIC ARRAY OF LAYERED NONMAG-

NETIC SPHERICAL PARTICLES," *Progress In Electromagnetics Research B,* vol. 33, pp. 175-202, 2011.

[98] L. Peng, L. Ran, H. Chen *et al.*, "Experimental Observation of Left-Handed Behavior in an Array of Standard Dielectric Resonators," *Physical Review Letters,* vol. 98, no. 15, pp. 157403, 2007.

[99] Q. Zhao, L. Kang, B. Du *et al.*, "Experimental Demonstration of Isotropic Negative Permeability in a Three-Dimensional Dielectric Composite," *Physical Review Letters,* vol. 101, no. 2, pp. 027402, 2008.

[100] X. Cai, R. Zhu, and G. Hu, "Experimental study for metamaterials based on dielectric resonators and wire frame," *Metamaterials,* vol. 2, no. 4, pp. 220-226, 2008.

[101] T. Lepetit, E. Akmansoy, and J. P. Ganne, "Experimental measurement of negative index in an all-dielectric metamaterial," *Applied Physics Letters,* vol. 95, no. 12, pp. 121101, 2009.

[102] L. Liu, J. Sun, X. Fu *et al.*, "ARTIFICIAL MAGNETIC PROPERTIES OF DIELECTRIC METAMATERIALS IN TERMS OF EFFECTIVE CIRCUIT MODEL," *Progress In Electromagnetics Research,* vol. 16, pp. 159-170, 2011.

[103] V. Yannopapas, and A. Moroz, "Negative refractive index metamaterials from inherently non-magnetic materials for deep infrared to terahertz frequency ranges," *Journal of Physics: Condensed Matter,* vol. 17, pp. 3717, 2005.

[104] A. Garcia-Etxarri, R. Gomez-Medina, L. S. Froufe-Perez *et al.*, "Strong magnetic response of submicron Silicon particles in the infrared," *Optics Express,* vol. 19, pp. 4815, 2011.

[105] A. Ahmadi, and H. Mosallaei, "All-Dielectric Metamaterials: Double Negative Behavior and Bandwidth-Loss Improvement," in Antennas and Propagation Society International Symposium, 2007, pp. 5527-5530.

[106] I. B. Vendik, M. A. Odit, and D. S. Kozlov, "3D isotropic metamaterial based on a regular array of resonant dielectric spherical inclusions," *Metamaterials,* vol. 3, no. 3-4, pp. 140-147, 2009.

[107] C. F. Bohren, and D. R. Huffman, *Absorption and Scattering of Light by Small Particles*: Wiley, University of California, Berkeley, 1983.

[108] C. Tserkezis, C. Gantzounis, and N. Stefanou, "Collective Plasmonic modes in ordered assemblies of metallic nanoshells," *Journal of Physics: Condensed Matter,* vol. 20, pp. 075232, 2008.

[109] J. Li, G. Sun, and C. T. Chan, "Optical properties of photonic crystals composed of metal-coated spheres," *physical Review B,* vol. 73, pp. 075117, 2006.

[110] J. B. Pendry, A. J. Holden, W. J. Stewart *et al.*, "Extremely Low Frequency Plasmons in Metallic Mesostructures," *physical Review Letters,* vol. 76, pp. 4773-4776, 1996.

[111] J. B. Pendry, A. J. Holden, D. J. Robbins *et al.*, "Low frequency plasmons in thin-wire structures," *J. Phys.: Condens. Matter,* vol. 10, pp. 4785, 1998.

[112] D. R. Smith, and S. Schultz, "Determination of effective permittivity and permeability of metamaterials from reflection and transmission coefficients," *Physical Review B,* vol. 65, no. 19, pp. 195104, 2002.

[113] S. Kim, E. F. Kuester, C. L. Holloway *et al.*, "Boundary Effects on the Determination of Metamaterial Parameters From Normal Incidence Reflection and

Transmission Measurements," *IEEE Transactions on Antennas and Propagation,* vol. 59, pp. 2226, 2011.

[114] X. Chen, T. Grzegorczyk, B.-I. Wu *et al.*, "Robust method to retrieve the constitutive effective parameters of metamaterials," *Physical Review E,* vol. 70, no. 1, pp. 016608, 2004.

[115] S. Kim, E. F. Kuester, C. L. Holloway *et al.*, "Effective Material Property Extraction of a Metamaterial by Taking Boundary Effects into Account at TE/TM Polarized Incidence," *Progress In Electromagnetics Research B,* vol. 36, pp. 1-33, 2012.

[116] D. R. Smith, D. C. Vier, T. Koschny *et al.*, "Electromagnetic parameter retrieval from inhomogeneous metamaterials," *Physical Review E,* vol. 71, no. 3, pp. 036617, 2005.

[117] A. Vasylchenko, Y. Schols, W. De Raedt *et al.*, "Quality assessment of computational techniques and software tools for planar antenna analysis," *IEEE Antennas and Propagation Magazine,* vol. 51, pp. 23-38, 2009.

[118] X.-J. He, Y. Wang, J.-S. Mei *et al.*, "Three-dimensional surface current loops in broadband responsive negative refractive metamaterial with isotropy," *Chinese Physics B,* vol. 21, no. 4, pp. 044101, 2012.

[119] D. L. Jaggard, A. R. Mickelson, and C. H. Papas, "On electromagnetic waves in chiral media," *Applied Physics A,* vol. 18, no. 2, pp. 211-216, 1979.

[120] B. Wang, J. Zhou, T. Koschny *et al.*, "Nonplanar chiral metamaterials with negative index," *Applied Physics Letters,* vol. 94, no. 15, pp. 151112, 2009.

[121] S. Zhang, Y.-S. Park, J. Li *et al.*, "Negative Refractive Index in Chiral Metamaterials," *Physical Review Letters,* vol. 102, no. 2, pp. 023901, 2009.

[122] A. V. Rogacheva, V. A. Fedotov, A. S. Schwanecke *et al.*, "Giant Gyrotropy due to Electromagnetic-Field Coupling in a Bilayered Chiral Structure," *Physical Review Letters,* vol. 97, no. 17, pp. 177401, 2006.

[123] E. Plum, V. A. Fedotov, A. S. Schwanecke *et al.*, "Giant optical gyrotropy due to electromagnetic coupling," *Applied Physics Letters,* vol. 90, no. 22, pp. 223113, 2007.

[124] H. Liu, D. Genov, D. Wu *et al.*, "Magnetic plasmon hybridization and optical activity at optical frequencies in metallic nanostructures," *Physical Review B,* vol. 76, no. 7, 2007.

[125] C. Huang, Y. Feng, J. Zhao *et al.*, "Asymmetric chiral metamaterial circular polarizer based on four U-shaped split ring resonators," *physical Review B,* vol. 85, no. 19, pp. 195131, 2012.

[126] M. Decker, M. Ruther, C. E. Kriegler *et al.*, "Strong optical activity from twisted-cross photonic metamaterials," *Optics Letters,* vol. 34, no. 16, pp. 2501-2503, 2009.

[127] M. Decker, R. Zhao, C. M. Soukoulis *et al.*, "Twisted split-ring-resonator photonic metamaterial with huge optical activity," *Optics Letters,* vol. 35, no. 10, pp. 1593-1595, 2010.

[128] E. Plum, X. X. Liu, V. Fedotov *et al.*, "Metamaterials: Optical Activity without Chirality," *Physical Review Letters,* vol. 102, no. 11, pp. 113902, 2009.

[129] E. Plum, V. A. Fedotov, and N. I. Zheludev, "Optical activity in extrinsically chiral metamaterial," *Applied Physics Letters,* vol. 93, no. 19, pp. 191911, 2008.

[130] J. Zhou, D. R. Chowdhury, R. Zhao *et al.*, "Terahertz chiral metamaterials with giant and dynamically tunable optical activity," *Physical Review B,* vol. 86, no. 3, pp. 035448, 2012.

[131] S. Zhang, J. Zhou, Y.-S. Park *et al.*, "Photoinduced handedness switching in terahertz chiral metamolecules," *Nature Communications,* vol. 3, pp. 942, 2012.

[132] M. Mutlu, A. E. Akosman, A. E. Serebryannikov *et al.*, "Asymmetric chiral metamaterial circular polarizer based on four U-shaped split ring resonators," *Optics Letters,* vol. 36, no. 9, pp. 1653-1655, 2011.

[133] S. Yan, and G. A. E. Vandenbosch, "Increasing the NRI bandwidth of dielectric sphere-based metamaterials by coating," *progress In Electromagnetics Research,* vol. 132, pp. 1-22, 2012.

[134] E. Plum, J. Zhou, J. Dong *et al.*, "Metamaterial with negative index due to chirality," *Physical Review B,* vol. 79, no. 3, pp. 035407, 2009.

[135] J. Zhou, J. Dong, B. Wang *et al.*, "Negative refractive index due to chirality," *Physical Review B,* vol. 79, no. 12, pp. 121104, 2009.

[136] X. Xiong, W.-H. Sun, Y.-J. Bao *et al.*, "Construction of a chiral metamaterial with a U-shaped resonator assembly," *Physical Review B,* vol. 81, no. 7, pp. 075119, 2010.

[137] R. Zhao, L. Zhang, J. Zhou *et al.*, "Conjugated gammadion chiral metamaterial with uniaxial optical activity and negative refractive index," *Physical Review B,* vol. 83, no. 3, pp. 035105, 2011.

[138] V. Volskia, G. A. E. Vandenboscha, and A. Vasylchenkoa, "A dedicated technique to measure shielding effectiveness of textiles using a two-horn antenna set-up," *Journal of the Textile Institute,* vol. 102, no. 2, pp. 164-171, 2011.

[139] J. D. Jackson, *Classical Electrodynamics, 3rd*, New York: Wiley, 1998.

[140] H. Liu, J. X. Cao, S. N. Zhu *et al.*, "Lagrange model for the chiral optical properties of stereometamaterials," *Physical Review B,* vol. 81, no. 24, pp. 241403, 2010.

[141] N. Liu, H. Liu, S. Zhu *et al.*, "Stereometamaterials," *Nature Photonics,* vol. 3, pp. 157-162, 2009.

[142] Z. Li, R. Zhao, T. Koschny *et al.*, "Chiral metamaterials with negative refractive index based on four "U" split ring resonators," *Applied Physics Letters,* vol. 97, no. 8, pp. 081901, 2010.

[143] M. Boutria, R. Oussaid, D. Van Labeke *et al.*, "Tunable artificial chirality with extraordinary transmission metamaterials," *Physical Review B,* vol. 86, no. 15, pp. 155428, 2012.

[144] N. V. T. Dinh, "Metamaterial based GPS Antennas," Department of Electrical Engineering, KU Leuven, Leuven, Belgium, July 2014.

[145] D. R. Smith, W. J. Padilla, D. C. Vier *et al.*, "Composite Medium with Simultaneously Negative Permeability and Permittivity," *physical Review Letters,* vol. 84, no. 18, pp. 4184-4187, 2000.

[146] I. Sersic, M. Frimmer, E. Verhagen *et al.*, "Electric and Magnetic Dipole Coupling in Near-Infrared Split-Ring Metamaterial Arrays," *Physical Review Letters,* vol. 103, no. 21, pp. 213902, 2009.

[147] J. Baena, R. Marqués, F. Medina *et al.*, "Artificial magnetic metamaterial design by using spiral resonators," *Physical Review B,* vol. 69, no. 1, pp. 014402, 2004.

[148] S. Yan, and G. A. E. Vandenbosch, "Chiral structure based on bilayered displaced U pair," *Europhysics Letters (EPL),* vol. 103, no. 1, pp. 18002, 2013.

[149] M. Mutlu, A. E. Akosman, A. E. Serebryannikov *et al.*, "Diodelike Asymmetric Transmission of Linearly Polarized Waves Using Magnetoelectric Coupling and Electromagnetic Wave Tunneling," *Physical Review Letters,* vol. 108, no. 21, pp. 213905, 2012.

[150] V. Fedotov, P. Mladyonov, S. Prosvirnin *et al.*, "Asymmetric Propagation of Electromagnetic Waves through a Planar Chiral Structure," *Physical Review Letters,* vol. 97, no. 16, pp. 167401, 2006.

[151] S. Zhang, D. A. Genov, Y. Wang *et al.*, "Plasmon-Induced Transparency in Metamaterials," *Physical Review Letters,* vol. 101, no. 4, pp. 147401, 2008.

[152] N. Liu, H. Guo, L. Fu *et al.*, "Plasmon Hybridization in Stacked Cut-Wire Metamaterials," *Advanced Materials,* vol. 19, no. 21, pp. 3628-3632, 2007.

[153] N. Liu, S. Kaiser, and H. Giessen, "Magnetoinductive and Electroinductive Coupling in Plasmonic Metamaterial Molecules," *Advanced Materials,* vol. 20, no. 23, pp. 4521-4525, 2008.

[154] Y. Sun, H. Jiang, Y. Yang *et al.*, "Electromagnetically induced transparency in metamaterials: Influence of intrinsic loss and dynamic evolution," *Physical Review B,* vol. 83, no. 19, pp. 195140, 2011.

[155] C. Wu, A. B. Khanikaev, R. Adato *et al.*, "Fano-resonant asymmetric metamaterials for ultrasensitive spectroscopy and identification of molecular monolayers," *Nature Materials,* vol. 11, no. 1, pp. 69-75, 2012.

[156] N. Liu, T. Weiss, M. Mesch *et al.*, "Planar Metamaterial Analogue of Electromagnetically Induced Transparency for Plasmonic Sensing," *Nano Letters,* vol. 10, no. 4, pp. 1103-1107, 2010.

[157] F. Y. Meng, Q. Wu, D. Erni *et al.*, "Polarization-Independent Metamaterial Analog of Electromagnetically Induced Transparency for a Refractive-Index-Based Sensor," *iEEE Transactions on Microwave Theory and Techniques,* vol. 60, no. 10, pp. 3013-3022, 2012.

[158] S. Zhu, and R. Langley, "Dual-band wearable textile antenna on an EBG substrate," *IEEE Transactions on Antennas and Propagation,* vol. 57, no. 4, pp. 926-935, 2009.

[159] Z. H. Jiang, D. E. Brocker, P. E. Siever *et al.*, "A Compact, Low-Profile Metasurface-Enabled Antenna for Wearable Medical Body-Area Network Devices," *IEEE Transactions on Antennas and Propagation,* vol. 62, no. 8, pp. 4021-4030, 2014.

[160] I. Locher, M. Klemm, T. Kirstein *et al.*, "Design and characterization of purely textile patch antennas," *IEEE Transactions on Advanced Packaging,* vol. 29, no. 4, pp. 777-788, 2006.

[161] P. J. Soh, B. Van den Bergh, H. Xu *et al.*, "A smart wearable textile array system for biomedical telemetry applications," *IEEE Transactions on Microwave Theory and Techniques,* vol. 61, no. 5, pp. 2253-2261, 2013.

[162] A. Tronquo, H. Rogier, C. Hertleer *et al.*, "Robust planar textile antenna for wireless body LANs operating in 2.45 GHz ISM band," *Electronics Letters,* vol. 42, no. 3, pp. 142-143, 2006.

[163] S. Agneessens, and H. Rogier, "Compact Half Diamond Dual-Band Textile HMSIW On-Body Antenna," *IEEE Transactions on Antennas and Propagation,* vol. 62, no. 5, pp. 2374-2381, 2014.

[164] S. Lemey, F. Declercq, and H. Rogier, "Dual-band substrate integrated waveguide textile antenna with integrated solar harvester," *IEEE Antennas and Wireless Propagation Letters,* vol. 13, pp. 269-272, 2014.

[165] T. Kaufmann, and C. Fumeaux, "Wearable textile half-mode substrate-integrated cavity antenna using embroidered vias," *IEEE Antennas and Wireless Propagation Letters,* vol. 12, pp. 805-808, 2013.

[166] M. Schussler, J. Freese, and R. Jakoby, "Design of Compact Planar Antennas using LH-Transmission Lines," in In Microwave Symposium Digest, 2004 IEEE MTT-S International, 2004, pp. 209-212.

[167] C.-J. Lee, K. M. K. H. Leong, and T. Itoh, "Composite Right Left-Handed Transmission Line Based Compact Resonant Antennas for RF Module Integration," *IEEE Transactions on Antennas and Propagation,* vol. 54, no. 8, pp. 2283-2291, 2006.

[168] A. Lai, K. M. K. H. Leong, and T. Itoh, "Infinite Wavelength Resonant Antennas With Monopolar Radiation Pattern Based on Periodic Structures," *IEEE Transactions on Antennas and Propagation,* vol. 55, no. 3, pp. 868-876, 2007.

[169] F. J. Herraiz-Martinez, V. Gonzalez-Posadas, F. Inigo-Villacorta *et al.*, "Low-cost Approach based on an Eigenfrequency Method to obtain the Dispersion Diagram in CRLH Structures," *IEEE Microwave and Wireless Components Letters,* vol. 17, pp. 13-15, 2007.

[170] Y. Dong, H. Toyao, and T. Itoh, "Compact Circularly-Polarized Patch Antenna Loaded With Metamaterial Structures," *IEEE Transactions on Antennas and Propagation,* vol. 59, no. 11, pp. 4329-4333, 2011.

[171] O. Quevedo-Teruel, and E. Rajo-Iglesias, "Inverted mode patch antenna for dual-band communications," *IEEE Antennas and Wireless Propagation Letters,* vol. 7, pp. 792-794, 2008.

[172] C. Caloz, and T. Itoh, *Electromagnetic metamaterials: transmission line theory and microwave applications*: John Wiley & Sons, 2005.

[173] Y. Dong, and T. Itoh, "Promising Future of Metamaterials," *IEEE Microwave Magazine,* vol. 13, no. 2, pp. 39-56, 2012.

[174] Viscose, Wool Felt Sheet, 3 mm, RS Components Inc. Available http://uk.rs-online.com/web/p/felt-sheets/7336775/.

[175] SHIELDIT TM Super, Less EMF Inc. Available http://www.lessemf.com/1220.pdf.

[176] RS Straight Panel Mount SMA Connector, jack, Solder Termination, RS Components Inc. Available http://uk.rs-online.com/web/p/sma-connectors/5463181/.

[177] Computer Simulation Technology Microwave Studio (CST MWS), 2013. Available https://www.cst.com/Products/CSTMWS.

[178] J. Gemio, J. Parron, and J. Soler, "Human body effects on implantable antennas for ISM bands applications: Models comparison and propagation losses study," *progress In Electromagnetics Research,* vol. 110, pp. 437-452, 2010.

[179] S. Yan, P. J. Soh, and G. A. E. Vandenbosch, "Compact All-Textile Dual-band Antenna Loaded with Metamaterial Inspired Structure," *IEEE Antennas and Wireless Propagation Letters*, 2014.

[180] Viscose, Wool Felt Sheet, 6 mm, RS Components Inc. Available http://uk.rs-online.com/web/p/felt-sheets/7336779/.

[181] CONDUCTIVE THREAD, Less EMF Inc. Available http://www.lessemf.com/fabric.html.

[182] Silver Conductive Epoxy, MG Chemicals Inc. Available http://www.mgchemicals.com/products/adhesives/electrically-conductive/silver-conductive-epoxy-8331/.

[183] A. Ahmadi, S. Saadat, and H. Mosallaei, "Resonance and Q Performance of Ellipsoidal ENG Subwavelength Radiators," *IEEE Transactions on Antennas and Propagation,* vol. 59, no. 3, pp. 706-713, 2011.

[184] A. Erentok, and R. W. Ziolkowski, "Metamaterial-Inspired Efficient Electrically Small Antennas," *IEEE Transactions on Antennas and Propagation,* vol. 56, no. 3, pp. 691-707, 2008.

[185] S. Yan, and G. A. E. Vandenbosch, "A Fully Planar Near-Field Resonant Parasitic Antenna," *Progress In Electromagnetics Research C,* vol. 54, pp. 163-169, 2014.

[186] P. J. Soh, G. A. E. Vandenbosch, F. H. Wee *et al.*, "Specific Absorption Rate (SAR) Evaluation of Textile Antennas," *IEEE Antennas and Propagation Magazine,* vol. accepted, to appear, 2015.

[187] HUGO Human Body Model, CST. Available https://www.cst.com/Applications/Article/HUGO-Human-Body-Model.

[188] V. González-Posadas, D. Segovia-Vargas, E. Rajo-Iglesias *et al.*, "Approximate analysis of short circuited ring patch antenna working at TM01 mode," *IEEE Transactions on Antennas and Propagation,* vol. 54, no. 6, pp. 1875-1879, 2006.

[189] Ó. Quevedo-Teruel, and E. Rajo-Iglesias, "Design of Short-Circuited Ring-Patch Antennas Working at TM_{01} Mode Based on Neural Networks," *IEEE Antennas and Wireless Propagation Letters,* vol. 5, pp. 559-562, 2006.

[190] A. K. Bhattacharyya, and R. Garg, "Generalised transmission line model for microstrip patches," *IEE Proceedings H (Microwaves, Antennas and Propagation), IET Digital Library,* vol. 132, no. 2, pp. 93-98, 1985.

[191] A. K. Bhattacharyya, and R. Garg, "Input impedance of annular ring microstrip antenna using circuit theory approach," *IEEE Transactions on Antennas and Propagation,* vol. 33, no. 4, pp. 369-374, 1985.

[192] A. Yu, F. Yang, and A. Z. Elsherbeni, "A DUAL BAND CIRCULARLY POLARIZED RING ANTENNA BASED ON COMPOSITE RIGHT AND LEFT HANDED METAMATERIALS," *progress In Electromagnetics Research,* vol. 78, pp. 73-81, 2008.

[193] I. J. Bahl, *Lumped elements for RF and microwave circuits*: Artech House, 2003.

[194] E. Rajo-Iglesias, O. Quevedo-Teruel, and M. Sanchez-Fernandez, "Compact multimode patch antennas for MIMO applications [wireless corner]," *IEEE Antennas and Propagation Magazine,* vol. 50, no. 2, pp. 197-205, 2008.

[195] S. Baek, and S. Lim, "Miniaturised zeroth-order antenna on spiral slotted ground plane," *Electronics Letters,* vol. 45, no. 20, pp. 1012, 2009.

[196] S.-M. Han, J.-W. Baik, and Y.-S. Kim, "A Slot-Loaded Composite Right Left-Handed Transmission Line for a Zeroth-Order Resonant Antenna With Improved Efficiency," *IEEE Transactions on Microwave Theory and Techniques,* vol. 57, no. 11, pp. 2775-2782, 2009.

[197] H. Tang, and X. Zhao, "Center-fed circular epsilon-negative zeroth-order resonator antenna," *Microwave and Optical Technology Letters,* vol. 51, no. 10, pp. 2423-2428, 2008.

[198] S. Yoo, and S. Kahng, “CRLH ZOR ANTENNA OF A CIRCULAR MICROSTRIP PATCH CAPACITIVELY COUPLED TO A CIRCULAR SHORTED RING,” *progress In Electromagnetics Research C,* vol. 25, pp. 15-26, 2012.

[199] D. M. Pozar, and B. Kaufman, “Comparison of three methods for the measurement of printed antenna efficiency,” *IEEE Transactions on Antennas and Propagation,* vol. 36, no. 1, pp. 136-139, 1988.

[200] A. Rennings, T. Liebig, S. Otto *et al.*, “Highly Directive Resonator Antennas based on Composite RightLeft-Handed (CRLH) Transmission Lines,” 2007, pp. 190-194.

[201] K. E. Browne, R. J. Burkholder, and J. L. Volakis, “Through-wall opportunistic sensing system utilizing a low-cost flat-panel array,” *IEEE Transactions on Antennas and Propagation,* vol. 59, no. 3, pp. 859-868, 2011.

[202] S. Kim, Y. J. Ren, H. Lee *et al.*, “Monopole Antenna With Inkjet-Printed EBG Array on Paper Substrate for Wearable Applications,” *IEEE Antennas and Wireless Propagation Letters,* vol. 11, pp. 663-666, 2012.

[203] M. S. Alam, N. Misran, and M. T. Islam, “Inverse triangular-shape CPW-fed antenna loaded with EBG reflector,” *Electronics Letters,* vol. 49, no. 2, pp. 86-88, 2013.

[204] Viscose, Wool Felt Sheet, 1.5 mm, RS Components Inc. Available http://uk.rs-online.com/web/p/felt-sheets/7336772/.

[205] J. Lilja, and P. Salonen, “On the modeling of conductive textile materials for SoftWearAntennas,” in In Antennas and Propagation Society International Symposium, APSURSI'09. IEEE, 2009, pp. 1-4.

[206] S. J. Boyes, P. J. Soh, Y. Huang *et al.*, “Measurement and performance of textile antenna efficiency on a human body in a reverberation chamber,” *IEEE Transactions on Antennas and Propagation,* vol. 61, no. 2, pp. 871-881, 2013.

[207] P. J. Soh, G. A. E. Vandenbosch, F. H. Wee *et al.*, “Specific Absorption Rate (SAR) evaluation of biomedical telemetry textile antennas,” in In Microwave Symposium Digest (IMS), 2013 IEEE MTT-S International, 2013, pp. 1-3.

[208] S. Yan, P. J. Soh, and G. A. E. Vandenbosch, “Dual-Band Textile MIMO Antenna Based on Substrate Integrated Waveguide (SIW) Technology,” *IEEE Transactions on Antennas and Propagation*, 2015.

[209] S. Yan, P. J. Soh, and G. A. E. Vandenbosch, “Wearable Dual-Band Magneto-Electric Dipole Antenna for WBAN/WLAN Applications,” *IEEE Transactions on Antennas and Propagation*, 2015.

[210] N. I. o. H. Nat. Inst. on Aging, US Dept. of Health and Human Services, Washington DC, 2007. "Why population aging matters: a global perspective". Available http://www.nia.nih.gov/sites/default/files/wpam.pdf.

[211] R. Saxby, “How silicon will transform healthcare,” in Third IET Int. Conf. on Medical Electrical Devices and Technology (MEDTECH 2007), January, 2007, pp. 135-150.

[212] M. Mercuri, P. J. Soh, G. Pandey *et al.*, “Analysis of an indoor biomedical radar-based system for health monitoring,” *IEEE Transactions on Microwave Theory and Techniques,* vol. 61, no. 5, pp. 2061-2068, 2013.

[213] P. J. Soh, M. Mercuri, G. Pandey *et al.*, “Dual-band Planar Bowtie Monopole for a Fall-Detection Radar and Telemetry System,” *IEEE Antennas and Wireless Propagation Letters,* vol. 11, pp. 1698-1701, 2012.

[214] P. Karsmakers, T. Croonenborghs, M. Mercuri *et al.*, "Automatic in-door fall detection based on microwave radar measurement," in Proc. Eur. Radar Conf., Amsterdam, The Netherlands, Oct.-Nov. 2012, pp. 202-205.

[215] M. Mercuri, P. J. Soh, D. M. M. Schreurs *et al.*, "A practical distance measurement improvement technique for a SFCW-based health-monitoring radar in real indoor environment " in Automatic RF Techniques Group Conf. 7, June 2013.

PUBLICATIONS

■ International papers

[1] **S. Yan**, and G.A.E. Vandenbosch. "Increasing the NRI bandwidth of dielectric sphere-based metamaterials by coating." *Progress In Electromagnetics Research* 132 (2012): 1-23.

[2] **S. Yan**, and G.A.E. Vandenbosch. "Chiral structure based on bilayered displaced U pair." *EPL (Europhysics Letters)* 103.1 (2013): 18002.

[3] **S. Yan**, and G.A.E. Vandenbosch. "Compact circular polarizer based on chiral twisted double split-ring resonator." *Applied Physics Letters* 102.10 (2013): 103503.

[4] **S. Yan**, P.J. Soh and G.A.E. Vandenbosch. "A wearable dual-band composite right/left-handed (CRLH) waveguide textile antenna for WLAN applications", *Electronics Letters,* 50. 6 (2014): 424-426.

[5] **S. Yan**, P.J. Soh and G.A.E. Vandenbosch. "Made to Worn", *Electronics Letters,* 50. 6 (2014): 420.

[6] **S. Yan**, and G.A.E. Vandenbosch. "Zeroth-order Resonant Circular Patch Antenna Based on Periodic Structures", *IET Microwaves, Antennas & Propagation,* 8. 15 (2014): 1432-1439.

[7] **S. Yan**, and G.A.E. Vandenbosch. "An encapsulating meta-molecule: U resonator containing spiral line", *Japanese Journal of Applied Physics* (*JJAP),* 53. 11 (2014) 110306.

[8] **S. Yan**, P.J. Soh, M. Mercuri, D.M.M.–P. Schreurs, and G.A.E. Vandenbosch. "A low profile dual-band antenna loaded with artificial magnetic conductor for indoor radar systems", *IET Radar, Sonar & Navigation,* 9. 2 (2015): 184 – 190.

[9] **S. Yan**, P.J. Soh, and G.A.E. Vandenbosch. "Low-profile dual-band textile antenna with artificial magnetic conductor plane", *IEEE Transactions on Antennas and Propagation,* 62. 12 (2014): 6487-6490.

[10] **S. Yan**, and G.A.E. Vandenbosch. "A Fully Planar Near-field Resonant Parasitic Antenna", *Progress In Electromagnetics Research* C (PIER C), 54 (2014): 163-169.

[11] **S. Yan**, P.J. Soh, and G.A.E. Vandenbosch. "Compact All-textile Dual-band Antenna Loaded with Metamaterial Inspired Structure", *IEEE Antennas and Wireless Propagation Letters,* 2015 DOI: 10.1109/LAWP.2014.2370254.

[12] Y. Svezhentsev, P.J. Soh, **S. Yan**, and G.A.E. Vandenbosch, "Green's Functions for Probe-fed Arbitrary-Shaped Cylindrical Microstrip Antennas", *IEEE Transactions on Antennas and Propagation*, 63.3 (2015): 993-1003.

■ Papers and abstracts at international conferences

[1] **S. Yan**, and G.A.E. Vandenbosch. "Circular polarizer Based on chiral twisted structure." *EMC Europe 2013 Symposium*, Brugge, Belgium, Sep. 2013.

[2] **S. Yan**, and G.A.E. Vandenbosch, "Circuit Model of Circular Antenna Loaded with Composite Right/Left-Handed Transmission Line", *European Conference on Antennas and Propagation*, The Hague, The Netherlands, Apr. 2014.

[3] X. Zheng, **S. Yan**, N. Verellen, V. Volskiy, P. Van Dorpe, G. A. E. Vandenbosh, and V. V. Moshchalkov, "An N-Port Network Model for Nanoantennas", *European Conference on Antennas and Propagation*, The Hague, The Netherlands, Apr. 2014.

[4] Y. Svezhentsev, V. Volskiy, P.J. Soh, **S. Yan**, and G.A.E. Vandenbosch, "Omnidirectional Conformal Antenna Array Based on E-Shaped Patches", *European Conference on Antennas and Propagation*, The Hague, The Netherlands, April 2014.

[5] Y. Svezhentsev, P.J. Soh, **S. Yan**, V. Volskiy, and G.A.E. Vandenbosch, "Omnidirectional Horizontally-Polarized Cylindrical Microstrip Antenna with Two Parasitic Patches", *IEEE International Symposium on Antennas and Propagation and USNC-URSI national Radio Science Meeting*, Mephis, Tennessee, USA, July 2014.

[6] N. Thi Hien, E. Janssens, P. Lievens, **S. Yan**, G.A.E. Vandenbosch and V.D. Lam, "Simulation and experimental evidence for broadband negative refractive index metamaterials based on hybridization effect", *7th International Workshop on Advanced Materials Science and Nanotechnology, IWAMSN 2014*, Ha Long City, Vietnam, Nov. 2014.

[7] **S. Yan**, P.J. Soh, and G.A.E. Vandenbosch. "Performance on the Human Body of a Dual-Band Textile Antenna loaded with Metamaterials", *European Conference on Antennas and Propagation*, Lisbon, Portugal, April 2015*,* accepted.

[8] Y. Svezhentsev, **S. Yan**, V. Volskiy, and G.A.E. Vandenbosch. "Omnidirectional Cylindrical Microstrip Antennas with Horizontally-Polarized Radiation", *European Microwave Week 2015*, Paris, France, Sep. 2015, accepted.

[9] P.J. Soh, **S. Yan** and G.A.E. Vandenbosch. "SAR MITIGATION OF TEXTILE ANTENNA VIA AN ARTIFICIAL MAGNETIC CONDUCTOR (AMC) PLANE", URSI *Atlantic Radio Science Conference 2015 (AT-RASC 2015)*, Gran Ganaria, Canary Islands, May 2015, accepted.

■ Manuscripts under review

[1] **S. Yan**, P.J. Soh, and G.A.E. Vandenbosch. "Wearable Dual-Band Magneto-Electric Dipole Antenna for WBAN/WLAN Applications", *IEEE Transactions on Antennas and Propagation*, minor revision.

[2] **S. Yan**, P.J. Soh, and G.A.E. Vandenbosch. "Dual-Band Textile MIMO Antenna Based on Substrate Integrated Waveguide (SIW) Technology", *IEEE Transactions on Antennas and Propagation*, major revision.

[3] **S. Yan**, and G.A.E. Vandenbosch. "Meta-loaded Circular Sector Patch Antenna ", *IET Microwave, Antennas & Propagation*, submitted 09 Jan. 2015.

[4] L. A. Yimdjo Poffelie, P.J. Soh, **S. Yan**, and G.A.E. Vandenbosch. "A High Fidelity All-Textile UWB Antenna with Low SAR for WBAN Applications", *IEEE Transactions on Antennas and Propagation*, major revision.

[5] Y. Svezhentsev, V. Volskiy, **S. Yan**, P.J. Soh, and G.A.E. Vandenbosch. "Omnidirectional Wide-Band E-Shaped Cylindrical Patch Antennas", *IEEE Transactions on Antennas and Propagation*, major revision.

[6] **S. Yan**, and G.A.E. Vandenbosch. "Radiation Pattern Reconfigurable Wearable Antenna Based on Metamaterial Structure", *IEEE Transactions on Antennas and Propagation*, submitted 26 April 2015.

[7] Y. Svezhentsev, V. Volskiy, **S. Yan**, and G.A.E. Vandenbosch. "Omnidirectional Wide-band E-shaped Cylindrical Patch Antenna with Horizontal Polarisation", *IET Electronics Letters*, submitted 6 May 2015.